

See discussions, stats, and author profiles for this publication at: <https://www.researchgate.net/publication/239598657>

Low Dielectric Constant Materials for Micro Electronics

ARTICLE *in* JOURNAL OF APPLIED PHYSICS · JUNE 2003

Impact Factor: 2.18 · DOI: 10.1063/1.1567460

CITATIONS

795

READS

41

6 AUTHORS, INCLUDING:



Mikhail R Baklanov

imec Belgium

353 PUBLICATIONS **4,367** CITATIONS

SEE PROFILE



Francesca Iacopi

Griffith University

107 PUBLICATIONS **1,920** CITATIONS

SEE PROFILE



S.H. Brongersma

Imec Netherlands

51 PUBLICATIONS **1,609** CITATIONS

SEE PROFILE

APPLIED PHYSICS REVIEWS—FOCUSED REVIEW

Low dielectric constant materials for microelectronics

K. Maex^{a)}

IMEC, Kapeldreef 75, 3001 Leuven and EE. Department, K.U.-Leuven, 3001 Leuven, Belgium

M. R. Baklanov

Affiliate researcher at IMEC from XPEQT, Kapeldreef 75, 3001 Leuven, Belgium

D. Shamiryan and F. Iacopi

IMEC, Kapeldreef 75, 3001 Leuven and EE. Department K.U.-Leuven, 3001 Leuven, Belgium

S. H. Brongersma

IMEC, Kapeldreef 75, 3001 Leuven, Belgium

Z. S. Yanovitskaya

Institute of Semiconductor Physics, 630090 Novosibirsk, Russia

(Received 9 September 2002; accepted 31 January 2003)

The ever increasing requirements for electrical performance of on-chip wiring has driven three major technological advances in recent years. First, copper has replaced Aluminum as the new interconnect metal of choice, forcing also the introduction of damascene processing. Second, alternatives for SiO₂ with a lower dielectric constant are being developed and introduced in main stream processing. The many new resulting materials needs to be classified in terms of their materials characteristics, evaluated in terms of their properties, and tested for process compatibility. Third, in an attempt to lower the dielectric constant even more, porosity is being introduced into these new materials. The study of processes such as plasma interactions and swelling in liquid media now becomes critical. Furthermore, pore sealing and the deposition of a thin continuous copper diffusion barrier on a porous dielectric are of prime importance. This review is an attempt to give an overview of the classification, the characteristics and properties of low-*k* dielectrics. In addition it addresses some of the needs for improved metrology for determining pore sizes, size distributions, structure, and mechanical properties. © 2003 American Institute of Physics.

[DOI: 10.1063/1.1567460]

TABLE OF CONTENTS

I. Introduction.....	8794	C. Chemical vapor deposition (CVD).....	8802
A. Low- <i>k</i> dielectrics for electrical performance....	8794	1. Constitutive porosity in silica by	
B. Implementation of low- <i>k</i> dielectrics.....	8795	deposition.....	8802
II. Dielectric materials.....	8796	2. Constitutive porosity in silica by doping...	8803
A. Capacitance and relative permittivity.....	8796	3. Subtractive porosity.....	8804
B. Polarization phenomena.....	8796	IV. Characterization techniques.....	8804
C. Film density and relative permittivity.....	8797	A. Composition.....	8805
D. Relative permittivity and frequency.....	8797	1. Fourier transform infrared spectroscopy	
III. Constitutive and subtractive porous dielectrics....	8798	(FTIR).....	8805
A. Classification of constitutive porous materials..	8799	2. Energy filtered transmission electron	
1. Silsesquioxane (SSQ) based.....	8799	spectroscopy (EFTEM).....	8806
2. Silica based.....	8799	3. Nuclear magnetic resonance (NMR).....	8806
3. Organic polymers.....	8800	B. Electrical characterization.....	8807
4. Amorphous carbon.....	8800	1. Area capacitance.....	8807
B. Deposition by spin on.....	8800	2. Interline capacitance.....	8807
1. Constitutive porous dielectrics.....	8800	C. Pore structure.....	8808
2. Subtractive porous dielectrics.....	8801	1. Positron annihilation lifetime spectroscopy	
		(PALS, PAS).....	8808
		2. Scattering techniques (SANS, SAXS).....	8809
		3. Adsorption techniques (BJH, EP).....	8810
		4. Comparative study.....	8813
		5. Limitations of the methods for evaluation	
		of thin film low- <i>k</i> dielectrics.....	8813

^{a)} Author to whom correspondence should be addressed; electronic mail: maex@imec.be

D. Mechanical characterization.	8814
1. Hardness and elastic modulus evaluation. ...	8814
2. Quantitative adhesion measurements.	8816
V. Properties of low- <i>k</i> materials.	8817
A. Physico-chemical properties.	8817
1. Composition and stability.	8817
2. Pore structure.	8820
3. Thermal conductivity.	8822
B. Electrical properties.	8822
C. Mechanical properties.	8823
1. Modulus and hardness of various low- <i>k</i> films.	8824
2. Adhesion.	8824
3. Thermal expansion.	8825
VI. Process interactions.	8825
A. Interaction of low- <i>k</i> dielectrics with plasmas. ...	8825
1. SSQ-based materials.	8825
2. Silica-based materials.	8826
3. Organic polymers.	8827
B. Swelling of low- <i>k</i> dielectric films in liquid media.	8828
C. Thin film deposition on porous dielectrics.	8830
D. Pore sealing.	8831
1. Characterization of sealing defects.	8831
2. Pore sealing by thin film deposition.	8832
3. Simulation of pore sealing by thin film deposition.	8833
4. Pore sealing by plasma surface interaction .	8835
5. Pore sealing by surface cross-linking/reconstruction.	8836
Appendix: Glossary (terms and abbreviations)	8836

I. INTRODUCTION

A. Low-*k* dielectrics for electrical performance

The microelectronics industry is continuously reinvesting its past success into the development of more advanced processes. This has led to Moore's law, which is forecasting transistor density, chip complexity, and operating speed or frequency for future technology nodes.

So far the emphasis in scaling feature sizes has been on the maximization of transistor density. All of this is driven by the need for electrical and functional performance. It is recognized, however, that device physics is not the first limiting factor to the continued performance improvement for systems. The challenge will be to carry electric power and to distribute the clock signals that control the timing and synchronize the operation. This challenge extends beyond the materials properties and technology and also involves system architecture.^{1,2}

The propagation velocity of electromagnetic waves will become increasingly important due to their unyielding constraints on interconnect delay. The introduction of Cu and low-*k* dielectrics has incrementally improved the situation as compared to the conventional Al/SiO₂ technology by reducing both resistivity of and capacitance between wires. Interconnect technology is the determining factor for signal delay. The impact of delay will undoubtedly increase as we move into the nanometer regime. Now that Cu has become the

common metallization material, lowering signal delay by introducing low-*k* dielectrics is one of the main challenges today.

Power consumption is a major concern for interconnects besides signal delay. Ever increasing frequencies and higher densities lead to a dramatic increase in power consumption. There are two elements contributing to the power consumption that are of interest to this paper. One is the dynamic power given by

$$P = \alpha C f V^2, \quad (1)$$

where P is the power consumption, α is the wire activity (i.e., when the wire is really transferring a signal), f is the frequency, V is the power supply voltage, and

$$C = C_{\text{output}} + C_{\text{wire}} + C_{\text{input}}, \quad (2)$$

which describes the output and input capacitance of the transistors and the capacitance introduced by the wire itself. Each time the wire is active, i.e., each time it transports a signal, this power will be dissipated. The other contributor to power is the static power, which is related to the leakage current between wires. Low leakage is therefore an additional and important requirement for the dielectric of choice.

Of interest in this review is the dominance of wire capacitance and the dynamic power dissipation which is influenced significantly by the dielectric constant of the materials between the wires.

Table I is an overview of the expected progress for technology nodes over the coming years based on the ITRS roadmap of 2001.³ The top row refers to the first predicted year of production of the technology node. Each technology node has characteristic dimensions for the transistor (poly-Si gate) and for the interconnecting wires. The pitch is shown because this translates into density of transistors and wires per unit area. The table separates pitches for several wiring levels from the ITRS 2001 roadmap into three categories (local, intermediate, and global wiring). The pitches give a realistic idea of the dimension of the low-*k* dielectric spacing in the various nodes. Because of the presence of other dielectric layers in the dielectric stack, it is necessary to consider an effective k value, which consists of a combination of the k value of the low-*k* dielectric and all other dielectrics between the wires. In the bottom rows on the table, the predicted and effective k value are taken directly from the roadmap. The latter predicts as such the k value designers envision for that node, whereas the former indicates the type of material that will be needed. The effective k value will be higher due to process interactions and the presence of other thin dielectric layers (hard masks) which are necessary to improve process control or to protect the low-*k*-material during processing.

Table I also shows the total capacitance per unit length and the interconnect delay for a 1 mm line that are calculated from the ITRS numbers. The total interconnect capacitance decreases slightly over future nodes, but the RC delay increases significantly. Total capacitance can be traded for resistance and vice versa by changing the geometry of the wire cross-section, but the RC product will always increase for future nodes. It is interesting to compare the wire capacitance and delay with that of the transistors. The specifications of

TABLE I. Characteristic numbers for future technology nodes relating to dimensions and material characteristics from the ITRS 2001 roadmap. The electrical performance was calculated based on these numbers.

Year of production	2001	2004	2007	2010	2013	2016
DRAM 1/2 pitch (nm)	130	90	65	45	32	22
MPU/ASIC 1/2 Pitch (nm)	150	90	65	50	35	25
MPU printed gate length (nm)	90	53	35	25	18	13
MPU physical gate length (nm)	65	37	25	18	13	9
Local wiring						
Local wiring pitch (nm)	350	210	150	105	75	50
Total interconnect capacitance (fF/mm)	192	169	148	127	118	114
Interconnect RC delay 1 mm line (ps)	86	198	342	565	970	2008
Line length where $C_{\text{line}} = C_{\text{gate}}$ ($w = 3L$) (μm) (low power)	1.80	0.94	0.58	0.39	0.26	0.15
Line length where $\tau = RC$ delay (μm) (low power)	172	96	58	39	24	13
Line length where $C_{\text{line}} = C_{\text{gate}}$ ($w = 3L$) (μm) (high performance)	1.24	0.58	0.43	0.32	0.23	0.14
Line length where $\tau = RC$ delay (μm) (high performance)	137	70	44	26	15	9
Intermediate wiring						
Intermediate wiring pitch (nm)	450	265	195	135	95	65
Total interconnect capacitance (fF/mm)	197	173	154	130	120	116
Interconnect RC delay 1 mm line (ps)	53	127	198	348	614	1203
Line length where $C_{\text{line}} = C_{\text{gate}}$ ($w = 3L$) (μm) (low power)	1.75	0.92	0.55	0.38	0.25	0.09
Line length where $\tau = RC$ delay (μm) (low power)	218	120	76	50	30	17
Line length where $C_{\text{line}} = C_{\text{gate}}$ ($w = 3L$) (μm) (high performance)	1.2	0.56	0.42	0.32	0.22	0.08
Line length where $\tau = RC$ delay (μm) (high performance)	174	88	58	33	19	11
Global wiring						
Global wiring pitch (nm)	670	460	290	205	140	100
Total interconnect capacitance (fF/mm)	211	186	167	143	133	128
Interconnect RC delay 1 mm line (ps)	21	37	79	131	248	452
Line length where $C_{\text{line}} = C_{\text{gate}}$ ($w = 3L$) (μm) (low power)	1.63	0.85	0.51	0.34	0.23	0.09
Line length where $\tau = RC$ delay (μm) (low power)	351	223	120	81	47	28
Line length where $C_{\text{line}} = C_{\text{gate}}$ ($w = 3L$) (μm) (high performance)	1.12	0.52	0.38	0.29	0.20	0.08
Line length where $\tau = RC$ delay (μm) (high performance)	280	163	92	54	30	19
Bulk k value	2.7	2.4	2.1	1.9	1.7	1.6
Effective k value	3–3.6	2.6–3.1	2.3–2.7	<2.1	<1.9	<1.6

transistors distinguish between low power and high performance. For both cases the wire length is calculated assuming the capacitance equals that of a gate capacitor. Note that these equivalent lengths are in the submicron range, giving an idea of the importance of wires in the total power budget. Finally, as a figure of merit, the line length is given for which the RC delay equals that of a single high performance or low power transistor. These data clarify how significant the impact of wiring has become in comparison to the transistors. It also shows how electrical system performance will now be a consequence of both transistor and wiring performance.

B. Implementation of low- k dielectrics

It is unclear how close materials for dielectrics will come to the ultimate limit of k equal to unity within the next years. The impact of the dielectric constant on system performance has triggered all the research on new dielectrics as discussed in this review. The chemical industry has been very active in bringing new materials to the market with ever decreasing k values, attempting to comply with the perfor-

mance specifications provided by the microelectronics industry. However, the requirements for compatibility with damascene processing (i.e., the process in which the wires are inlaid in preformed trenches and vias in the dielectric) that are imposed on these materials are stringent, and implementation of materials is often hampered by lack of process compatibility as scaling of feature sizes proceeds (and often accelerates). This has led to new and exciting research areas to solve these problems.

This paper will systematically review the low- k dielectric materials, their classification, the characterization techniques, the properties, and characteristic process interactions. As older materials become unavailable and new materials are developed, this overview does not aim to be exhaustive on materials and will by no means lead to the ultimate choice of a dielectric material. It should be noted that one of the research areas is to achieve a k value of one by introducing air gaps, but even though this is an interesting approach it will not be discussed here.

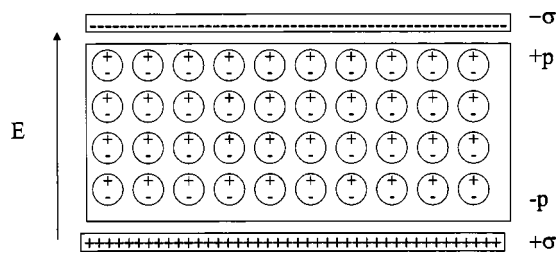


FIG. 1. Schematic cross section of two capacitor plates with surface charge density σ and a dielectric polarized by an electric field E . Each circle denotes a polarization moment.

The aim of this review is to provide a deeper insight into: (i) the requirements for dielectric films and (ii) the possible solutions to solve process incompatibilities. The research field of low- k dielectrics is multidisciplinary and involves physics, organic chemistry, inorganic chemistry, and microelectronics. Each research field has its own viewing angle and often its own nomenclature. An example is the representation of the relative permittivity or dielectric constant by either k or ϵ_r as

$$\epsilon = \epsilon_r \epsilon_0 = k \epsilon_0, \quad (3)$$

with ϵ_0 the permittivity of vacuum.

The microelectronics community has adopted k in contrast to the scientific communities using ϵ_r . In scientific formulas we will use ϵ_r , but we will use k in our discussion. An attempt is made to bring the different fields together and give as wide a scientific view as possible. It is not within the scope of the review to go into technological details. For that we refer to specific literature.⁴

II. DIELECTRIC MATERIALS

A. Capacitance and relative permittivity

The relative permittivity ϵ_r of a medium is defined as the ratio of the capacitances of a capacitor with and without the dielectric in place. The capacitance is described by its charge density σ and plate area A (Fig. 1).

The charge density σ and the magnitude of the applied field E are related as

$$E = \sigma / \epsilon. \quad (4)$$

The charge on the plates arises from the polarizing medium which induces a net charge density p . The electric field between the plates can be written as

$$E = (\sigma - p) / \epsilon_0. \quad (5)$$

Since the electric field in both these equations is the same one obtains

$$p = \left(\frac{\epsilon - \epsilon_0}{\epsilon} \right) \sigma = (\epsilon_r - 1) \epsilon_0 E. \quad (6)$$

The electric susceptibility χ_e is defined as

$$\chi_e = \epsilon_r - 1, \quad (7)$$

and writing the polarization and electric field as vectors, one obtains

$$\mathbf{P} = \chi_e \epsilon_0 \mathbf{E}. \quad (8)$$

The next stage is relating the polarization of the medium, \mathbf{P} , to the polarizability of its molecules. The polarization is the dipole-moment density and equals the mean dipole moment of a molecule, \mathbf{p} , in the medium, multiplied by the number density of molecules N .

The induced dipole moment is proportional to the local electric field \mathbf{E}^* . The local electric field is the total field arising from the applied field and the electric dipoles which that field stimulates in the medium. The polarization of the medium becomes

$$\mathbf{P} = N \mathbf{p} = \alpha N \mathbf{E}^* \quad (9)$$

with α the polarization constant (see next section).

For a continuous dielectric, the Lorentz local field can be derived from electrostatics and is given by

$$\mathbf{E}^* = \mathbf{E} + \mathbf{P} / 3 \epsilon_0. \quad (10)$$

B. Polarization phenomena

The polarizability of a molecule is a measure of its ability to respond to an electric field and acquire an electric dipole moment \mathbf{p} . There are several microscopic mechanisms of polarization in a dielectric material.⁵⁻⁷ Electric dipole moments can be induced by the electric field or can be permanent.

The *induced electric dipole moment* can be a result of two polarization phenomena, i.e., electronic polarization and distortion polarization.

Electronic polarization, α_e , describes the displacement of the cloud of bound electrons with reference to the nucleus under an applied electric field. The atom distorts and the center of the atom's negative charge no longer coincides with the position of the nucleus, resulting in an electric dipole moment. The electric dipole moment of each atom is described by

$$\mathbf{p} = \alpha_e \mathbf{E}^*. \quad (11)$$

Distortion polarization α_d (also often referred to as ionic polarization) relates to the distortion of the position of the nuclei by the applied field, thereby stretching or compressing the bond length, depending on the relative orientation between the ionic bond and the electric field. The molecule is bent and stretched by the applied field and its dipole moment changes accordingly. Nonpolar molecules may acquire an induced dipole moment in an electric field on account of the distortion the field causes in their electronic distributions and nuclear positions.

A polar molecule is a molecule with a permanent electric dipole moment. The permanent dipole moment is a result of the partial charges on the atoms in the molecule that arise from the different electronegativity or other features of bonding. Polar molecules may have their existing dipole moments modified by the applied field. Orientation polarization relates to the phenomenon of a permanent dipole moment as a result of polar molecules.

The total polarization of a medium, composed of polarizable polar molecules, is therefore

$$\mathbf{P} = N \left(\alpha_e + \alpha_d + \frac{\mu^2}{3kT} \right) \mathbf{E}^*, \quad (12)$$

with N the number of molecules per m^3 , μ the orientation polarizability, k the Boltzmann constant, and T the temperature in K.

The terms α_e and α_d represent the electronic and distortion polarization in the molecule, while the term $\mu^2/3kT$ stems from the thermal averaging of permanent electric dipole moments in the presence of an applied field.

The quantitative relation between the relative permittivity and properties of the molecules is described by the Debye equation

$$\frac{\epsilon_r - 1}{\epsilon_r + 2} = \frac{N}{3\epsilon_0} \left(\alpha_e + \alpha_d + \frac{\mu^2}{3kT} \right). \quad (13)$$

The relative permittivity ϵ_r of materials is high if its molecules are polar and highly polarizable. This equation shows that the permittivity is smaller if materials do not contain polar molecules. Reduction of density N and polarizabilities α_e and α_d are also possible ways to decrease the dielectric constant. Reducing the number of ionic bonds in the material minimizes distortion polarization. The electronic polarization is minimized by lowering the electron density in the material, i.e., introducing smaller elements.

The same expression, but without the permanent dipole moment contribution, is called the Clausius–Mossotti equation

$$\frac{\epsilon_r - 1}{\epsilon_r + 2} = \frac{N}{3\epsilon_0} (\alpha_e + \alpha_d). \quad (14)$$

Although the value of the electric dipole moment is extremely important for predicting properties of dielectric materials, their calculation is difficult. In the case of simple molecules the Stark effect⁸ is used to measure the electric dipole moment of molecules for which rotational spectra can be observed. In the case of more complicated systems, the polarizability and permanent dipole moment of molecules can be determined by measuring ϵ_r at a series of temperatures. These measurements facilitate the determination of molar polarizations and their slope and intersect versus $1/T$ give values of dipole moment and polarizability.

C. Film density and relative permittivity

The possibility to lower the molecular polarizability is limited. Equations (12)–(14) show that number of molecules per unit of volume (film density) plays an important role in reduction of the film permittivity. The effect of the density on the film permittivity is stronger than the effect of molecular polarizability since reducing density allows to reduce the dielectric constant to the extreme value close to unity.

Technologically, an important way to reduce the film density is introduction of pores. Generally, porous films can be considered as two-component materials where the solid skeleton has a dielectric constant close to the dense prototype and the second component (pores) has dielectric constant equal to 1. The relative permittivity of porous film ϵ_r directly depends on porosity

$$\begin{aligned} \frac{\epsilon_r - 1}{\epsilon_r + 2} &= P \cdot \frac{(\epsilon_1 - 1)}{(\epsilon_1 + 2)} + (1 - P) \cdot \frac{(\epsilon_2 - 1)}{(\epsilon_2 + 2)} \\ &= (1 - P) \cdot \frac{(\epsilon_2 - 1)}{(\epsilon_2 + 2)}. \end{aligned} \quad (15)$$

In this equation ϵ_1 is permittivity of material inside the pores, ϵ_2 is permittivity of the film skeleton, and P is the film porosity. The term $P \cdot (\epsilon_1 - 1)/(\epsilon_1 + 2)$ is equal to 0 if the pores are empty, as experimentally demonstrated by Hrubesh and co-workers.⁹

D. Relative permittivity and frequency

When the applied electric field is an ac field, the frequency of the signal comes into play. The polarization phenomena described above are very different for applied electric fields with different frequencies.

For an applied field

$$\mathbf{E} = \mathbf{E}_0 e^{-i\omega t} \quad (16)$$

the polarization vector is of the form

$$\mathbf{P} = \epsilon_0 (\epsilon_r - 1) \mathbf{E}_0 e^{-i\omega t} \quad (17)$$

and gives rise to a current density

$$\mathbf{J} = -i\omega\epsilon_0 (\epsilon_r - 1) \mathbf{E}_0 e^{-i\omega t}, \quad (18)$$

which is imaginary as long as ϵ_r is real. This will not always be the case as will be discussed later.

Let us first consider the consequences for the polarization phenomena. Electronic polarization follows the electric field almost instantaneously as only the displacement of bound electrons is involved. The distortion polarization cannot respond as rapidly to fast changing fields since it involves the displacement of entire ions. Both electronic and distortion polarization are subject to a counter-active restoring force, which gives rise to a resonant frequency.

In contrast, orientation polarization requires the motion of complete molecules. For orientation polarization there is no counteractive restoring force. Therefore, it does not give rise to a resonance at a critical frequency, as distortion and electronic polarization do. The orientation polarization is, however, opposed by thermal disorder.

At low frequencies the three polarization phenomena contribute to the real part of the dielectric constant. The maximum frequency for orientation polarization is on the order of 10^9 Hz. Above this frequency distortion and electronic polarization contribute to the dielectric constant up to the resonance frequency for distortion polarization, which is typically in the order of $\sim 10^{13}$ Hz, and beyond that only electronic polarization is defining the dielectric constant. The resonant frequency of the electronic polarization is typically beyond the frequency of visible light at $\sim 10^{15}$ Hz.

It follows from Maxwell's equations that the refractive index relates to the relative permittivity, beyond optical frequencies, as

$$n_r = \epsilon_r^{1/2}. \quad (19)$$

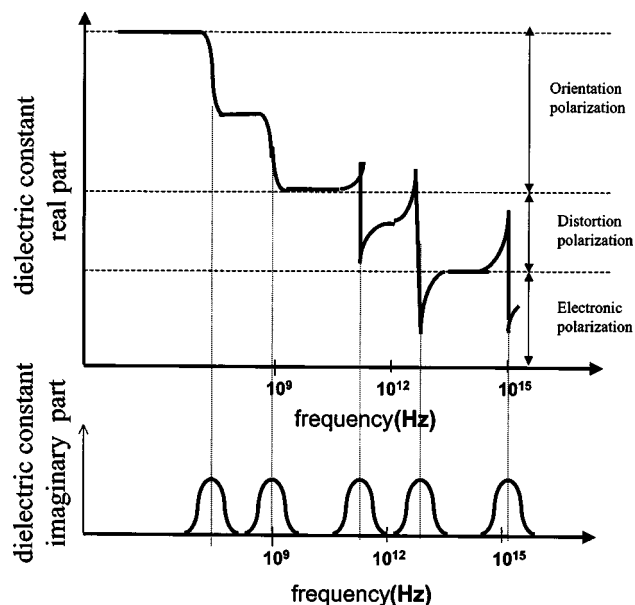


FIG. 2. Schematic curve of the real and imaginary parts of the dielectric constant of a fictive material. This material exhibits two different orientation polarization modes and two different distortion polarization modes.

Because of the relation between the relative permittivity and the molecular polarizability, one can relate n_r to the molecular properties as follows:

$$n_r = \left(\frac{1 + (2\alpha N/3\epsilon_0)}{1 - (\alpha N/3\epsilon_0)} \right)^{1/2} \approx 1 + \frac{\alpha N}{2\epsilon_0}. \quad (20)$$

This expression leads to the Lorenz–Lorentz formula

$$\frac{n_r^2 - 1}{n_r^2 + 2} = \frac{N\alpha(\omega)}{3\epsilon_0}. \quad (21)$$

The characteristic response of the different polarization phenomena to the electric field results in a frequency dependence which has not only an impact on the real part of the dielectric constant, but the imaginary part is related to the counteractive restoring forces in case of electronic and distortion polarization, and to the thermal disorder in case of orientation polarization. The imaginary component of the dielectric constant corresponds to a current density within the dielectric that is no longer exactly $\pi/2$ out of phase with the electric field. It is as such responsible for the dissipation in the dielectric at the specific frequencies indicated in Fig. 2.

From the frequency dependence one should note that orientation polarization in low- k dielectrics should be prevented as much as possible, not only for its contribution to the dielectric constant but more importantly for the imaginary part of the dielectric constant. Indeed orientation polarization leads to heat dissipation in a frequency range that is envisioned within the application frequencies of microelectronics systems.

III. CONSTITUTIVE AND SUBTRACTIVE POROUS DIELECTRICS

In this section low- k materials are classified according to their basic composition and structure. Subsequently, the ma-

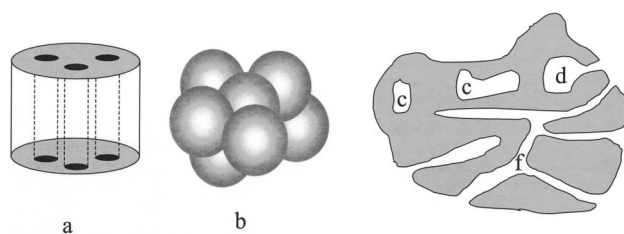


FIG. 3. Idealized pore structures (a) cylindrical pores; (b) voids between packed spheres and schematic boundary structure showing (c) closed (latent) pores; (d) ink bottle; (e) funnel; and (f) open pores.

jor deposition techniques are described. Finally, the various ways to create and control porosity are discussed.

We will follow the recommendations for the characterization of porous solids as given by the International Union for Pure and Applied Chemistry (IUPAC).¹⁰ In their introduction it is stated that most materials are to some extent porous. This holds also for the dielectrics and therefore more specific nomenclature is mandatory. The description of porous solids is complicated by the existence of different shapes of pores, connections between the pores, and the distribution in size of pores. According to the IUPAC definition micropores have diameters smaller than 2 nm, while mesopores have diameters between 2 and 50 nm. In this review pore size will be referred to denote the diameter.

The importance of the interconnectivity of the pores will be shown in later sections. The terms microconnectivity and mesoconnectivity are introduced, referring to the same dimensions for the connectivity as for the pore sizes. As will be discussed in detail below, porous materials can be formed by several routes. We will follow the IUPAC nomenclature in defining materials constitutively porous if their final structure mainly depends on the original, as-deposited, arrangement. Subtractive porous materials are those for which certain parts of the original structure are selectively removed to create pores, as is the case, e.g., for pore formation by thermal desorption of some particles or porogens in multiphase solids.

Figure 3 shows idealized pore structures. In order to interpret characterization results and correlate pore size with physical models, it is important to make assumptions about the pore geometry. The complexity of the real porous texture of materials is such that even a theoretical description of the texture usually entails the introduction of simplified assumptions. No single experimental method provides the absolute value of parameters such as porosity, surface area, and pore size. Each gives a characteristic value which depends on the principles involved and the nature of the probe used.¹⁰

Porosity is defined as the fraction p of the total volume of the film comprised by pores: $p = V_p/V$, where V_p is pore volume and V is total volume of the film. Pores are defined to be “open” if they are accessible by the probe. Pores with a size smaller than the probe diameter are inaccessible and therefore by definition “closed.” Note, however, that different analytical methods will provide different thresholds of open and closed pores.

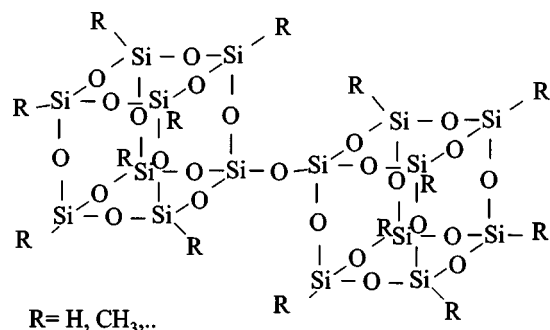


FIG. 4. Structure of elementary units of SSQ dielectric materials.

Specific surface area is defined as the accessible area of solid surface per unit mass of material. This value also depends on the characterization method employed and size of the probe.

A. Classification of constitutive porous materials

1. Silsesquioxane (SSQ) based

For SSQ based materials silsesquioxane is the elementary unit. Silsesquioxanes, or T-resins, are organic-inorganic polymers with the empirical formula $(R-SiO_{3/2})_n$. These compounds derive their name from the one-half (3/2) or sesquistoichiometry of oxygen bound to silicon. Its alternate name "T-resin" is derived from the presence of three oxygen substituents on silicon (tri-substituted). The most common representatives are a ladder-type structure, and a cage structure containing eight silicon atoms placed at the vertices of a cube (T_8 cube) (Fig. 4). Substituents (R) on silicon can include hydrogen, alkyl, alkenyl, alkoxy, and aryl. Many silsesquioxanes have reasonable solubility in common organic

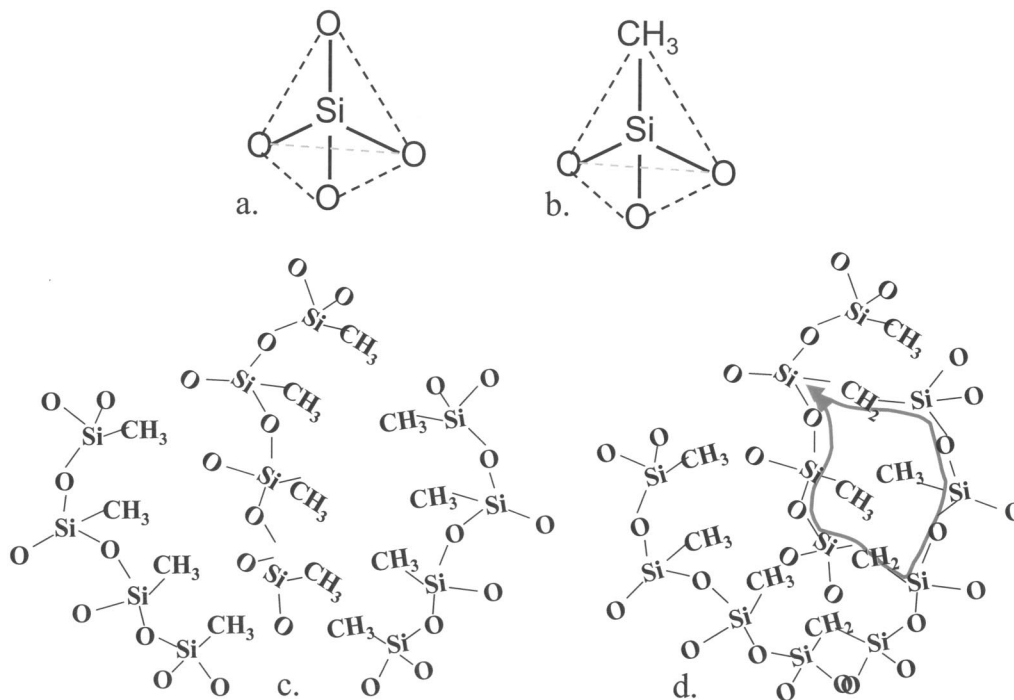
solvents due to their organic substitution on Si. The organic substitutes provide low density and low dielectric constant matrix material. The lower dielectric constant of the matrix material is also attributed to a low polarizability of the Si-R bond in comparison with the Si-O bond in SiO_2 .

The silsesquioxane based materials for microelectronic application are mainly hydrogen-silsesquioxane (HSQ), and methyl-silsesquioxane or $CH_3-SiO_{3/2}$ (MSQ). The elementary units of these materials are depicted in Fig. 4.

MSQ materials have a lower dielectric constant as compared to HSQ because of the larger size of the CH_3 group (2.8 and 3.0–3.2, respectively) and lower polarizability of the Si- CH_3 bond as compared to Si-H. The materials being evaluated for microelectronics applications are not solely MSQ but mixtures of MSQ and HSQ. For simplicity we will refer to these mixtures as MSQ based dielectrics.

2. Silica based

The silica based materials have the tetrahedral basic structure of SiO_2 . Silica has a molecular structure in which each Si atom is bonded to four oxygen atoms, and each oxygen atom to two silicon atoms ($SiO_{4/2}$) [Fig. 5(a)]. Each silicon atom is at the center of a regular tetrahedron of oxygen atoms. All types of silica have fairly dense structures and high chemical and thermal stability. The density of different silica types varies between 2 and 3 g/cm³. Amorphous silica films, used in microelectronics, have a density of 2.1–2.3 g/cm³ and a refractive index of 1.46. The high frequency dispersion of dielectric constant ($k \approx 4$ in the low frequency region and $k \approx 2.15$ in the range of visible light) is related to the high polarizability of the Si-O bonds (distortion polarization). Lowering the k value can be accomplished by replacing the Si-O bond with the less polarizable Si-F bond

FIG. 5. Elementary unit of: (a) SiO_2 , of (b) C doped silica glass and schematic bonding structure (c) without and (d) with cross linking.

producing F doped silica glasses (FSG). Another approach is doping the silicate glasses with C by introducing CH_3 groups, which also lowers the k value. Moreover, both fluorine and carbon increase the interatomic distances or “free volume” of silica which provides an additional decrease of dielectric constant. The elementary unit of C-doped silica glasses is presented schematically in Fig. 5. These elementary units form long chains with a different degrees of cross-linking.

Typical densities of C-doped silica glasses are between 1.2 and 1.4 g/cm³, which is significantly lower than SiO_2 . C-doped silica films have dielectric constants close to 2.6–3. The k value of the material depends on the number of CH_3 groups built into the structure since they lower both polarity and density of the material by steric hindrance.

3. Organic polymers

Organic polymers can be divided into two different groups with respect to the behavior of their dielectric constant. Non-polar (so called low-loss) polymers contain molecules with almost purely covalent bonds. Since they mainly consist of nonpolar C–C bonds, the dielectric constant can be estimated using only density and chemical composition.¹¹ The relation between dielectric constant and density is given by the Clausius–Mossotti (Lorentz–Lorenz) Eq. (21). Low-loss polymers, by definition, have dielectric constants which are independent of frequency. The dielectric loss observed in these polymers is the convolution of two effects: the presence of a dipole that couples to the electric field and a suitable (thermal) motion in the polymer that gives rise to a dispersion. The nature and origin of the dipoles in low-loss polymers can be related to impurities in the starting materials (e.g., residual catalyst) or unsaturated terminal groups of a polymer chain.

Polar polymers do not have low loss, but rather contain atoms of different electronegativity which give rise to an asymmetric charge distribution. Thus polar polymers have higher dielectric loss and a dielectric constant which depends on the frequency and temperature at which they are evaluated.

Several organic polymers, synthesized in research laboratories, have been analyzed and reported in different articles published over the last 5 yr.^{12–14} Applicability of some of these films is limited because of their low thermal stability, softness, and incompatibility with traditional technological processes developed for SiO_2 based dielectrics.

Saturated hydrocarbons have a lower polarizability than unsaturated, conjugated and aromatic hydrocarbons. Therefore, they may provide the lowest k value. However, the aliphatic C–C, C–H, and C–N bonds generally become unstable at $T \geq 300$ – 400°C and in some cases at even lower temperatures. Only materials composed of nonaliphatic C–C, C–O, C–N, and C–S bonds, aromatic structures, and cross-linked or ladder structures can withstand the temperatures necessary for interconnect technology (450 – 500°C). Fluorination generally decreases the dielectric constant and improves thermal stability partly because the C–F bond is stronger than C–H. Fluorine substitution also lowers the k value by decreasing the polarizability and increasing the free

volume. Substitution of hydrogen with F or $-\text{CF}_3$ groups decreases the electronic polarizability due to strong electron-withdrawing inductive effects of the F atom. Most of the organic low- k films with sufficient thermal stability have dielectric constants close to 2.6–2.8.

4. Amorphous carbon

Another class of low- k materials is so-called “amorphous carbon” (very often fluorinated and/or hydrogenated).^{15,16} The material is usually obtained by plasma-assisted chemical vapor deposition methods using a discharge with fluoro-carbon gases.^{17,18} This material does not attract much attention due to difficulties with combining sufficiently low- k values with acceptable thermal stability and mechanical properties,¹⁹ and will not be discussed in our review.

B. Deposition by spin on

1. Constitutive porous dielectrics

The spin-on deposition technique is a well known deposition method for dielectric films. It is particularly suitable where depositions with good planarization and gap fill properties are required. Inorganic and organic films can be deposited by spin-on, and their final structure can be either amorphous or crystalline. The dielectric precursors should be available in soluble form or “sol,” i.e., a dispersed solution of primary particles/polymers (solid part) mixed with a solvent (liquid part).

Thin film coating is performed by dispensing a liquid precursor at the center of the substrate, which is placed on a spinner. This is commonly done at room temperature and ambient pressure. Rotation of the substrate creates centrifugal forces that ensure a uniform distribution of material on the surface. The thickness of the coating is a result of the balance between centrifugal forces (dependent on the rotation speed ω) and viscous forces, determined by the viscosity of the solution. Normally, the spinning step is followed by heating or “bake” at temperatures typically below 250°C , for removal of the solvents. The latter step can also initiate cross-linking of the film. Finally, a sintering at temperatures varying from 350 to 600°C (“cure”) is required to obtain a stable film. This “cure” step induces the final cross-linking of the polymer chains and results in a mechanically stable film structure.

Spin-on amorphous dielectrics with an inorganic backbone are referred to as spin-on glasses (SOGs). There exist various specific sol–gel reactions,²⁰ and they usually a combination of hydrolysis and condensation processes. The common feature in the hydrolysis is that there is a transition from Si–OR or Si–R functional groups to Si–OH silanol groups in the presence of moisture. Consequently, two or more silanol groups can condensate into a Si–O–Si structure, accompanied by the elimination of H_2O .

After spinning, the sol undergoes a sharp increase in viscosity and transforms into a “wet gel.” The mechanisms at the molecular level promoting this sudden transition are not well understood. The wet gel is a somewhat rigid substance yet consisting of a liquid and a solid component. The

solid part is formed by a three dimensional network of linked polymers spanning throughout the film, while the liquid fills the free space surrounding the solid part. Subsequently, the gel is dried by a thermal step at a moderate temperature (bake). During this bake step, the original solvents are removed and the film undergoes a major weight and volume loss of up to 50%. For thin films, this shrinkage is accommodated only in the direction perpendicular to the substrate plane. Based on the technique used for drying, a distinction between xerogels and aerogels can be made. Xerogels are formed through conventional drying by evaporation, while aerogels use supercritical drying of solvents.

The drying of the wet gel is a critical process for promoting constitutive porosity in the films. Most of this constitutive porosity is however lost during subsequent thermal steps, especially “cure,” leading to a densification of the film.

For the spin on deposition of organic polymers, the polymer weight and solution concentration are tuned to enable spin on deposition. After deposition, the polymer is thermally cured to an insoluble film by cross-linking.

2. Subtractive porous dielectrics

Numerous methods of introducing subtractive porosity into spin-on deposited materials exist, but they can be divided into two main categories. The first category groups all materials where the porosity is introduced exclusively through sol-gel processes, while the second group includes the materials where this porosity is formed through the use of sacrificial “nanoparticles” (also called “porogens”) that are desorbed during film cure.

Subtractive porosity by sol-gel based techniques There exist two main approaches exclusively based on sol-gel techniques to the formation of subtractive porosity into a film: the first takes advantage of *aging* processes and the second relies on a hierarchical organization of the primary particles in the sol (self-assembly).

The formation of a more or less rigid skeleton structure before extraction of the liquid from a wet gel is a key point in the formation of high porosity materials. Even if the gel point is reached after material spinning, a long time is still required before the hydrolysis and condensation reactions are complete. For this purpose, an additional step (aging) before drying the wet gel is introduced. The aim of this step is to accelerate the sol-gel reactions, typically by relying on the pH and the water content in the ambient. These are diffusion controlled processes and dedicated equipment (aging chamber) is normally required. Once the network structure is strengthened, extraction of the solvent can take place without collapse of the network backbone. Examples exist of both xerogels and aerogels prepared with high porosity in combination with an aging step. The level of residual porosity is generally tuned through the ratio of solvent to solid content in the sol.

Aerogels are based on supercritical drying of the wet gel after aging. This process is not suited for all solvents since it implies relatively high pressure and temperature, so a supplementary solvent exchange step is added. This step aims to remove the original solvent in the sol by a less hazardous

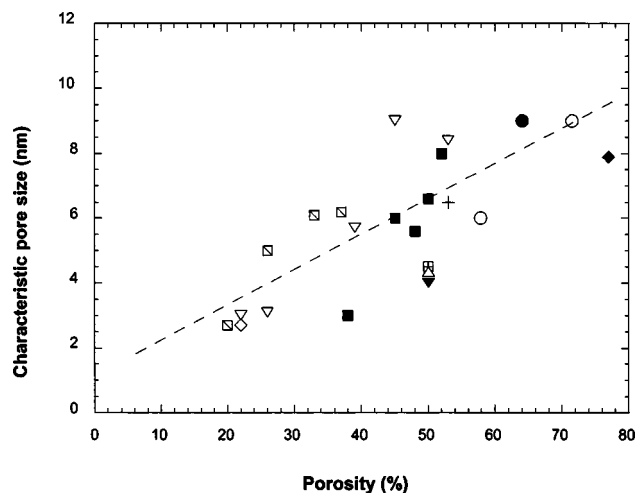


FIG. 6. Average pore size vs total porosity for several sol-gel based materials (data points include porous SiO_2 , HSQ, and MSQ based dielectrics, the average pore size was determined by several techniques (see Ref. 24).

solvent like, in most cases, CO_2 ($T_c = 31^\circ\text{C}$, $P_c = 1050$ psi). Aerogel based materials are of interest because of their tunable thermal and electrical properties. The synthesis of one of the early silica-based dielectrics for microelectronics applications with a dielectric constant approaching 2.0 was based on this method.^{21,22}

For xerogels the precursor can be a sol prepared with two types of solvents that have significantly different evaporation temperatures. The first type is a highly volatile solvent that is removed through simple evaporation during gel drying at low temperatures. Subsequently the film undergoes an aging step and then a thermal step at higher temperature (typically between 100 and 200 $^\circ\text{C}$). The second thermal step aims at the evaporation of the second solvent (high boiling point solvent) once the film structure is strengthened. The residual porosity in the film is related to the quantity of high boiling point solvent present in the sol.²³

For subtractive dielectric films based on aging techniques, there is a strong indication that the pore size and the total porosity in the film are related. In Fig. 6 the average pore size versus total porosity is presented for several silica and SSQ based films.²⁴ There is a clear trend of increasing total porosity leading to larger pore sizes. As will be discussed below, the control of pore size and pore distribution is key in processing porous materials. Subtractive techniques based on aging do not allow independent control of pore size and total porosity.

In sol-gel science numerous studies have been performed in the synthesis of self-assembled microporous materials. These are mainly zeolites, microporous crystalline solids with well-defined structures. Zeolites generally contain silicon, aluminum, and oxygen, together with cations. They are also widely found in nature as minerals. Their synthesis by sol-gel processes allows the formation of films or membranes. Combining zeolite crystallites with surfactants or a molecular-sized “template” in solution favors an organized aggregation of the primary crystallites.^{25,26} Supramolecular assemblies can be used to template in the same way as materials with pore sizes in the upper range of the mi-

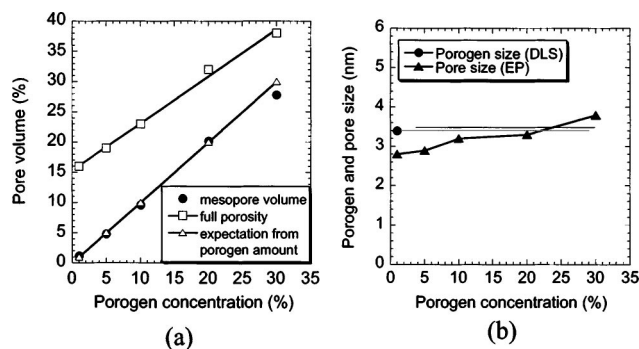


FIG. 7. Pore volume (a) and pore size (b) vs porogen loading for an MSQ based material prepared using macromolecular porogen to create subtractive porosity. Pore size measured by EP is almost independent of porosity and equal to the porogen macromolecule size determined by dynamic light scattering (DLS) (see Ref. 33).

croporous regime (approaching 2.0 nm), which are also able to incorporate more porosity.²⁷ Hierarchical ordering of the aggregates by preferential solvent evaporation during spin coating is reported for a solution of surfactants, swelling agent and soluble silica. By this method, ordered materials with dielectric constant as low as 1.3 have been synthesized.^{25,28} In the self-assembly case, the final film porosity and pore structure is therefore related to the way in which the primary particles are assembled and ordered.

Overall, the pore structure of films based on sol-gel processes depends: (i) on the size and structure of the primary particles/polymers formed by the condensation reactions, (ii) on the organization of these structures, and (iii) on the type of the gel drying process.²⁹ Within the sol-gel category, materials engineered by self-assembly techniques show superior control on pore structure and size distribution than xerogels and aerogels. In particular, the self-assembly approach by templating surfactant agents can lead to pores in ordered structures with narrow pore size distribution determined by the surfactant supramolecular size.^{30,31}

Subtractive porosity by macromolecular porogens This technique is based on the addition in the dielectric precursor of molecular or supramolecular particles ("porogens") with tailored thermal stability.³² The stability of these particles is such that they are not affected by the coating drying step, and they are removed by pyrolysis during final film sintering or cure (i.e., at temperatures typically in the range from 300 to 400 °C). Their volume distribution in the film at the moment of desorption represents the template for the residual micro- or mesopores in the layer. In the ideal case, the film's final porous fraction is directly related to the amount of porogen as a function of the total solid part in the precursor solution (porogen load), and the size of the sacrificial particles is directly related to the final pore size.³² An example of a material for which the pore size and porosity, or the pore size and porogen load can be controlled independently is shown in Fig. 7.³³

In practice, there are some requirements in order to maintain the relationship between sacrificial particles, pores and porosity. First, the sacrificial material should be chemically compatible with the network (or matrix) material, in order to avoid phase separation. Second, the sacrificial par-

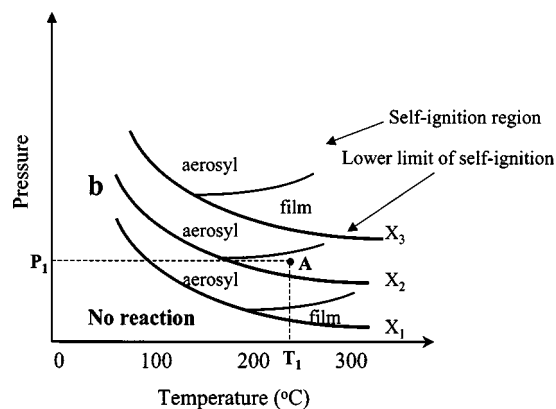


FIG. 8. SiH_4 oxidation near the first limit of self-ignition at different S/V ratios ($X_3 > X_2 > X_1$) (see Ref. 43). Point A (P_1, T_1) corresponds to the film formation at $S/V = X_2$, powder formation at $S/V = X_1$ and no solid product formation at $S/V = X_3$.

ticles should be uniformly distributed throughout the film volume, in order to avoid coalescence of pores.³⁴

There are two ways in which the sacrificial nanoparticles are brought into the dielectric precursor solution. One method is dispersion of porogens in the solution.^{35,36} The second is chemically linking sacrificial particles (grafted) to the network polymers.³⁷ This second method grants an inherent control of the volume distribution of porogens in the dielectric film.

One advantage of the nanoparticle template approach is that the film has a higher degree of cross-linking when the pores are created. The porous structure is, therefore, less affected by further densification than compared to the case of sol-gel based pore formation. Also, closed mesoporosity can be obtained, within certain boundary conditions related to the nature and total load of porogens.

C. Chemical vapor deposition (CVD)

1. Constitutive porosity in silica by deposition

The fundamental principles of CVD involve a wide variety of scientific and technical principles including gas-phase reaction chemistry, thermodynamics, heat and material transfer, fluid mechanics, surface and plasma reactions, thin film growth mechanism, and reactors engineering. Active intermediates and structural units are formed in the gas phase, before being inserted in the matrix of the growing layer.^{38–40} A typical example is deposition of silica layers by silane oxidation. Active intermediates (SiH_3 , SiH_3OH etc.) are formed in the gas phase by thermal initiation and followed chain-branch reaction.^{41,42} The lifetime and concentration of the active intermediates in the gas phase is proportional to the reactor volume (V) and inversely proportional to the internal surface area (S) of the reactor including the wafer surface because the chain-branch reactions are mainly terminated by the surface. If the S/V ratio is too high, all intermediates necessary for film formation are deactivated on the reactor and sample surfaces and no solid product formation is observed (Fig. 8). If the S/V ratio is sufficiently small, then concentration of intermediates in the gas phase is too high and further transformations mainly occur via polymer-

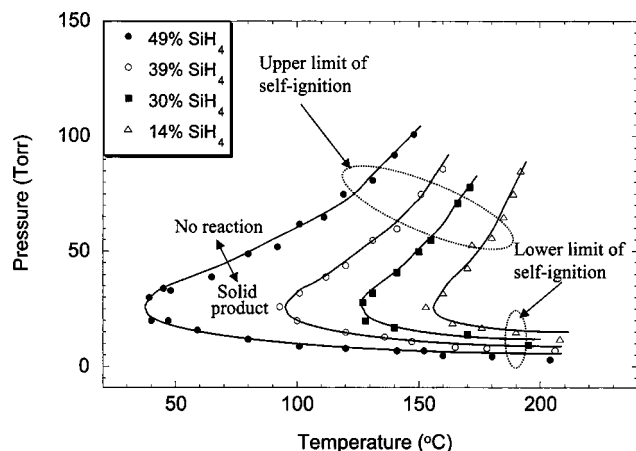


FIG. 9. Self-ignition regions of a silane-oxygen mixture at different SiH_4 concentrations. Figure redrawn from Ref. 42.

ization reactions forming powder like product (aerosyl). Only in the optimal S/V range, a solid film is deposited with a chemical composition close to SiO_2 , but different structural groups, which are typical for aerosyl, are also observed ($\text{HOSiO}_{3/2}$, $(\text{OH})_2\text{SiO}_{2/2}$, $\text{HSiO}_{3/2}$ etc.). Therefore, important parameters to achieve constitutive porosity are the S/V ratio, the deposition temperature, and pressure.^{43–45} These parameters define the limits of self-ignition of SiH_4 . Self-ignition (thermal explosion) represents the rapid increase of reaction rate with temperature for the kinetics of chain-branch exothermic reactions. The acceleration of the reaction rate results in a faster temperature rise upon which the process gets an autocatalytic character. The occurrence of an ignition depends on temperature, pressure, and reactants concentration. Increasing the pressure takes the system through the lower limit of self-ignition. The chain-branch reaction is terminated by the upper limit of self-ignition due to the increase of three-particle collisions in the gas phase. The self-ignition region is defined by a lower (at low pressure) and an upper limit (high pressure) and depends on pressure and temperature as shown in Fig. 9.^{42,46} For the case at hand, formation of a solid product occurs inside the self-ignition region in which solid SiO_2 and gas phase H_2O products are formed in a finite range of SiH_4/O_2 concentrations. Constitutively porous films are formed in conditions close to the region of powder formation.

Similar phenomena are observed during plasma enhanced chemical vapor deposition (PECVD). The concentration of active intermediates in the gas phase depends on plasma power. Therefore, regions of nonstable discharge (low concentration of intermediates), powder, dense, and low-density film formation are also observed as function of plasma power and geometrical factors of the plasma reactor.⁴⁷ Figure 10 shows how powder and film formation depend on experimental conditions. Decreasing temperature and the plasma power shifts the region of film formation to lower ethylene flow suggesting similarity between CVD and PECVD.⁴⁷ In both cases any changes decreasing gas phase concentration of intermediates shifts the process to the region of film formation. Limited incorporation of agglomerates in the gas phase results in porous films. For the deposi-

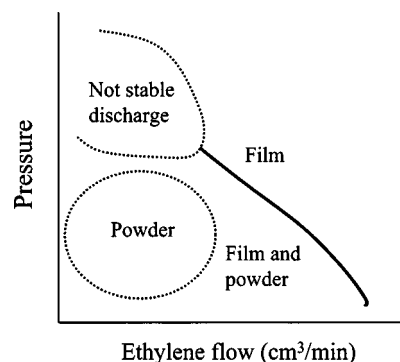


FIG. 10. Powder and dense film formation regions in PECVD of polyethylene. Figure redrawn from Ref. 47.

tion of SiC and SiOCH films from trimethylsilane (3MS) it was observed that the dielectric constant increases with increasing temperature, total flow, rf power; and decreasing 3MS concentration. The dependence of the dielectric constant on pressure goes through a maximum above which the dielectric constant decreases again.

2. Constitutive porosity in silica by doping

The semiconductor industry has long relied on insulating films of silicon dioxide so it is not surprising that most of the attempts at producing low- k materials by CVD have been with doped versions of this material. These dopants have to provide a decrease of the volume polarizability of the film matrix and/or a decrease in film density to lower the k value.

The main dopants used to date have been fluorine and carbon in the form of alkyl groups. Introduction of these groups is done by replacing standard silane (SiH_4) by fluoro- and alkylsilanes like $\text{Si}_2\text{H}_2\text{F}_2$ or methylsilanes $(\text{CH}_3)_x\text{SiH}_y$, where $(x+y)=4$. Fluorine has the effect of lowering the distortion polarization contribution, which minimizes the response of molecules within the film to an applied electric field. Doping a film with alkyl groups terminates some of the silicon bonds within the oxide lattice and lowers the electronic polarizability of the film. The relatively large molecular volume of the alkyl groups decreases the film density. Moreover, lower thermal stability of Si-F and Si-alkyl groups allows for the generation of additional porosity by their removal during the deposition or postdeposition annealing of the film. Huge numbers of F-containing precursors have already been evaluated to deposit low- k FSG films.^{48–53} It should be noted, however, that in some cases thermal annealing leads to a densification of the silica matrix, while in other cases removal of the dopants does not change the matrix structure and highly porous films can be prepared. Thermal annealing of F-doped silica increases the film density.^{54,55} In the case of C-doped silica, thermal annealing allows for the preparation of highly porous low- k films.^{56,57} Precursors for CVD deposition of C-doped silica (silicon oxycarbides) have also been developed, but information related to most of these compounds is still not systemized.^{58–60} Generally, SiOCH films have a constitutive porosity of about 5%–15% with a pore size of about 1 nm.⁶¹

Properties of methyl groups incorporated into the SiOCH dielectric layer during CVD with different precursors have been proposed.^{62,63} SiOCH have been deposited by pulsed plasma oxidation of monomethylsilane H_3SiCH_3 (1MS), dimethylsilane $\text{H}_2\text{Si}(\text{CH}_3)_2$ (2MS), and trimethylsilane $\text{HSi}(\text{CH}_3)_3$ (3MS) and tetra-methylsilane $\text{Si}(\text{CH}_3)_4$ (4MS). Solid-state nuclear magnetic resonance (NMR) (^1H , ^{13}C , and ^{29}Si NMR) was used to determine the network structure of these low- k films. The focus was on ^{29}Si (or Si^*) NMR which achieves superior resolution chemical bonding environments.

The primary structures of $(\text{SiO})\text{Si}^*(\text{CH}_3)_3$, $(\text{SiO})_2\text{Si}^*(\text{CH}_3)_2$, $(\text{SiO})_3\text{Si}^*(\text{CH}_3)$, and $(\text{SiO})_4\text{Si}^*$ are referred to as M , D , T and Q configurations, respectively. In the case of T , D , and M configurations the other silicon bonds are terminated by CH_3 , H , and/or OH groups. It is interesting to note that the highest number of Q configurations was found in films obtained by oxidation of 2MS. The intensity of the Q configuration in the case of 1MS and 3MS is not so pronounced but they contain different ratios of M , D , and T configurations. 4MS and 3MS films are qualitatively and quantitatively very similar. The 1 MS film is relatively CH_3 poor and hydrogen rich, rendering it more prone to hydrolyzation. Hydrolyzation results in a material with more polarity and eventually higher density. The optimization of the network structure is extremely important to reduce polarity and therefore dielectric constant. All these facts suggest that optimizing thermal anneal is instrumental in improving the properties of CVD SiOCH films.

3. Subtractive porosity

Recently, various techniques have been employed to produce CVD oxycarbide (SiOCH) films with subtractive porosity.

One method utilizes a multiphase deposition. The SiOCH precursor tetramethylcyclotetrasiloxane (TMCTS) is mixed with a thermally unstable CH_x phase during deposition.^{64,65} This unstable phase is thermally decomposed and removed from the film during subsequent anneal (4 h at 400 °C) leaving behind pores. The resulting porosity depends on the CH_x/TMCTS ratio and can be as high as 30%–40% for a 1/2 ratio.⁵⁷ The mean pore size is about 2 nm and Fig. 11 plots the obtained dielectric constant as a function of CH_x/TMCTS ratio.

It should be noted that an alternative deposition method exists that produces films with rather large pores (up to 4 nm) and k value of 2.2. However, information on the exact deposition method has not been disclosed.⁶⁶

Another method uses chemical etching of a constitutively porous material from within the pores. An example is a film deposited from a 3-methylsilane (3MS) precursor, that is then etched with HF acid. The starter film is constitutively porous with 10% porosity and a mean pore size of about 1 nm. Using a 2% HF solution, both the mean pore size and the porosity can be increased.⁶⁷ The material is etched equally at the top surface and within the pores with a very low etch rate of about 0.6 nm/min. Such a low etch rate does not produce significant thickness loss for several minutes of etching while the relative effect on pore size is significant.

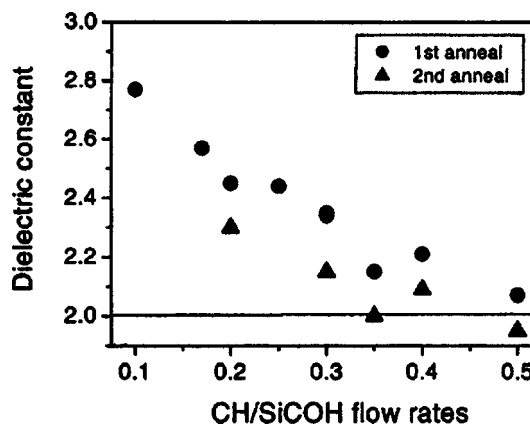


FIG. 11. The dielectric constant as a function of the ratio of the precursor flow rates (reprinted with permission) (see Ref. 57).

After etching the film remains hydrophobic as no water peak is observed in the Fourier transform infrared (FTIR) spectra, and the water contact angle maintains a value of 90° after modification. The nonselective etch does not result in detectable compositional changes as indicated by FTIR and x-ray photoemission spectroscopy (XPS) analysis. The resulting porosity and pore size depend on etch time and can reach 60% and 8 nm, respectively, after 8 min of HF dip (see Fig. 12). Etched films have k values down to 1.8 at highest porosity.⁶⁸

The data on dielectric constant versus porosity are summarized in Figs. 13 and 14, confirming that the k value is primarily determined by porosity.

IV. CHARACTERIZATION TECHNIQUES

In this section, some specific characterization techniques limited to those techniques that are characteristic for either structured dielectrics or for porous dielectrics are discussed.

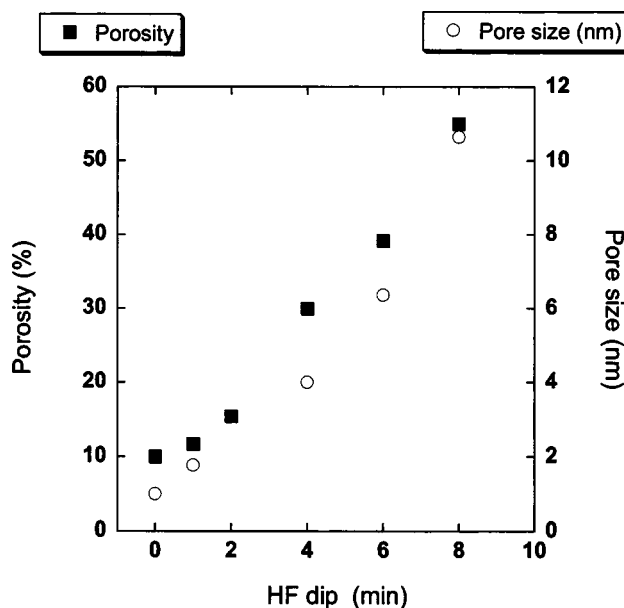


FIG. 12. Porosity and mean pore size of 3MS-based SiOCH film as a function of 2% HF treatment time.

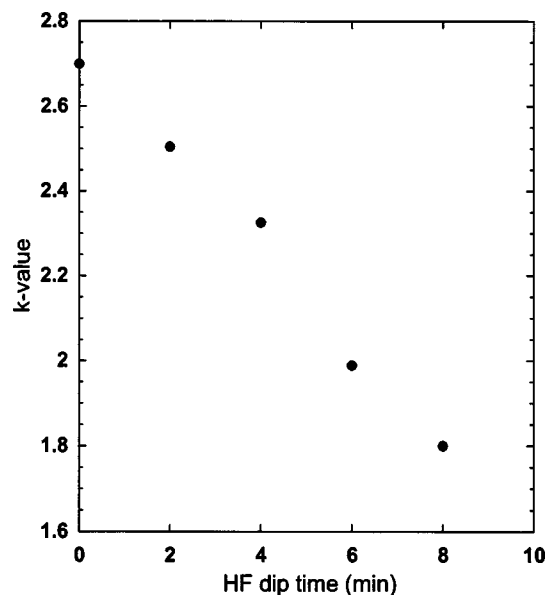


FIG. 13. The dielectric constant (measured in vertical MIM configuration) of 3MS-based SiOCH film as a function of treatment time in 2% HF.

For a description of commonly used characterization methods for dielectrics, such as XPS, Rutherford backscattering spectroscopy (RBS), elastic recoil detection (ERD), transmission electron microscopy (TEM), electron energy loss spectroscopy (EELS), and atomic force microscopy (AFM), we refer to the excellent review by Green *et al.*⁶⁹

A. Composition

1. Fourier transform infrared spectroscopy (FTIR)

FTIR is one method for characterization low- k dielectrics in terms of composition and bond structure. The technique is based on the absorbance of infrared radiation and is sensitive to bulk changes in the rotational, bending, and stretching vibrational modes of the molecules in the film. FTIR is an extremely useful technique to verify the composition of the film before and after processing steps. For po-

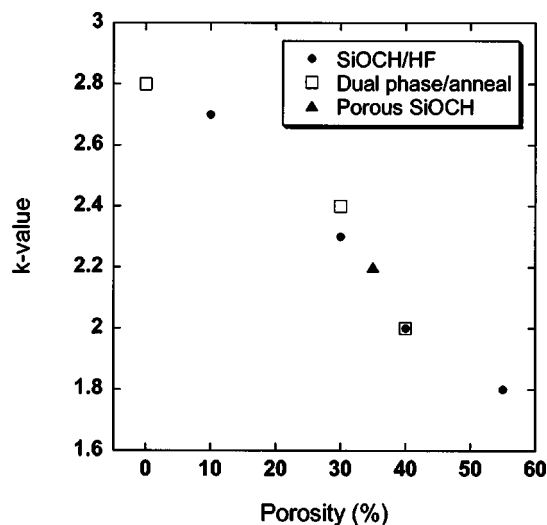


FIG. 14. The dielectric constant versus total porosity for different SiOCH materials with subtractive porosity (see Refs. 57 and 66).

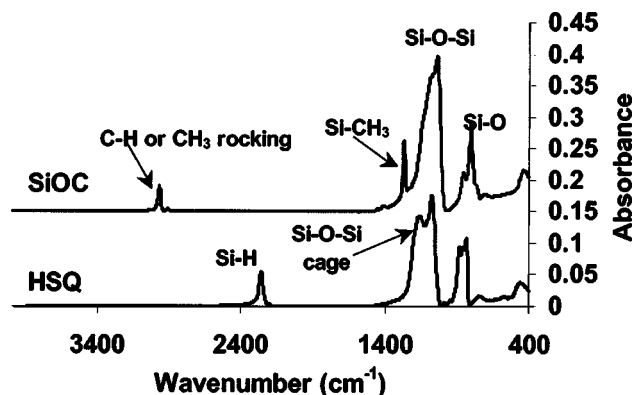


FIG. 15. FTIR spectra of HSQ and SiOCH-based thin dielectric films on Si. Both films are 400 nm thick. Both materials are characterized by a Si–O–Si backbone, with stretch band absorbance peaks in the 1000–1200 cm^{-1} region. In the HSQ spectrum both small (1070 cm^{-1}) and large angle (1150 cm^{-1} , caged structure) stretch band peaks are present, while in the SiOCH spectrum only the small angle Si–O–Si absorbance peak is present. Absorbance peaks from the –H and – CH_x terminating groups are also observed.

rous dielectrics, due to their large internal porous surface, bulk changes are detected as a consequence of minute changes at the pore walls.

Typical absorbance spectra of HSQ- and SiOCH-based films are shown in Fig. 15. Both possess a Si–O–Si backbone with dominant stretching vibrations in the 1000–1200 cm^{-1} region. In the HSQ spectrum both small (around 1070 cm^{-1}) and large (around 1150 cm^{-1}) angle stretch bands are present, while in the SiOCH spectrum only the peak related to the small angle Si–O–Si absorbance can be observed. The absorbance peak around 2250 cm^{-1} is attributed to the H-functional group. CH_x terminating groups give rise to stretch bands in the region 2800–3200 cm^{-1} , and the band around 1270 cm^{-1} is attributed to – CH_3 groups. In Fig. 16 absorbance spectra of a thin aromatic polymer film are shown. The absorbance peaks in the region 400–1500 cm^{-1} are due to complex ring deformation of the aromatic structure. Overall, it can be seen that the absorbance in the infrared region is significantly lower than that for the inorganic Si based material with equivalent thickness (Fig. 15). This indicates that

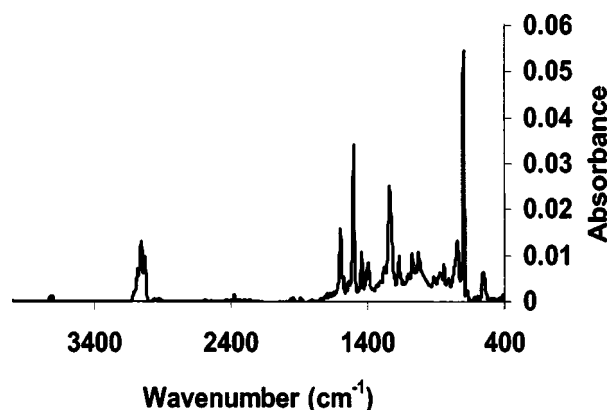


FIG. 16. FTIR spectrum of a dielectric polymer on Si, 400 nm thick film. The absorbance peaks in the region 400–1500 cm^{-1} are due to complex ring deformation of the aromatic structure, while the peaks around 3200 cm^{-1} are attributed to CH_x stretch band absorbance.

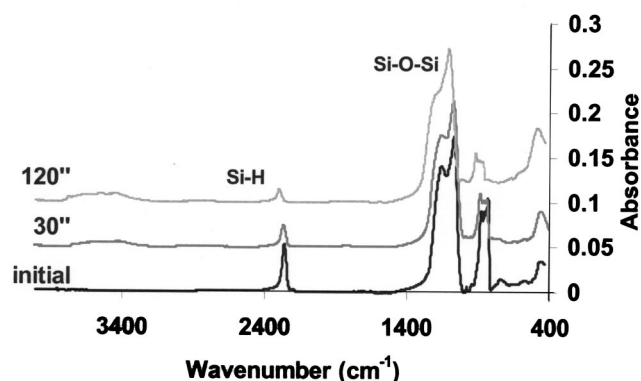


FIG. 17. Absorbance spectra of HSQ-based thin films. The pristine spectrum is compared to the spectra of films after a H_2 plasma treatment for 30 and 60 s ($T=230^\circ\text{C}$, $P=1$ Torr), showing the loss of Si-H hydrophobic groups (2250 cm^{-1}) due to the treatment and consequently the emergence of a peak in the $3200\text{--}3700\text{ cm}^{-1}$ region due to moisture adsorption in the bulk of the film.

the contribution of the distortion polarization is sensibly lower for the organic polymer than for an SSQ- or silica base material.

The large surface area of porous films renders FTIR sufficiently sensitive to characterize adsorption of, e.g., moisture, which can occur during any exposure to air in the processing. This is especially important because H_2O (around 3600 cm^{-1}) is a polar molecule and is detrimental to both the real and imaginary part of the k value.

Figure 17 adsorption spectra of HSQ films are shown after several treatments. The pristine (initial) spectrum is compared to spectra of the same film after H_2 plasma treatment. Loss of Si-H hydrophobic groups and the simultaneously emergence of a peak in the $3200\text{--}3700\text{ cm}^{-1}$ region are observed. This broad peak is a result of moisture adsorption and is due to the vibration of silanol groups (Si-OH) and H_2O molecules. The details of plasma interaction will be discussed in a later section.

2. Energy filtered transmission electron spectroscopy (EFTEM)

During the last decades, conventional transmission electron microscopy has evolved into a standard analytical tool for material research. With high resolution TEM (HRTEM) spatial resolution at the atomic level has been reached. This resolution is needed as the low- k dielectrics are to be used in the very narrow dimensions, which are outlined by the ITRS technology roadmap. EFTEM complements this by providing element sensitive analysis of materials in the narrow features.

The combination of elastic and inelastic electron scattering data facilitates the characterization of materials in different areas. EELS probes the electronic excitations from the primary inelastic scattering signal in TEM. The spectrum provides information about the elemental composition, chemical bonding, band structure, atomic specific radial distribution of near neighbors, sample thickness, valence, and conduction electron density.^{70,71} In EELS the characteristic threshold edge at high energy loss ($>50\text{ eV}$) is caused by the

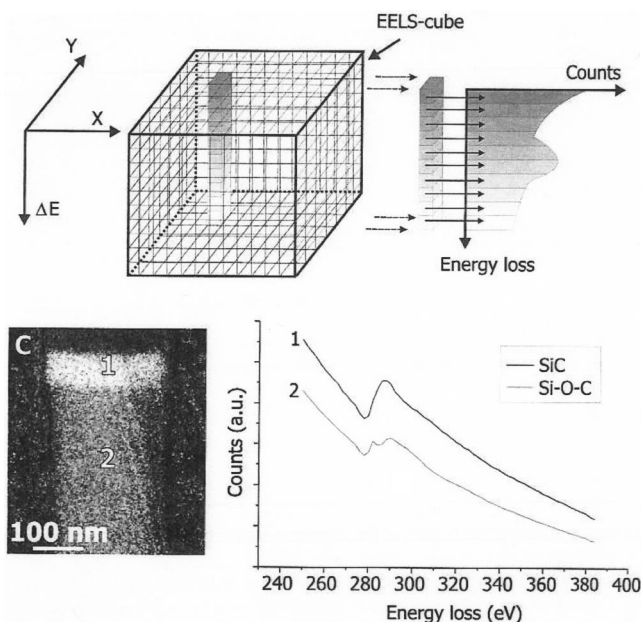


FIG. 18. Schematic representation of the acquisition and calculation of an energy filtered series of EELS spectra by recording the EELS cube. Two carbon spectra are extracted from the EELS cube to visualize the difference in the characteristic energy loss edge (see Ref. 72).

interaction of fast electrons with the deep bound core electrons of the material. The onset corresponds to the ionization energy of core electrons. As the binding energies of core electrons are a function of the atomic number, the position of the edges allows elemental identification. EFTEM is based on the acquisition of elemental distribution maps formed from electrons with an energy corresponding to the energy loss edge in the EELS spectrum.⁷²

Spatial and spectroscopic information can be retrieved by acquiring an energy filtered series and reconstructing a three dimensional EELS cube. This EELS cube is schematically shown in Fig. 18 and contains both the spatial information (X - Y planes) and the spectroscopic information (X - E and Y - E planes). The EELS cube can be reconstructed by taking a large set of energy filtered images (between 50 and 100) with an energy slit width between 1 and 5 eV. In Fig. 18, an example is shown for a low- k material of the silicate type with a SiC hard mask.⁷³ To reconstruct this EELS cube, 75 images with 2 eV slit width starting at 250 eV energy loss were recorded. A carbon distribution map is obtained from the carbon K -edge at 284 eV. Two different C areas can be distinguished relating to the silicate and the SiC hard mask. Clear differences in spectra are obtained by calculating the energy loss spectra from the EELS cube.

3. Nuclear magnetic resonance (NMR)

NMR allows us to characterize the structure of low- k dielectrics. It provides detailed structural information via the isotropic chemical shift interactions.⁷⁴ For low- k dielectrics ^1H , ^{13}C , and ^{29}Si are the primary active nuclei. The chemical shift of ^{29}Si is highly dependent on the presence of surrounding O atoms,⁷⁵ since O is highly electronegative and therefore tends to decrease the electron density around the Si

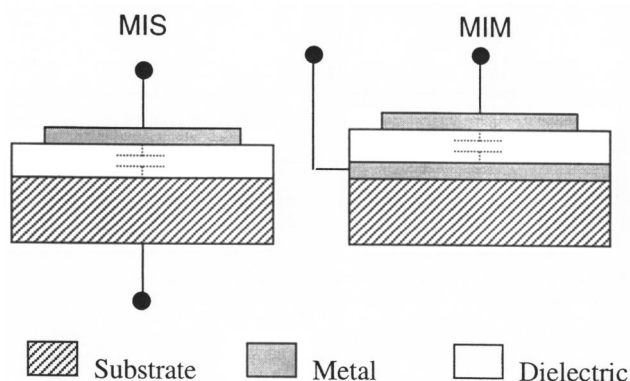


FIG. 19. Planar capacitor for k -value extraction in metal/insulator/Si and metal/insulator/metal configuration.

atom. In this way NMR gives information not only on the composition but also on the polarity of the bonds. ^{29}Si NMR can elucidate the diversity of chemical structures present, from the main M , D , T , and Q peaks⁶³ (see Sec. III) to their hydrogenated M^H , D^H , T^H , and hydrolyzed M^{OH} , D^{OH} , and T^{OH} counterparts. In the latter two the $\text{Si}-\text{CH}_3$ bonds are replaced by $\text{Si}-\text{H}$ and $\text{Si}-\text{OH}$, respectively.

B. Electrical characterization

The electrical performance of the low- k materials either in thin film or structured in narrow features is the key issue. Electrical evaluation of materials is therefore very important. Exposure to ambient and to process environments can have a large influence on the materials and on its electrical properties.

1. Area capacitance

The most basic electrical measurement of the dielectric constant is obtained by an area capacitor which consists of either a metal/dielectric/metal (MIM) or a metal/dielectric/Si (MIS) sandwich (Fig. 19). In the latter case it is important to ensure that the Si substrate is in accumulation. The dielectric constant can be obtained directly through the defining equation [Eq. (3)]. This is a valid assumption only if the fringing capacitance is negligible. For square capacitors with a top plate area $>1 \text{ mm}^2$ the error due to fringing is about 0.2%. Since water adsorption by porous dielectrics occurs readily upon exposure to air, the capacitor has to be sealed carefully by a passivation layer during process or moisture can be desorbed before/during the electrical measurement.

Mercury probe measurements have been used as a quick method to obtain a MIS type capacitor without the need for metal patterning. The interaction of the probe with porous dielectrics is unclear and the results obtained by the technique are subject to discussion. Area capacitance measurements also provide information about the breakdown properties and leakage currents.

2. Interline capacitance

The interline structure is described in a simplified cross section in Fig. 20, where two typical configurations are presented as two parallel lines or a meander fork structure em-

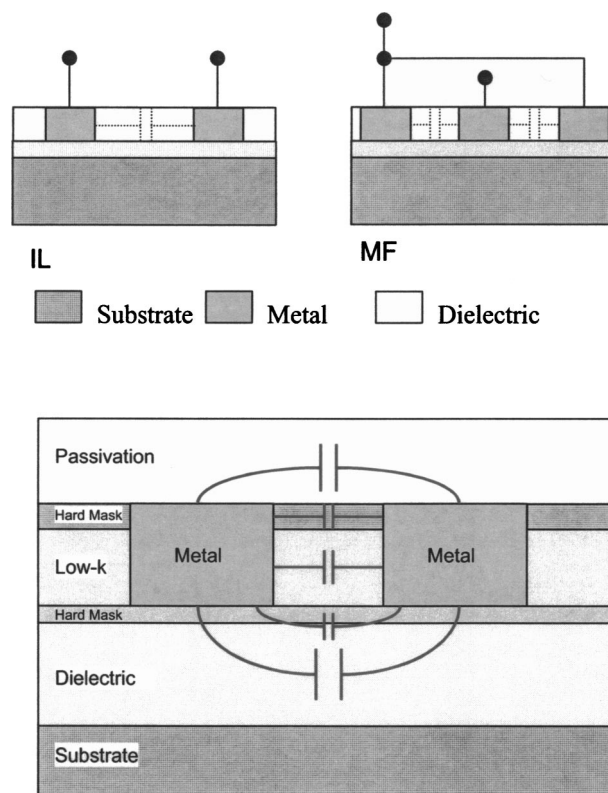


FIG. 20. Schematic layout of interline capacitors either by two parallel lines or by meander/fork structure. In the bottom drawing the presence of fringing capacitors is indicated for a more complete structure.

bedded in a dielectric layer. The lines are insulated from the substrate (or from a metal plane on top of the substrate) by a bottom dielectric layer. For an extensive discussion we refer to Stucchi and Maex.⁷⁶

The interline capacitors are more realistic structures as compared to the area capacitors, because they represent the capacitance between interconnect lines resulting from technology constraints (minimum dimensions, type of dielectric layers, process conditions). As with the area capacitors, interline structures may also suffer from moisture when not sealed properly.

The fringing effect for an interline capacitor can account for more than 50% of the measured capacitance due to the high perimeter/area ratio. Therefore, in order to extract k from these structures we are forced to use a static simulation on a two-dimensional (2D) model with RAPHAEL software.⁷⁷ The model has to include all the dimensions and layers involved in the interline structure definition. For an accurate k -value extraction it is critical to measure the actual dimensions of the dielectric spacing from cross-sectional images and relate these to the electrical measurement for the same structure. The methodology is based on a statistical analysis tool and is graphically represented in Fig. 21.

The interline k -value extraction shows statistical variation as a consequence of the limited technological process control, related to both patterning (litho and dry etch) and planarization chemical mechanical polishing (CMP). An estimate of the inaccuracy in k value due to these variations is indicated in Fig. 22.

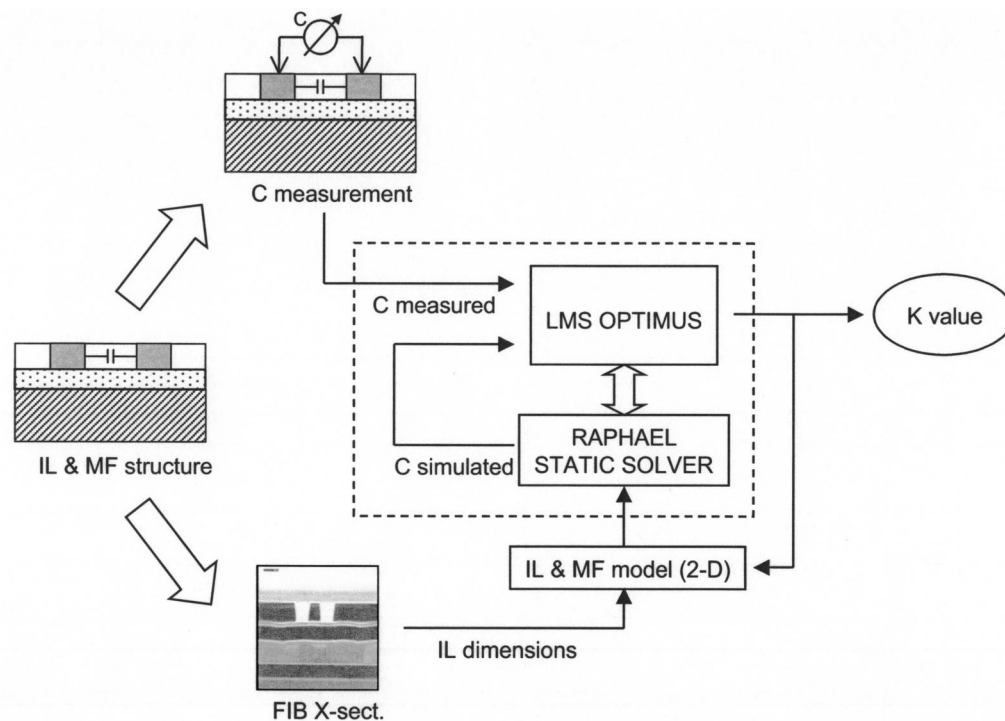


FIG. 21. k value extraction methodology from interline capacitance structures based on physical and electrical measurement and software simulation.

C. Pore structure

Some of the most important features of the low- k dielectrics are related to the pore structure. Methods for characterizing the pore structure are generally based on three different physical principles. The first class of methods is based on a *stereological analysis*, using various types of microscopes, providing a direct observation of the cross section of the solid. These methods are scanning electron microscopy (SEM), transmission electron microscope (TEM), HRTEM, AFM, and scanning tunneling microscopy (STM) or scanning tunneling electron microscopy. Image analysis of the

micrographs can give quantitative information, but in most of the cases the sensitivity is insufficient for porous films developed for microelectronic application.

Nonintrusive methods are based on radiation scattering, wave propagation, positron lifetime spectroscopy, etc. They are generally sensitive to both open and closed pore structures.

Intrusive methods are based on gas adsorption, mercury porosimetry, and calorimetric methods. In the mercury porosimetry, a nonwetting liquid (mercury), is forced into the pores of a dry sample and the pore radius is calculated by the modified Laplace equation. In the calorimetric methods the enthalpy change is measured when a dry sample is immersed into a liquid.^{10,78,79}

In this review we limit ourselves to those techniques that are applicable to thin films such as positron annihilation lifetime spectroscopy (PALS) or positron annihilation spectroscopy (PAS),^{80,81} small-angle neutron scattering (SANS) and small angle x-ray scattering (SAXS) combined with specular x-ray reflectivity (XRR),^{82,83} and ellipsometric porosimetry (EP).^{84–87} The values of interest are pore size and structure as well as total porosity. Although the above techniques are based on different physico-chemical principles, it will be discussed how well the results of the measurements agree.^{88,24}

1. Positron annihilation lifetime spectroscopy (PALS,PAS)

Both in PALS and PAS, films are irradiated with a focused beam of several keV positrons. Positrons have a limited lifetime and can, by interaction with an electron, either annihilate or form a positronium (Ps)—the electron-positron bound state. PALS measures the lifetime of positronium,

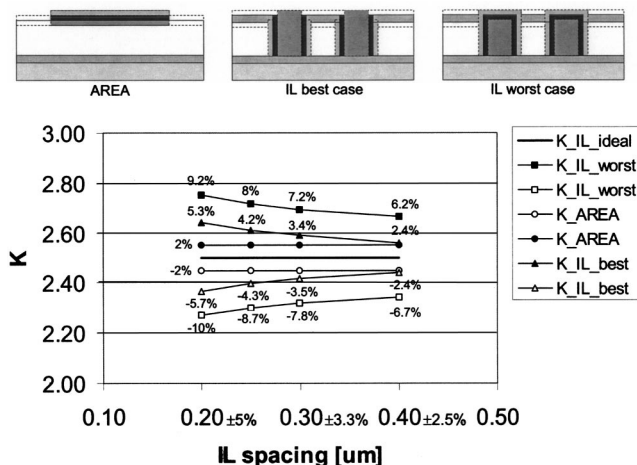


FIG. 22. Comparison between the accuracy of the k -value extraction in planar capacitors and interline capacitors. For the interline capacitor best case, a variation of 10% was taken into account for the vertical dimensions and for the worst case a similar variation in the lateral dimension.

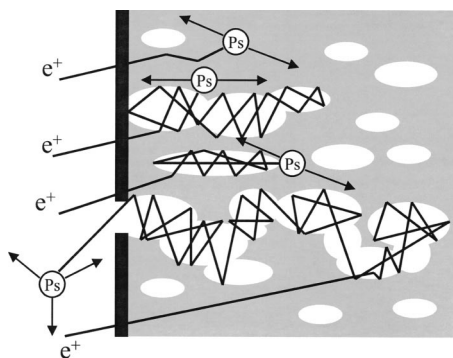


FIG. 23. Formation and diffusion of positronium (Ps) in a porous material containing both open and closed pores. More detailed description and analysis of positronium behavior in the materials with open and close pores and with capping layers can be found in papers of Gidley and Sun (Refs. 89 and 90).

whereas PAS extracts information from the Ps annihilation reaction. As will become clear, the former provides information on pore size and pore structure, whereas the latter on total porosity.

Ps can exist in two different spin states (ortho- and para-). Ortho-positronium (*o*-Ps) is more stable and localizes in the void volume where the *o*-Ps binding energy is not reduced by the dielectric constant of the surrounding material. With an initial kinetic energy of a few eV it will begin to diffuse and thermalize. Its natural lifetime of 142 ns (in vacuum) is reduced by annihilation with molecular electrons in the pore walls with an opposite spin, yielding information about pore sizes and geometry. However, if all pores are open and interconnected, Ps can escape to vacuum, existing for its natural lifetime, and information related to pore size cannot be obtained. In this case one needs to deposit a capping layer to measure the pore size (Fig. 23).^{89,90}

In order to get information on the pore size Ps lifetime histograms are recorded, and the lifetime distribution curves are obtained with a fitting program developed for this purpose (Fig. 24). The distribution curves can then be transformed into pore size data when the pore geometry is

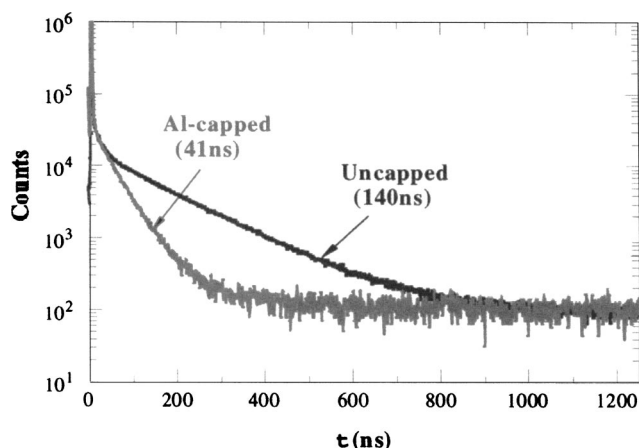


FIG. 24. PALS spectra of uncapped and Al capped porous silica film. Reduction of Ps lifetime allows calculate pore size using a special calibration procedure and using an appropriate pore geometry (reprinted with permission) (see Ref. 90).

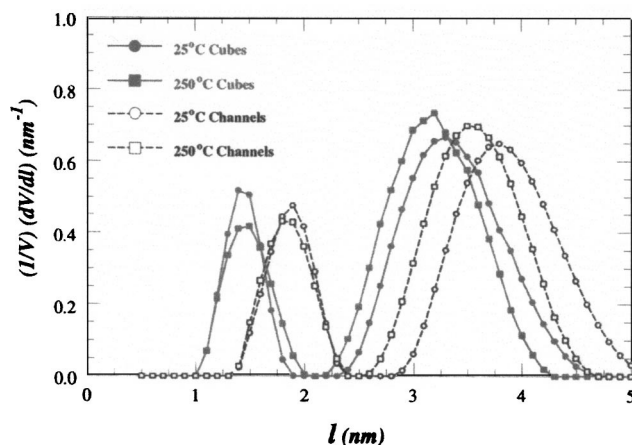


FIG. 25. The specific void-volume distribution in MSQ based low-*k* film obtained using the corresponding lifetime calibration and different pore models (cubes and channels) and different sample temperatures (reprinted with permission) (see Ref. 89).

known.⁸⁰ For this calculation it is necessary to perform calibration. For very large pores (mean free path on the order of 100 nm) the calibration is performed using high porosity (90%–98%) silica powders. In the sub-nm regime, the quantum mechanical Tao–Eldrup model has been empirically used to calibrate Ps lifetime of several nanoseconds with pore size.⁸⁰ The quantum mechanical model has been extended to the classical large-pore limit and results of the analysis show good agreement with other techniques.

Depending on the annihilation reaction in PAS 2γ or 3γ photons are generated. The film porosity can be calculated from a comparison of the measured 2γ and 3γ photon annihilation ratio of Ps atoms (3γ PAS).³⁴ This is based on the fact that self-annihilation of *o*-Ps requires at least 3γ photons to convert total momentum (which is related to 142 ns in vacuum) while an annihilation with a molecular electron from the pore wall (“pickoff” annihilation) results in the emission of 2γ photons. The probability of the latter depends on the collision frequency with pore walls which affects the *o*-Ps lifetime. The rate of “pickoff” annihilation influences the ratio of the 2γ and 3γ annihilation intensity and can therefore be used to derive porosity properties. A more detailed description of this procedure can be found in the aforementioned article.³⁴

PAS and PALS are also efficient for the evaluation of bi-modal pore size distributions: they give information related to their size and relative concentration (Fig. 25).⁸⁰ They also allow to analyze depth profile of the pore structure.

2. Scattering techniques (SANS, SAXS)

Small angle radiation scattering arises from variations in the scattering length density occurring over distances exceeding the interatomic spacing in solids. Such variations occur when a solid material contains pores and details of the porosity can be obtained from measurements of the angular distribution of scattered intensity. A schematic setup of the experiment is shown in Fig. 26 for both SAXS and SANS. The scattered intensity is measured as a function of angle, 2θ , to the incident direction. The pore size is given as d

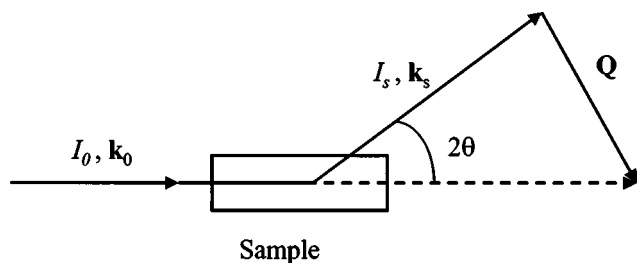


FIG. 26. Schematic representation of the incident and scattered beams in a small angle scattering experiment (see Ref. 83).

$\sim \lambda/2\theta$ where λ is the wavelength of the scattered radiation (0.1–0.4 nm for x rays and 0.1–2.5 nm for neutrons).⁷⁹

Scattering techniques are normally used in combination with specular XRR that allows the measurement of the film density, i.e., total porosity (see Fig. 27). The latter is calculated by normalization of the XRR film density to the skeleton density. This necessitates the assumption that the skeleton is identical to the dense, nonporous prototype. Sometimes such an assumption is not justified.⁸² The nonporous prototype may also not be available as is the case for CVD SiOCH films. When the angular distribution of scattered intensity is available, the pore size distribution can be obtained using a variety of fitting models.

In SANS, at e.g., the NIST Center for Neutron Research,⁸² the absolute scattered neutron intensity I is plotted against the scattering vector $q = (4\pi/\lambda)\sin(\theta/2)$, where θ is the scattering angle of the incident beam and λ is the neutron wavelength (0.6 nm). The SANS intensity plotted versus q is a function of the porosity and wall density. The functional form is determined using the Debye random two-phase (void+solid) model. The film thickness and overall electron density are evaluated by XRR measurements and are combined with film compositional data from RBS and ERD in order to determine the overall film density. Since the film density is also a function of the porosity and skeleton density, these values are obtained by solving for the unknowns in the equations from SANS and XRR.⁸²

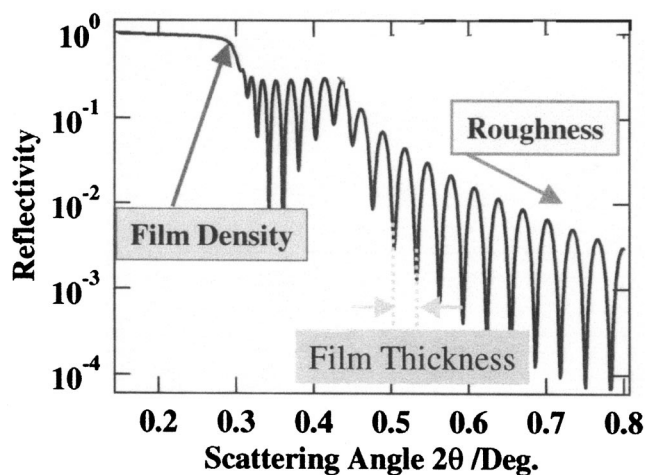


FIG. 27. Determination of the film density and thickness from x-ray reflectivity.

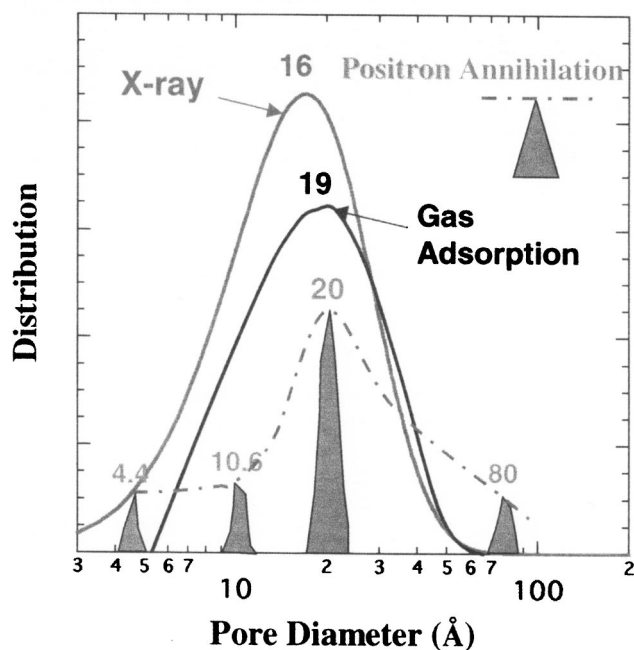


FIG. 28. Pore size distribution measured by x-ray scattering, nitrogen porosimetry, and PALS (see Ref. 83).

Recently, a simple x-ray scattering method (SAXS) for thin film evaluation was reported.⁸³ The pore size is calculated by comparing the observed profile of scattering intensity with results of simulation. This is a convenient approach for getting general information as only the mean pore size can be calculated (Fig. 28). Four different peaks were resolved by PALS. Unfortunately, the authors did not provide any information about the film. They make clear, however, that if the film has a bi-modal pore distribution, the effective pore size depends on the ratio between small and large pores. Generally, SAXS is not able to distinguish between pores and particles.

The small volume of low- k films as compared to bulk materials reduces the sensitivity and resolution of the scattering techniques. Wu *et al.* used the Debye formalism and additional information obtained by XRR, RBS, and ERD (density and film composition) to analyze SANS data and to determine additional film characteristics such as porosity, wall density, etc.⁸² The pore connectivity was analyzed by comparing the neutron scattering in the films with empty pores and pores filled by deuterated toluene.⁸² The films are stacked together (with up to eight films) in order to enhance the scattering signal. These efforts allowed the extraction of more extensive information.

3. Adsorption techniques (BJH, EP)

Gas adsorption porosimetry. Adsorption porosimetry is one of the most important and widely used method for the characterization of a variety of porous solids. The traditional nitrogen porosimetry uses direct weighing by special microbalance techniques but is almost not applicable for the evaluation of thin porous films. We will highlight its general features and fundamentals because they also apply to EP,

which has been developed for thin film applications and will be discussed in the next section.

Different approaches are used for the calculation of the pore size distribution in mesoporous and microporous films. The calculation of pore size in mesoporous films relies on the phenomenon of progressive emptying of a porous system, initially filled to equilibrium pressure, $P = P_0$. The calculations are based on analysis of a hysteresis loop that appears as a result of the difference in effective radius of curvature of a condensed liquid meniscus during adsorption and desorption.⁹¹ The adsorptive vapor condenses in the pores at a vapor pressure P below the equilibrium pressure of a flat liquid surface P_0 . The dependence of the relative pressure P/P_0 on the meniscus curvature is described by the Kelvin equation

$$\ln\left(\frac{P}{P_0}\right) = -\frac{f\gamma V_L}{r_K \cdot RT}, \quad (22)$$

where γ and V_L are surface tension and molar volume of the liquid adsorptive, respectively. f equals unity for slit-shaped pores and $f=2$ for cylindrical pores. The Kelvin radius, r_K , is calculated from the measurement of P/P_0 . The pore radius, r_p , is related to the Kelvin radius as $r_p = r_K + t$ and t is the thickness of the layer adsorbed on the pore walls. Values of t are obtained from the adsorption of the same adsorbate on a nonporous sample and are defined by the Brunauer, Emmet, Teller (BET) equation⁹¹

$$t = \frac{d_0 C \cdot K \cdot (P/P_0)}{[1 - K(P/P_0)] \cdot [1 + K(C-1)(P/P_0)]},$$

where C is the BET constant, and K is a coefficient satisfying the requirement that at $P = P_0$ $t \leq 5-6$ monolayers.

The BET equation is also used for measurements of specific surface area. The volume of adsorbate necessary for filling the first monolayer is measured and the surface area is calculated from the surface area occupied by each adsorbate molecule. In some cases calculation of cumulative surface area is more convenient. In this case the specific surface area of each small group of pores δA_i is calculated from the pore volume and pore radius as $\delta A_i = \delta V_i / r_i$. By summing the values of δA_i over the whole pore system the cumulative surface area is obtained.^{92,93}

In micropores of the order of a few molecular diameters, the Kelvin equation is no longer valid. Not only do the values of the surface tension and the molar volume deviate from those of the bulk liquid adsorptive, but also the concept of a meniscus becomes meaningless. Different methods have been developed to address this issue. The simplest method to determine the microporous volume is the t method of de Boer and its extension.⁹¹ Thermodynamic methods (Dubinin and Radushkevitch,⁹⁴ Horvath and Kawazoe,⁹⁵ Saito and Foley,⁹⁶ etc.) based on the change of the adsorption potential in micropores are presently used.

A theory developed by Dubinin and Radushkevitch (DR)⁹⁴ uses change in adsorption potential when the pore diameter is comparable with the size of the adsorbate molecules. The process involved is micropore volume filling rather than layer-by-layer adsorption on the pore walls. The adsorption potential \mathbf{A} and the characteristic adsorption en-

ergy \mathbf{E}_0 are a function of the micropore size and the amount of adsorption \mathbf{W} at the relative pressure \mathbf{P}/\mathbf{P}_0 is given by

$$W = W_0 \exp[-(A/E)^n], \quad (23)$$

$$[n=2; E = \beta E_0; A = RT \ln(P_0/P)],$$

where W_0 is the micropore volume and β is the affinity coefficient. A linear plot of $\ln(W)$ versus A^2 gives W_0 and βE_0 . The value of βE_0 provides the isosteric heat of adsorption. E_0 gives the average pore size $w_0 = K/E_0$ where $K \approx 12$ is a coefficient slightly changing with E_0 .^{91,97} The DR analysis provides important parameters of the micropore structure such as micropore volume, average pore size, and isosteric heat of adsorption.

Traditional N_2 adsorption porosimetry [Barrett-Joyner-Halenda (BJH)] is based on the measurement of mass or volume of adsorbate condensed in the pores. Therefore, only information related to open pores can be obtained. If the material swells during the adsorption, the measured adsorptive volume corresponds to the swelled film and is larger than the real concentration of open pores.

This method clearly has limitations for the evaluation of thin films. In case of a small amount of porous substance the microbalance technique is not sufficiently sensitive to detect the adsorbate mass. Films from several substrates need to be scrubbed off to have enough material and prepare a powder like sample. Another limitation is related to the low operating temperature of nitrogen porosimetry. Significant stress in the film can be generated during cooling and cracking can occur.

Several papers on the measurement of the pore size distribution by adsorption porosimetry in thin films have been published. In these articles the good enough sensitivity was realized by using quartz crystal microbalance (QCM),⁴⁴ surface acoustic wave (SAW) sensor,⁹⁸ XRR,⁹⁹ and ellipsometry. First two methods need deposition of the porous film on top of a special sensor. From this point of view, methods based on x-ray reflectivity and ellipsometry are more attractive because they allow nondestructive evaluation of porous films deposited on top of any smooth substrate. XRR measurements allow detect change of the adsorbent mass that makes it similar to traditional microbalance technique. Ellipsometric porosimetry has several special features making this method more informative. For this reason we are going to analyze this method in more detail.

Ellipsometric porosimetry (EP). Ellipsometric porosimetry is a combination of a nonintrusive (wave propagation) and intrusive (adsorption) methods.^{84,85} Ellipsometry is based on modeling changes in the measured polarization state of a light beam reflected off a surface. The measured parameters are the phase and amplitude ellipsometric angles Δ and Ψ , defined by the fundamental equation of ellipsometry

$$R_{\parallel}/R_{\perp} = \tan(\Psi) \exp(i\Delta) \quad (24)$$

where R_{\parallel} and R_{\perp} are Fresnel reflection coefficients for the light polarized parallel and perpendicular to the plane of incidence. The reflection coefficients are determined by the optical characteristics and composition of the substrate and

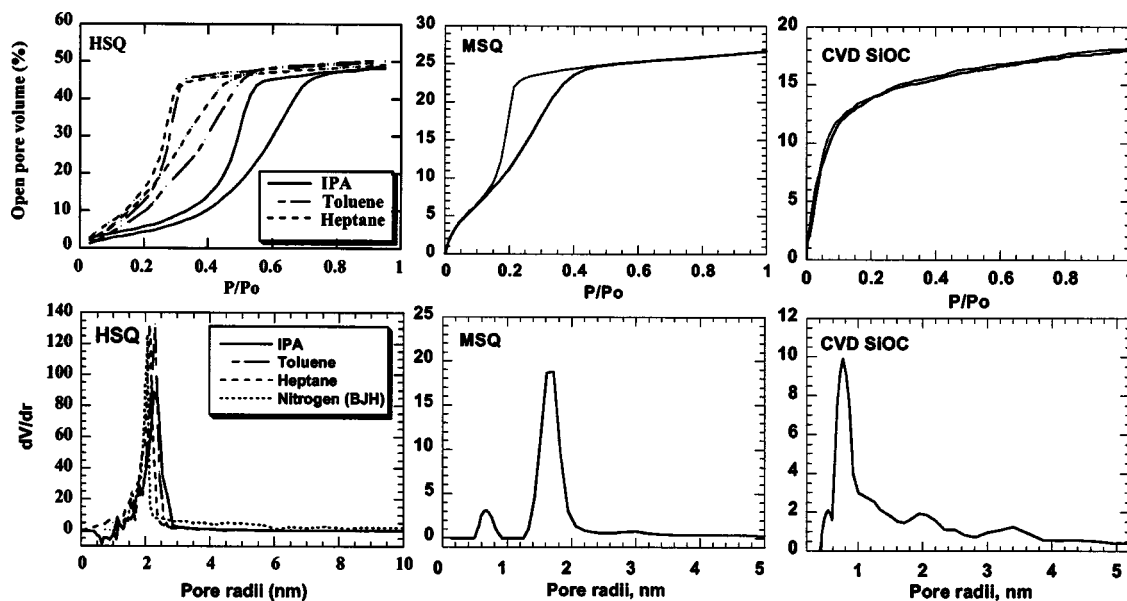


FIG. 29. Ellipsometric porosimetry data for typical low- k films (a) mesoporous HSQ based material. This graph demonstrates good agreement of pore size calculated with different adsorptives and nitrogen (BJH) porosimetry, (b) MSQ based film with bi-modal porosity and (c) a carbon doped microporous silica film. In the last two cases adsorptive is toluene.

overlayers, their thickness and morphology. The ellipsometric parameters Δ and Ψ can be measured either at a constant wavelength or as function of photon energy. The single wavelength ellipsometry is often used for fast, nondestructive, in-line monitoring of the film thickness and refractive index. However, it has limitations if the film is thin (<10 nm) or the film thickness is close to the ellipsometric period. [In the case of a transparent dielectric film with refractive index n , the ellipsometric period is equal to $d_0 = \lambda/2\sqrt{n^2 - \sin^2 \varphi}$, where λ and φ are wavelength and incidence angle, respectively. d_0 can be changed by wavelength variation. For this reason spectroscopic ellipsometry is more suitable for independent determination of the film thickness and refractive index.] Spectroscopic ellipsometry (SE) is more informative because it provides a more reliable independent determination of the film thickness and refractive index. The basic idea is to measure changes in optical characteristics of a porous film when the pores are filled by a liquid adsorbate with known refractive index.

First we will discuss the measurement of the full porosity. The relation between the optical characteristics and properties of the porous film is described by the Lorentz–Lorenz equation

$$B_p = \sum N_i \alpha_i = \frac{3}{4\pi} \left[V \cdot \frac{(n_1^2 - 1)}{(n_1^2 + 2)} + (1 - V) \cdot \frac{(n_s^2 - 1)}{(n_s^2 + 2)} \right], \quad (25)$$

where

$$V = 1 - \frac{B_p}{B_s} = 1 - \left[\frac{n_p^2 - 1}{n_p^2 + 2} \right] \bigg/ \left[\frac{n_s^2 - 1}{n_s^2 + 2} \right] \quad (26)$$

and B_p is the effective polarizability of a unit volume of the porous film, N_i and α_i are the number of molecules and the molecular polarizability volume¹⁰⁰ of the material compo-

nents; n_p is the measured refractive index of the porous film; and n_s and n_1 are the refractive index of the film skeleton and of the material inside pores, respectively. V is the relative pore volume (porosity). If the pores are empty $n_1 = 1$, then the relative film porosity is given by Eq. (26).⁸⁵

Equations (25) and (26) are also valid if a liquid with a known refractive index n_{liq} fills the pores ($n_1 = n_{liq}$). The amount of adsorbate inside the pores is calculated using the refractive index and density of the liquid adsorptive. Ellipsometry yields information on both the refractive index and the film thickness d . Therefore, the adsorbate volume, which is equal to the open pore volume, can be calculated. The relative volume of open and closed pores is calculated from a comparison of the results obtained with empty and filled pores (before and after adsorption). This analysis gives information on pore connectivity because only open pores are filled during the adsorption. If the porous film is anisotropic, the depth profile can be analyzed using a multilayer optical model.⁸⁷ The pore size distribution is measured by using the Kelvin equation (if pores have a diameter larger than 2 nm) and extended by the Dubinin–Radushkevitch theory for micropores.

Figure 29(a) shows EP data for a typical mesoporous HSQ film. The adsorption/desorption isotherms produce a well-pronounced hysteresis loop. The saturation points for the different adsorbates are very close to one another and correspond to an open porosity of 48%. Comparison of this value with the total porosity measured by spectroscopic ellipsometry leads to the conclusion that all pores in this film are interconnected. This graph also demonstrates that the choice of an appropriate adsorbate can shift the isotherm to a different P/P_0 range because of different molecular characteristics. According to Gurvitch's rule, if adsorptives with different molecular characteristics give the same pore size, the Kelvin equation is still valid.^{91,92} A perfect agreement of

TABLE II. Comparative data for several porous MSQ and HSQ films, characterized with EP, BJH, and SANS methods. Full porosity and average pore size are given. M1, M2, M3, and M4 are based on the same MSQ1, M5, and M6 is a porous HSQ and M7 is MSQ2 based.

Sample	K	Thickness (nm)		Porosity (%)		Characteristic pore size (Å)			
		EP	XRR	EP	SANS/XRR	EP	BJH	SANS	PALS
M1	1.8	265±1	265±1	53±4	37±7	84±2	70	62±8	82±9
M2	2.0	418±1	424±1	45±2	33±6	90±3	92	61±6	73±5
M3	2.2	427±1	424±1	39±4	26±5	57±2	63	50±4	57±2
M4	2.5	410±1	427±1	26±4	20±7	31±4	33	27±3	39±2
M5	2.0	615	—	52	—	42	40	22	42
M6	2.5	710	—	21	—	28	—	—	27
M7	—	420	—	34	—	20	—	—	20

the pore size distribution calculated from the adsorption of different adsorbates is obtained. The data are also in good agreement with those obtained by standard N_2 adsorption (BJH) porosimetry.⁸⁸

Figure 29(b) shows the adsorption/desorption isotherm and pore size distribution obtained for a MSQ based film. This film shows a bi-modal porosity (both meso- and micropores are present in the film). The micropores appear to be an intrinsic property of the MSQ based material (constitutive porosity) and are related to the replacement of hydrogen by the larger methyl group. Adsorption in micropores is responsible for the additional slope in the isotherm in the low-pressure region ($P/P_0 < 0.1$).

Figure 29(c) shows EP results for a C doped silica film. C doped silica films are typically microporous and the DR method is used for pore size calculation.

4. Comparative study

The instrumental methods employed in this study are based on different physico-chemical principles. The pore sizes are not directly acquired from the measurements. In order to determine the pore size and porosity, it is necessary to transform the raw data by assuming an appropriate model that takes into account pore structure and pore-probe interaction. That is, the results can be highly model dependent. Table II summarizes the properties of some porous HSQ and MSQ films measured by different methods.⁸⁸ Wafers M1–M4 are the same MSQ based low- K film prepared with different porosity, wafers M5 and M6 are HSQ material with two different porosities and wafer M7 is another MSQ based film. Two techniques are adsorption porosimetry (EP and nitrogen BJH porosimetry) and the others are radiation beam-based (SANS/XRR and PALS). Bulk specimens are used only for BJH porosimetry—i.e., it is a destructive method. Nitrogen porosimetry was used as a standard technique for porosity characterization (Quantachrome Autosorb-6 sorption analyzer). The average pore diameters obtained from the BJH method show good agreement with the EP data, including the inversion of pore diameters of M1 and M3. Cumulative pore volumes are 0.98, 0.88, 0.70, and 0.35 (ml/g) for M1, M2, M3, and M4, respectively, and show consistent agreement with the EP data and the change of dielectric constant. The N_2 adsorption porosimetry is not capable of detecting inaccessible (closed) pores because the adsorptive vapor has no access to closed pores. A unique feature of EP is

that the number of closed pores can be calculated using a multiangular or SE measurement and assuming a dielectric model where the film consists of solid part+open porosity filled with adsorptive+closed pores. It is found that the pore connectivity, the ratio of open porosity to total porosity, increases from 86% (M4) to 97% (M1), as k decreases. The full porosity is determined to consistently increase as dielectric constant decreases.

The PALS results were deduced using an infinitely long channel pore model, where the pore size is the side length corresponding to a tubular pore diameter. The pore size increases with decreasing k and the values are similar to those obtained by BJH and EP. In all these films the pores are nominally found to be fully interconnected. A more significant difference is observed between the three above techniques (BJH, EP, and PALS) and SANS.

Whereas SANS reflects spatial density of scattering bodies, either voids or particles, PALS is directly related to the volume of void elements and adsorption porosimetry reflects pore surface geometry. SANS measurements provide systematically lower porosity and smaller pore sizes than the other methods. Besides the above points, it can be safely said that successful agreement is obtained.

Another example of comparative analysis of different instrumentation is evaluation of critical characteristics of MSQ based low- K films by XRR, EP, and SAWS.¹⁰¹ Figure 30(a) plots EP porosity and SAWS density as a function of porogen concentration. A strong linear dependence is clear. Comparing the SAWS density to the XRR density [Fig. 30(b)] yields a linear fit with an almost ideal slope of 1.0. These techniques clearly provide reliable density values with remarkably strong correlation among porogen concentration, porosity, and density. The skeletal density calculated from EP porosity and SAWS/XRR density was equal to ~ 1.4 g/cm³, typical for bulk MSQ.

5. Limitations of the methods for evaluation of thin film low- k dielectrics

Experimental results presented in the previous section were obtained under strictly controlled conditions. The porous films used for the analysis were chosen from the same lot of wafers. Any differences appearing during the analysis were carefully analyzed and discussed. It is important to understand specific features of these methods to be able to extract information most valuable for technology.

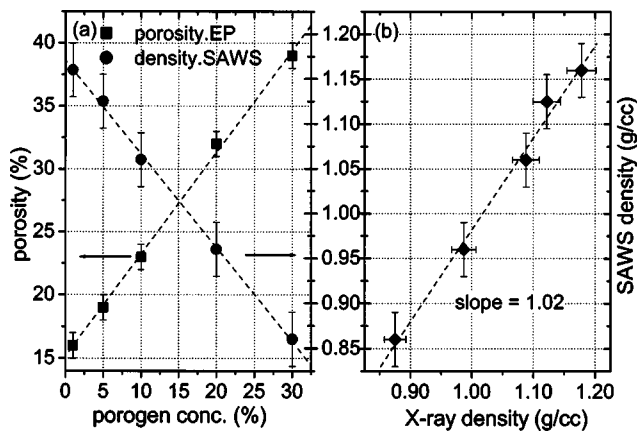


FIG. 30. (a) Linear dependence of EP porosity and SAWS density on Porogen concentration. (b) Correlation of SAWS density vs XRR measured density. The results are obtained for a MSQ based film with macromolecular porogen (see Ref. 101).

Table III shows a comparative characterization of different non-destructive techniques. This table includes radiation scattering techniques (SANS, SAXS) that are normally used in combination with XRR, positron annihilation methods (PALS, PAS), and EP. An important method is SAW spectroscopy (SAWS) allowing nondestructive evaluation of density and mechanical properties of low- k films (as discussed in the next section). SE gives information related to the film thickness and uniformity, refractive index and porosity of the films. Below is a brief analysis of problems and limitations of each method that can appear during the analysis of porous films.

(i) EP requires knowledge of the refractive index of the dense prototype in order to calculate the full porosity. This value is available for most low- k films or can be estimated if the chemical composition is known. If the porous film is completely unknown, EP may have problems with the calculation of full porosity, and consequently with the calculation

of film density and pore connectivity. EP is not capable of measuring the size of closed pores.

(ii) Both PALS and PAS are generally able to estimate the film porosity by comparing Ps annihilation inside the pores and in vacuum. All positron annihilation states contribute to a PALS spectrum. If the intensity of a given component is known, one can conclude that the fraction of the long o -Ps lifetime is equal to the porosity fraction. However, Ps annihilates after a limited number of collisions with pore walls. Therefore, if the low- k film contains pores with long and narrow “bottlenecks,” the Ps movement through these necks is limited.³⁴ In this case, some Ps are not able to escape to vacuum as the large number of collisions is sufficient for annihilation inside the necks. Therefore, these open pores behave as closed pores. As a result, these methods have a tendency to underestimate the open porosity and the degree of pore connectivity. For instance, PALS showed that Ps does not escape from the pores when the film was prepared with a relatively low porogen concentration,³³ whereas EP showed that toluene filled all pores in the MSQ based films. Swelling can interfere with the analysis of porosity in EP. To solve this problem, it is necessary to analyze change of refractive index and thickness independently.⁹³

(iii) The radiation scattering techniques (SANS and SAXS) are able to derive the mean pore size, but bi- or multimodal pores cannot be distinguished. Generally, these methods need to be combined with XRR measurements to determine the film density and calculate the porosity.

Generally, SAXS is also able to derive the total surface area and porosity in bulk materials. However, this procedure is not well suited for thin films because the total pore volume and surface area are too small.

D. Mechanical characterization

1. Hardness and elastic modulus evaluation

Below we give an overview of four techniques that are used for the determination of the elastic modulus E . Of these, nanoindentation is traditionally the method of choice, but other techniques are gaining interest due to their nondestructive nature and applicability to thinner layers.

Nanoindentation. Nanoindentation utilizes a diamond tip that is pressed into the material of interest, and subsequently retracted, while monitoring the required force P and indent depth h . Hardness is then defined by the ratio of the force and the projected contact area A , which is a known function of the contact depth h_c . However, it should be noted that hardness is not a fundamental property and values will depend on the indenter’s tip geometry. The reduced elastic modulus E_R , used instead of E because the Poisson ratio ν is not always known, is given by

$$\frac{1}{E_R} = \frac{1 - \nu^2}{E} + \frac{1 - \nu_i^2}{E_i}, \quad (27)$$

where ν_i and E_i are the properties of diamond. E_R is normally extracted using the slope of the unloading curve dP/dh (known as the contact stiffness S) from

TABLE III. Comparative characteristics of instrumentation used for the nondestructive characterization of porous low- k films.

Problem	SAXS 1	SANS 2	XRR 3	PALS 4	PAS 5	EP 6	SAWS 7	SE 8
Open pore size	a	a	...	b	a	a
Closed pore size	a	a	...	a	a
Full porosity	...	b	b	b	b	b	b	b
Closed pore volume	...	b	...	b	b	b
Open pore volume	...	b	...	b	a	a
Interconnectivity	...	b	...	a	a	a
Skeleton properties	...	a	a	...	b
Bi-modal pores size	a	a	a
PSD	a	a	a
Barrier evaluation	a	a	a
Film density	a	b	a	b
Film thickness	a	a	...	a
Refractive index	a	...	a
Spec. surface area	...	b	a
Young modulus	b	a	...

^aProven.

^bOption which has been realized but may have problem.

$$E_R = \frac{\sqrt{\pi}}{2\beta} \frac{dP/dh}{\sqrt{A}}, \quad (28)$$

where β is a constant close to unity that depends on the indenter tip geometry ($\beta=1$ for a spherical indenter). A good overview of the application of nanoindentation on endurance of coatings was recently given by Malzbender *et al.*¹⁰²

The main concern in using nanoindentation for the extraction of E_R is related to the spatial extent of the elastic deformation field. This extends well beyond the actual depth of indentation and, for a soft dielectric layer on a hard SiO_2 substrate, can result in an overestimation of the true modulus. The commonly used rule of thumb stating that reliable data can only be obtained from indentation depths below 10% of the layer thickness leads to highly stringent demands on the equipment for dielectric layer thicknesses as thin as 300 nm.

Recent advances in system design have resulted in tools that operate in the μN range. Using dynamic testing reproducible results can be obtained. In this method a small oscillation (nanometer regime) is added to the linear increase of h . The modulus is extracted during each periodic retraction of the tip, resulting in detailed $E_R(h)$ information. However, especially with soft polymers, a great deal of care needs to be taken with regards to tip shape,¹⁰³ relaxation phenomena, and surface contact.¹⁰⁴

Nanoindentation is also applicable for thin dielectric coatings with subtractive porosity. The latter tends to reduce the extent of the deformation field and consequently yields a constant value over a larger depth range. However, there is still a considerable discussion about the true meaning of the data obtained as the influence of pore crushing is not well understood.

Standard monitoring of elastic modulus and hardness can be performed by nanoindentation. For our results a MTS Nanoindenter^{XP} (DCM head) was used, which employs a continuous stiffness measurement (CSM), yielding continuous modulus and hardness data as a function of indent depth. Even though there is some concern about obtaining reliable data for thin films, Fig. 31 shows that the same modulus can be extracted for a 400 nm, 1 μm , and 2 μm film of a C-doped silica glass. The observed increase of modulus with contact depth is due to the influence of the hard SiO_2 substrate, as expected for a thin film, while the true modulus is extracted at low contact depth where this influence is minimal. The same behavior is observed for $H(h_c)$ curves, although the increasing trend is shifted to slightly higher depths due to the smaller spatial extent of the plastic as compared to the elastic deformation field.

It should be noted that a careful surface contact determination¹⁰⁴ should be made for each measurement in order to obtain reliable data. The scalability of the curves, for which the depth scale is normalized to the layer thickness, also indicates that layers with similar material properties are obtained for all thicknesses. Especially for spin-on materials this is not always the case.

As described elsewhere, sealing of low- k materials is attempted (e.g., plasma treatments) and typically leads to a modification of the surface region. Nanoindentation is a

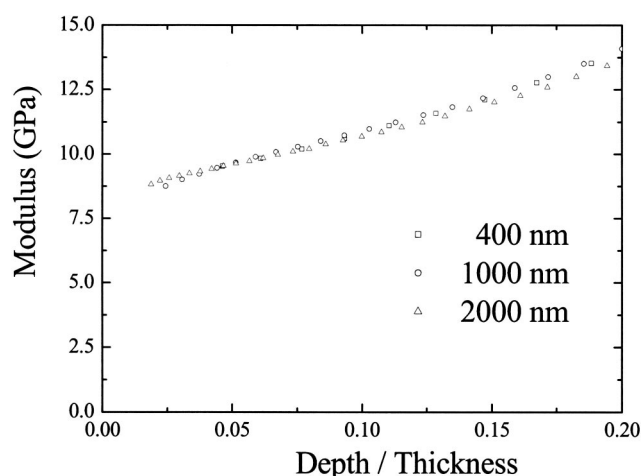


FIG. 31. Nanoindentation data on three C-doped silica films of different thickness as indicated. By using a depth/thickness axis a clear scaling is observed, indicating material properties are the same for the three films and the same value for the elastic modulus can be extracted.

powerful technique for the evaluation and optimization of the extent of modification obtained. Nanoindentation data on three C-doped silica films of different thicknesses is indicated. By using a depth/thickness axis a clear scaling is observed, indicating material properties are the same for the three films and the same value for the elastic modulus can be extracted.

Figure 32 shows an increase in hardness for the surface region of two materials for several different treatments.

Surface acoustic wave spectroscopy (SAWS). SAWS is a nondestructive characterization method. A surface wave, induced by a pulsed laser beam, has a phase velocity v_{ph} that depends on the material density ρ , Poisson ratio ν , and elastic modulus E as

$$v_{ph} = \frac{0.87 + 1.12\nu}{1 + \nu} \cdot \sqrt{\frac{E}{2\rho(1 + \nu)}} \quad (29)$$

for a homogeneous and isotropic material. The amplitude of the wave motion decays exponentially with depth, so its energy is concentrated near the surface. Therefore a thin coating will have a strong impact on the propagation velocity. A detailed description of the influence of the density and elastic properties of both coating and substrate on the wave dynamics is given by Farnell and Adler.¹⁰⁵

The SAW is typically detected at two positions, several millimeters from the source (x_1 and x_2), using a wide-band piezoelectric transducer. From the Fourier transform of the wave form the phase spectra $\phi_1(f)$ and $\phi_2(f)$ can be determined and can be used to calculate the frequency dependent velocity dispersion curve

$$v_{ph}(f) = \frac{(x_2 - x_1)\omega}{\phi_2(f) - \phi_1(f)}, \quad (30)$$

where ω is the angular frequency. The dispersion is a result of the larger penetration depth of the wave for smaller frequencies, and the resulting stronger influence of the substrate properties. A fit of the dispersion curve using all known material properties of both substrate and film then yields the

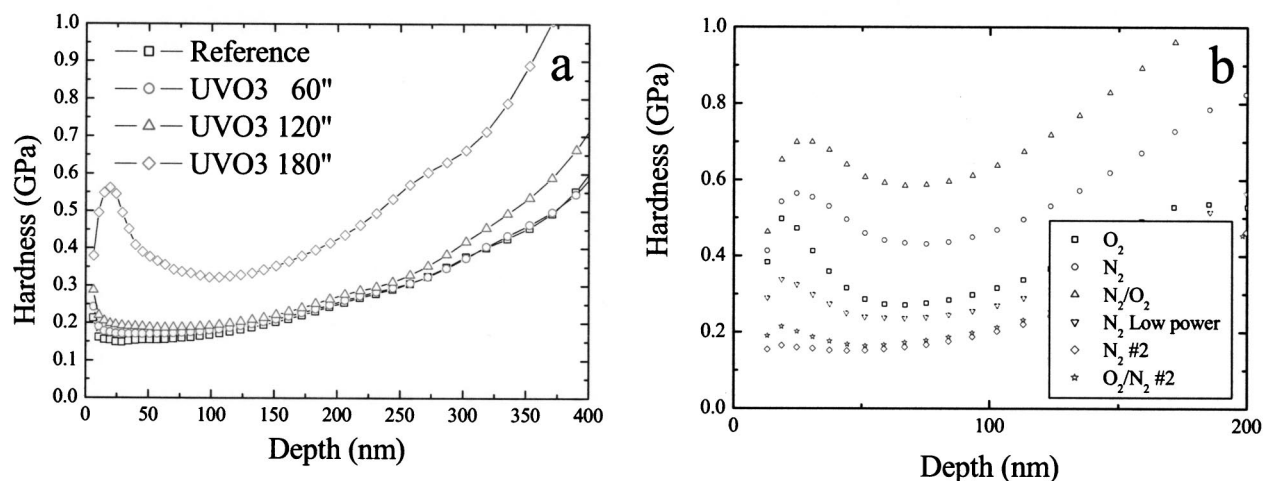


FIG. 32. Surface hardening of a 400 nm silica-based low- k film due to UV treatments for 60, 120, and 180 s (a) and several plasma treatments as indicated.

elastic modulus of the film. Other systems¹⁰⁶ using lasers to both induce the acoustic wave and measure its propagation are also being developed.

Surface Brillouin scattering (SBS). SBS also allows for the measurement of surface wave dispersions. It is based on the inelastic interaction between photons from a laser light source with acoustic phonons of the sample. The small frequency shift Δf of the Brillouin peaks, due to scattering of the photons, is directly related to the phase velocity of the acoustic phonons v_{ph} (and thus to E) through¹⁰⁷

$$v_{ph} = \frac{\pi \cdot \Delta f}{k \cdot \sin(\theta_i)} \quad (31)$$

for the surface phonon mode and through

$$v_{ph} = \frac{\pi \cdot \Delta f}{n \cdot k} \quad (32)$$

for the bulk phonon mode. θ_i is the angle of incidence of the laser beam, k is its wave vector, and n is the refractive index of the material.

The technique was originally developed to investigate transparent materials, with a large interaction volume. Since its extension to opaque materials, with a small penetration depth resulting in surface sensitivity, it strongly depends on the development of high resolution Fabry–Pérot interferometers of the Sandercock type,¹⁰⁸ which are used in backscatter mode for higher sensitivity.

Ellipsometric porosimetry. Ellipsometric porosimetry can be used to extract the elastic modulus of porous materials from the same data used for the evaluation of the pore structure.¹⁰⁹ It exploits the miniscule reversible film shrinkage during capillary condensation of a liquid in the pores, which depends on the elastic modulus. By measuring the film thickness d as a function of the relative pressure (P/P_0) and fitting to

$$d = d_0 - k_{ep} \ln(P/P_0) \quad (33)$$

one can extract the constant k_{ep} from which the modulus can be calculated using

$$E = \frac{d_0 RT}{k_{ep} V_L} \quad (34)$$

Here the molecular volume V_L of the adsorbate is the only molecular characteristic needed for determining the elastic modulus.

2. Quantitative adhesion measurements

One of the major reliability issues for electronic devices is interfacial debonding driven by stresses in multilayer structures. These include both thermal stresses induced during operation and/or cooling after processing and residual intrinsic stresses created during deposition. Over the years the adhesion of thin layers has been studied by a wide variety of techniques. These include the simple Scotch tape test,¹¹⁰ several pull-off methods,^{111,112} shockwave-loading,¹¹³ and scratch testing.¹¹⁴ Relaxation of residual stresses in the stack during delamination hampers the ability of these methods to extract quantitative data on the interfacial fracture energy. A good overview of these and other methods is given by Chalker *et al.*¹¹⁵

Three quantitative techniques that have been developed recently are the sandwich structure four-point bending technique (SS4PB),¹¹⁶ the modified-edge liftoff test (m-ELT),^{117,118} and cross-section nanoindentation (CSN).¹¹⁹

Sandwich structure four-point bending Well defined tests exist for the evaluation of interface fracture energy of interfaces embedded in bulk materials.^{120–122} Building on this experience the sandwich structure four-point bending technique was developed for thin film stacks.¹¹⁶ Here the layers of interest are sandwiched between the original silicon substrate on which they were deposited, and a second substrate that is either glued or diffusion bonded to the stack.

After initiating a crack, the top surface of the sandwich structure is bent, causing the crack to propagate vertically towards the layers of interest. It is then deflected into the weakest interface, at which point the critical load, just suffi-

cient for incipient crack growth, can be determined. During crack propagation the interface fracture energy Γ_i equals the strain energy release rate, and is given by

$$\Gamma_i = \frac{21 \cdot (1 - \nu^2) M^2}{4 E w^2 h^3}, \quad (35)$$

where w and h are the width and thickness of the silicon substrate, ν is the Poisson ratio, and M is the applied bending moment. Residual stress relaxation is minimized because both parts of the stack are still fixed to a substrate. Additionally, the results are independent of crack length as long as the crack tip is sufficiently far from the precrack and the loading points.

When extracting the critical interface fracture energy, care should be taken with regards to the influence of plastic energy dissipation. A good demonstration of this was given by Lane and Dauskardt¹²³ for a Ta(N)/SiO₂ interface. In this work the samples were diffusion bonded using copper layers, deposited on top of the Ta(N), of a range of thicknesses. For a copper thickness below 0.3 μm the intrinsic Ta(N)/SiO₂ fracture energy $G_0 = 5 \text{ J/m}^2$ was found. For thicker copper layers a strong increase of up to 88 J/m^2 for a 20 μm layer was observed due to plastic dissipation. Note that this is also considerably higher than the fracture toughness of SiO₂ ($G_c \sim 10 \text{ J/m}^2$), indicating clearly how plasticity may help interface fracture resistance.

Modified-edge liftoff test. In the modified-edge liftoff test^{117,118} an epoxy of thickness h_e , with a known stress-temperature profile $\sigma_e(T)$, is applied to the stack of interest. The substrate is diced in order to create 90° edges and is subsequently cooled until debonding is observed. For a sufficiently thick epoxy the stored energy is approximately that of the epoxy itself and the fracture energy is given by

$$\Gamma_i = \frac{\sigma_e^2 h_e}{2E}, \quad (36)$$

where E is the elastic modulus of the failing layer. A study¹²⁴ comparing m-ELT with SS4PB for a Cu/Ta(N)/Ta/Si substrate stack shows a good correlation between the energies obtained, although the m-ELT data are systematically somewhat higher than those obtained with SS4PB.

Cross-section nanoindentation. For cross-section nanoindentation a cleaved sample is mounted vertically and an indent is made in the substrate several micrometers behind the stack of interest. A flat edge of the diamond tip is parallel to the stack and cracks are induced from its two corners during indentation. For a sufficiently weak interface, these cracks are deflected into the stack and delamination of the stack occurs at the weakest interface. For two regimes of the crack length, the system can be modeled as either a delaminated circular plate or an assembly of tapered beams. Solutions for both models are described in detail by Sanchez et al.¹¹⁹

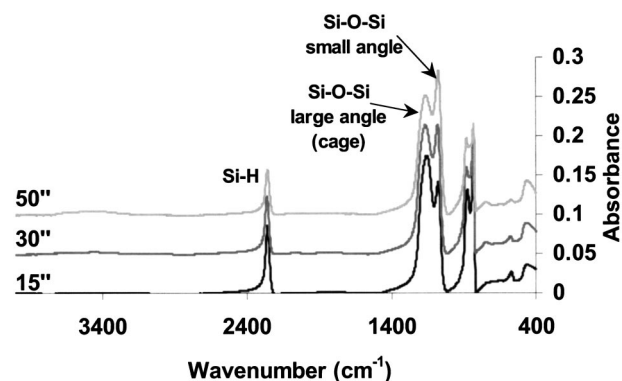


FIG. 33. FTIR spectra for HSQ based films prepared by the sol-gel process. The times in the insert indicate the duration of the NH₃ aging treatment. It can be seen that longer treatments correspond to higher loss of Si-H groups through hydrolysis reaction forming first silanol groups (Si-OH, absorbance peaks in the region above 3200 cm^{-1}) which can then undergo condensation leading to an increase in the total intensity for the absorbance peaks related to the Si-O-Si stretch bands (Ref. 132).

V. PROPERTIES OF LOW- k MATERIALS

A. Physico-chemical properties

1. Composition and stability

As discussed before, SSQ-based films can be found in both ladder and caged structures, depending on the two- or three-dimensional conformation of the monomers.¹⁴ The presence of caged structures, which can usually be recognized in FTIR spectra by an absorbance peak at 1150 cm^{-1} of the large angle Si-O-Si stretch band, induces lower film density.¹²⁵

One result is that constitutive HSQ-based films can have a density as low as 1.6 g/cm^3 , about one third less than tetraethyl orthosilicate (TEOS), (2.2–2.4 g/cm^3).¹²⁶ However, not all SSQ-based materials contain Si, O, and terminating groups R in stoichiometric ratios. The final film composition, as well as the ratio of cage to network bonds, can vary widely among films belonging to the same family, depending on the precursors, the conditions of film coating, and the curing. In particular, cure conditions are critical in determining the final film structure. For sol-gel based films it is the aging time in particular which has a strong impact on the structure of the dielectric material. FTIR spectra of HSQ based films prepared with different NH₃ aging treatments are shown in Fig. 33. Longer aging treatments result in a higher loss of Si-H groups through a hydrolysis reaction, with formation of silanol groups (Si-OH) as evidenced by adsorption peaks in the region above 3200 cm^{-1} . These groups can undergo a condensation reaction leading to an increase of Si-O-Si stretch bands. For longer aging times, a higher degree of cross-linking is achieved in the film, indicated by the increase in the small angle Si-O-Si absorbance peak.

Caged structures and the amount of R groups are highly sensitive to thermally activated redistribution processes^{127,128} and to oxidation reactions in the presence of low concentrations (10–20 ppm) of oxygen at temperatures above 350 °C.¹²⁵ In Fig. 34 FTIR spectra are shown for different spin-on SSQ-based dielectrics of equivalent thickness. It can be noted that the relative intensity of the peaks correspond-

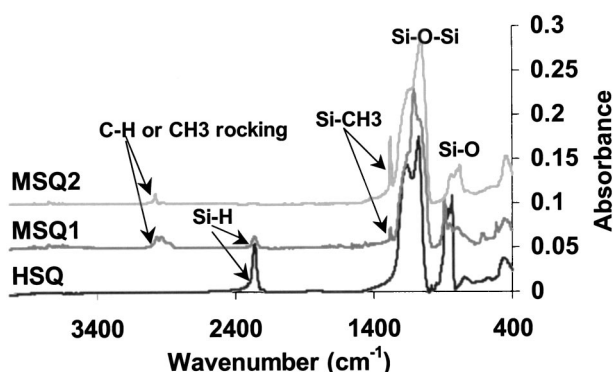


FIG. 34. FTIR spectra of a HSQ and two MSQ films with different organic content.

ing to the cage (1150 cm^{-1}) and network (1070 cm^{-1}) Si-O-Si bonds varies according to the specific material. For the HSQ-based dielectric an absorbance peak corresponding to Si-H bonds is observed around 2250 cm^{-1} , while for MSQ-based materials, typical CH_3 absorbance peaks appear around 2975 and 1275 cm^{-1} . All spectra present the typical absorbance peaks corresponding to the Si-O-Si stretch bands. The ratios of the small angle Si-O-Si band absorbance to the large angle absorbance differ for each material. The absorbance peaks in the region above 1500 cm^{-1} give an indication of the functional groups in the films: the Si-H adsorption peak is particularly pronounced in the HSQ film. It is present to a lesser extent in the MSQ based film with lower organic content. The CH_x stretch band absorbance peaks are present in both MSQ based films.

Also in terms of relative content of terminating groups large differences can be seen among the different dielectrics. In Table IV relative C content for different SSQ- and silica-based dielectric are compared in ERD measurements.¹²⁹ Cross-linking and material density of constitutively porous materials are lower than silica-based ones due to the presence of terminating groups.¹³⁰

In silica based materials, FTIR peaks reveal information about doping. Si-C, Si- CH_3 , Si-H, or Si-F bonds all produce measurable peaks. The dominating Si-O peak at 1040 cm^{-1} always has a shoulder at higher wavelengths. The shoulder is not to be attributed to the presence of cage-like structures (as in the case of SSQ-based materials). It is unclear what it is exactly due to,^{133,138} but it becomes more

TABLE IV. Elemental composition of Si-based low- k dielectric films as measured by ERD. Uncertainty is estimated at 2% for the shown elements, except for values related to H atoms, which can be subject to a relative uncertainty as high as 50%.

	Si %	O %	C %	H %	N %
HSQ	38	59	—	3	—
MSQ1	33	43	18	5	—
MSQ2	35	51	10	4	—
MSQ3	32	46	18	4	—
SiOC1	27	31	27	13	2
SiOC2	28	35	25	11	—

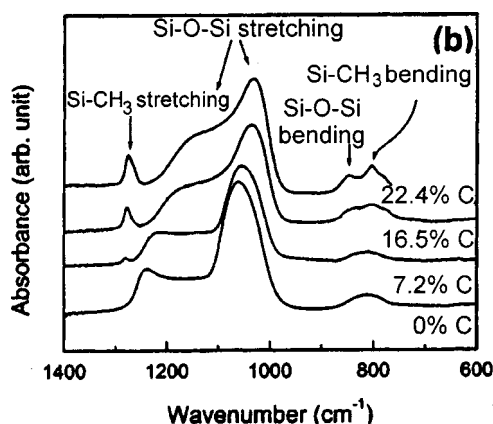


FIG. 35. FTIR spectra of silica-based films (SiOCH) with various carbon content (reprinted with permission) (see Ref. 131).

pronounced as the carbon content in the film increases as shown in Fig. 35.¹³¹

SSQ-based films do not typically decompose below $450\text{--}500\text{ }^\circ\text{C}$ in an inert atmosphere. Above this temperature, thermal desorption data by atmospheric pressure ion mass spectroscopy (APIMS) of HSQ-based films show an evolution of silane (SiH_2^+ and SiH_3^+ , respectively), indicating the onset of destruction of Si-H bonds.^{128,132} Si-methyl bonds are reported to be stronger than Si-H so that MSQ-based materials generally show higher thermal stability than HSQ-based films.¹⁴ In both cases prolonged thermal steps at temperatures above $500\text{ }^\circ\text{C}$ result in the loss of terminating groups and densification leading to transformation into SiO_2 -like films. All SSQ-based films show much lower thermal stability in an oxidizing atmosphere: for HSQ films the critical temperature for the onset of oxidation of Si-H bonds¹²⁵ was reported as $340\text{ }^\circ\text{C}$.

Silica-based films have better thermal stability, which is highest for fluorine-doped films because of the Si-F bond strength. No change in chemical composition or electrical properties are found after upon annealing up to $750\text{ }^\circ\text{C}$.^{133,136} If Si-H bonds are present in the film, decomposition starts at temperatures around $400\text{ }^\circ\text{C}$.¹³³ Carbon-containing bonds survive to higher temperatures. For example, Si- CH_3 bonds are reported to break starting at $500\text{ }^\circ\text{C}$.^{135,136}

It needs to be emphasized that the cage structure of SSQ is not very stable and can be decomposed to the more stable silica network. Such decomposition can be initiated by ultraviolet radiation or by high-energy particle interaction. This may explain why cage structures are not seen with plasma deposition. The thermal instability manifests itself in a strong decrease of a cage-related Si-O peak after $400\text{ }^\circ\text{C}$ anneal of SSQ-based material (see Fig. 36).¹³³

FTIR spectra of silica-based materials show almost no changes in Si-O peak shape when annealed at temperatures up to $500\text{--}600\text{ }^\circ\text{C}$.^{133–138} As is obvious from the spectra in Fig. 37, no reduction of the Si-O shoulder is observed, which is another confirmation that the main Si-O peak is not related to a cage structure.

The terminating groups in SSQ-based films play a water-blocking role, such that the films are normally hydrophobic.^{14,139} In this case the contact angle of the films

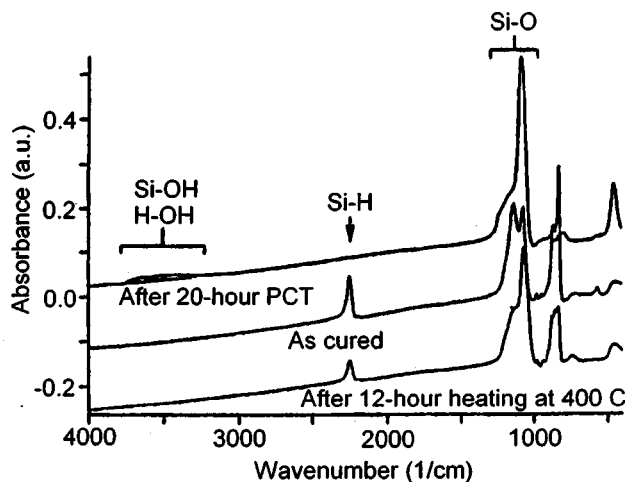


FIG. 36. FTIR spectrum change of HSQ during a heating test and a pressure-cooking test (2 atm, 120 °C, and 100% relative humidity) (reprinted with permission) (see Ref. 133).

with water is close to 90°. Depending on the amount of external and internal surface (due to porosity) exposed to the ambient, there is a minimal amount of terminating groups required in order to guarantee a hydrophobic behavior of the SSQ films. Moisture adsorbed by SSQ films can be either physisorbed, weakly bonded, or tightly bonded.^{140,141} The first can be easily desorbed at temperatures below 200 °C, the second type can be desorbed at temperatures around 400 °C. Tight bonding can occur when a considerable amount of R groups are lost due to thermal annealing, oxidation, or plasma damage. The Si–R bonds can be replaced by Si–OH bonds,¹²⁵ leading to tightly bonded silanol groups. This is irreversible and has a detrimental effect on the dielectric properties of the films.

Typical moisture uptake values in wt% are given for HSQ and MSQ films as 2.2 and 1.3, respectively.¹⁴ However, these values are strongly dependent on the porosity (constitutive and subtractive) and the amount of functional groups in the films. Additionally, the diffusion constant of water in a

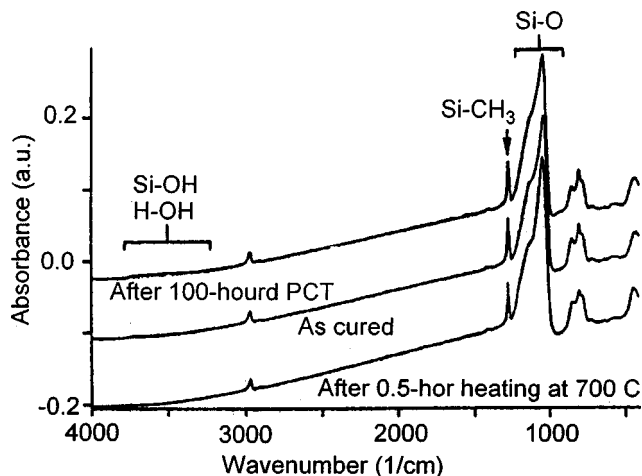


FIG. 37. FTIR spectrum change of silica-based glass during a heating test and a pressure-cooking test (2 atm, 120 °C, and 100% relative humidity) (reprinted with permission) (see Ref. 133).

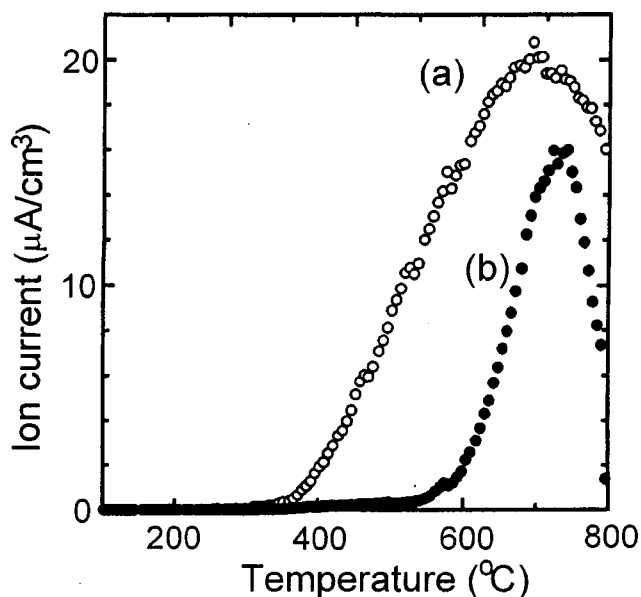
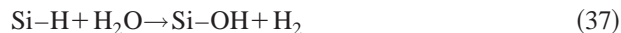


FIG. 38. Thermodesorption spectra for CH₄ molecules from SiOCH films with dense water-related species (a) and with very low water-related species content (b) (reprinted with permission) (see Ref. 137).

constitutively porous HSQ-based film has been reported to be about $3.6 \times 10^{-10} \text{ cm}^2/\text{s}$, measured by a quartz crystal microbalance method.¹⁴² It is expected to be significantly higher for mesoporous materials.

Water also plays an important role in the temperature stability of inorganic silica films, through the reactions.

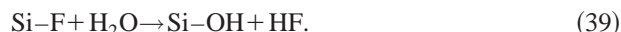


and



It was shown¹³⁷ that thermodesorption of CH₄ starts at 400 °C if water is initially present in the SiOCH film and only at 550 °C if a very low concentration of water is detected (see Fig. 38). After dehydration by gaseous XeF₂ at 200 °C both films showed similar thermal stability (up to 550 °C). Therefore, water promotes decomposition of hydrogen- or methyl-containing films. The effect of water on the thermal stability is one of the reasons of the lack of consistency in the literature. The higher water content results in a lower thermal stability.

As such, water adsorption influences not only the dielectric constant of low-*k* films, but also their integrity. In fluorinated silica, water reacts with Si–F bonds^{143,144} according to the following:



Such a reaction can occur at room temperature and leads to both the formation of undesirable hydrophilic Si–OH bonds and hydrofluoric acid which will attack the Si–O bond. Hence, fluorinated silica glasses cannot contain more than 10%–12% of fluorine (which corresponds to a *k* value of 3.3–3.4). Typical FSG contains only 5% F.

The most widely used organic low-*k* dielectric is an organic polymer,¹⁴⁵ which has a purely organic aromatic nature containing carbon (60 at. %), hydrogen (39 at. %), and oxy-

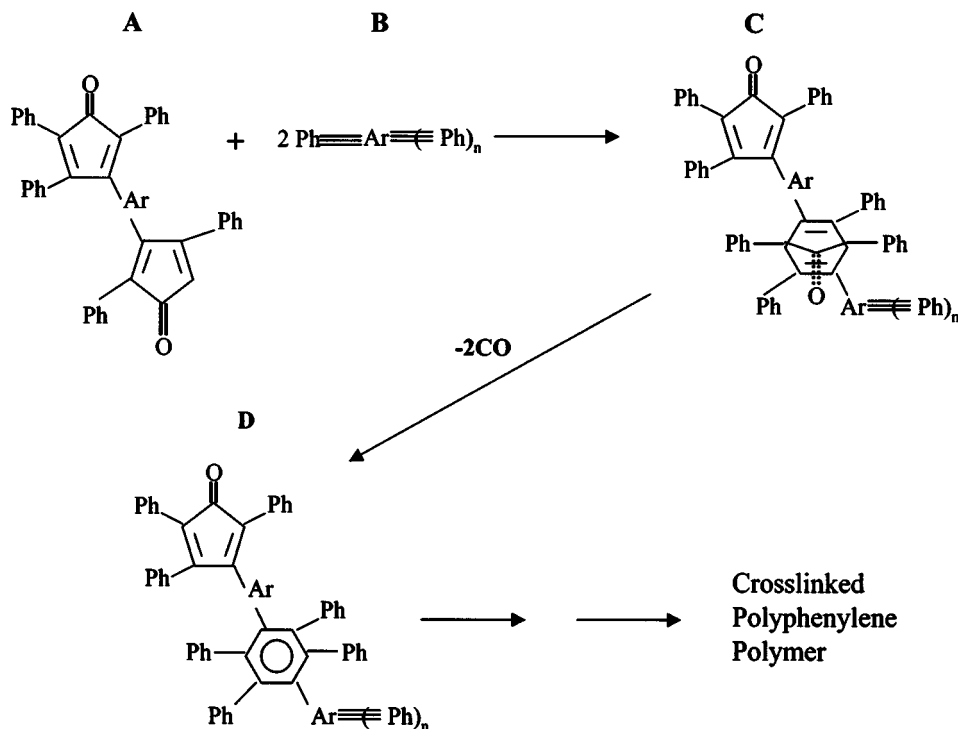


FIG. 39. Formation of a crosslinked polymer ($A+B \rightarrow C \rightarrow D$). Intermediate Diels-Alder (4+2) cycloaddition product (C) is formed by interaction of bi-functional cyclopentadienone cross linking agent (A) with acetylene type monomer/oligomer (B). Final aromatized and cross-linked polyphenylene (D) is driven by the extrusion of CO and the aromatization/formation of arylene functionality (see Ref. 145).

gen (1 at %).¹⁴⁶ It is a solution with a low molecular weight aromatic thermosetting polymer. After deposition on a substrate by spin-on technology, the polymer is thermally cured to an insoluble film with a high glass transition temperature (T_g). The formation involves the synthesis of cross-linked polyphenylenes by the reaction of polyfunctional cyclopentadienone- and acetylene-containing materials (Fig. 39).¹⁴⁵

Because of its aromatic nature, this organic polymer has a high thermal stability ($>425^\circ\text{C}$). Thermodesorption by RGA and APIMS has been reported for 800 nm thick films cured at $400\text{--}450^\circ\text{C}$.¹⁴⁷ The most pronounced desorbed species at low temperatures ($T < 200^\circ\text{C}$) have masses 2, 15–18, and 26–28 and are related to hydrogen, oxygen, water, and ammonia (mass 16–18). The peak intensities do not completely diminish in time until $T > 350^\circ\text{C}$. The peaks at masses 15–18 are related to water and small hydrocarbons. Peaks with mass 26–28 are also related to hydrocarbons (C_2H_4^+ , C_2H_3^+ , C_2H_2^+ , and probably N_2^+ and CO^+). At 200°C , the most intense peaks correspond to masses 40–44 (CO_2 and hydrocarbons such as C_3H_8^+). Also peak families appear with masses 57 and 71. However, these peaks (40–44, 57, and 71) become more pronounced only if wafers were exposed to air for more than 17 h (Fig. 40).

The peaks with masses near 44, 57, and 71 are possibly related to adsorption from cleanroom atmosphere, solid-state transformations, or oxidation of the film. These species are relatively weakly bonded and completely desorb at $T \geq 250^\circ\text{C}$. The integral desorption becomes more intense starting at $400\text{--}420^\circ\text{C}$. Most of the desorption peaks increase exponentially suggesting polymer degradation. At the same time, loss of film thickness and an increase in refractive index are observed as illustrated in Fig. 41.

The organic polymers of interest for low- k applications are hydrophobic. They adsorb only insignificant amounts of weakly bonded water, which can be easily removed by thermal annealing at a moderate temperature (Fig. 42). The water concentration in the organic polymer is much less than in silica based films and water molecules are not chemisorbed.¹⁴⁷ The increase in water desorption at $T > 500^\circ\text{C}$ is probably related to degradation of the film and oxidation from residual oxygen in the APIMS chamber.

2. Pore structure

In Sec. III of this review the various techniques to introduce pores were discussed. For the materials properties, it is not only the total porosity and pore size which are important, but also the pore connectivity.

The porous structure of SSQ-based materials is primarily determined by the way the subtractive porosity is introduced in the spin-on deposited films

Commonly, the pores of xerogel- and aerogel-based films have an interconnected structure with a relatively broad pore size distribution. The mesopores are typically connected by meso-channels, since this technique is based on solvent evaporation with no direct control over the porous structure.

Porogen based films have pore sizes related to the size of the chosen sacrificial nanoparticles (see Fig. 7). A desired pore structure can be achieved in which the mesopores are only connected by the constitutive porosity of the matrix material, usually micro-channels (necks of 1 or more orders of magnitude smaller than the mesopores).^{148,149} The uniformity in the distribution of the porogens throughout the film during cure is fundamental in avoiding or limiting coalescence/percolation, an issue that becomes critical for

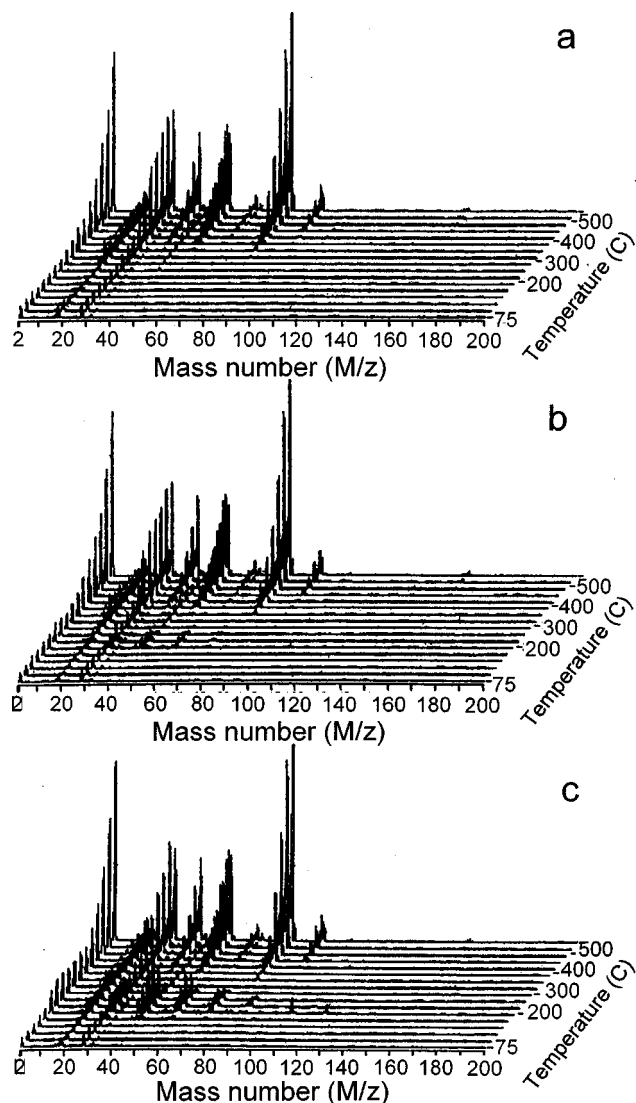


FIG. 40. Effect of air storage on the thermodesorption spectra. The curing temperature was equal to 375 °C. Storage time was equal to 2 h (a), 17 h (b), and 60 h (c). The temperature ramping speed was 1 °C/s.

increasing porogen loads.¹⁴⁹ When the porogens are chemically linked (grafted) to the matrix material, better control over the volume distribution can be achieved.¹⁵⁰ In the case of porous films, a monotonic increase of porosity may lead to complete interconnectivity of the pores. The pore interconnectivity may lead to deterioration of mechanical and thermal properties as well as film degradation during the different chemical treatments. Percolation theory is an important method to describe the flow of fluid, heat, charge etc. through a random medium. The simplest model considers a lattice of sites which are occupied with a probability p or not with probability $1-p$. Clusters are formed when neighboring sites are occupied. As this occupancy probability is increased, the clusters grow in size until a critical value (the percolation threshold, p_c). Around the threshold value, properties change abruptly.

A lot of discussion has been generated when percolation like phenomena were observed for positronium, Ps, formed inside of MSQ based films.³⁴ It was established that Ps escapes from the film with higher probability when the poro-

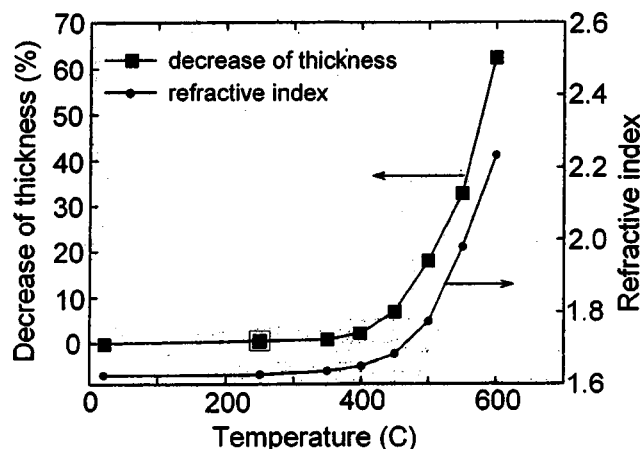


FIG. 41. Change of the refractive index of an organic polymer film and the decrease of the film thickness as a result of thermal annealing.

gen load is higher than 25 wt%. These observations were originally interpreted in view of a percolation threshold. However, the percolation threshold measured by PAS does not have a direct correlation with fluid and gas penetration and no dramatic changes of properties near the PAS percolation threshold have been observed.^{109,163}

Silica based materials can be non-porous (e.g., F doped silica), but most of them exhibit constitutive porosity (e.g., SiOCH obtained by CVD^{61,67}) or subtractive porosity (e.g., CVD SiOCH^{46,67} and spin-on porous silica).^{82,151} Constitutively porous films have a typical porosity of 5%–15% and a mean pore size of about 1 nm. Subtractive porosity can be as high as 70% and the mean pore size can reach values as high as 10 nm.

The porosity of organic polymers is still under investigation. Indeed some constitutive porosity is present in the film related to the solvent extraction process and polymerization process during spin on deposition and cure. This free volume can be compared to some extent to the constitutive microporosity of silica based low- k dielectrics as becomes evident from the swelling of organic polymers during wet treatment (see later section). A systematic study is, however, not available. Several different versions of subtractive organic polymers have been reported using porogen

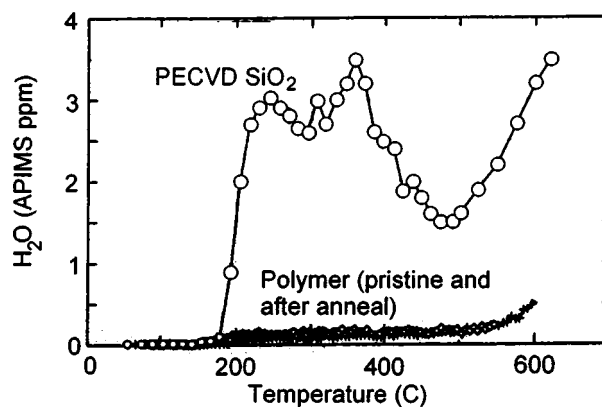


FIG. 42. Thermodesorption spectra of water from PECVD SiO₂ and a organic polymer film (APIMS data).

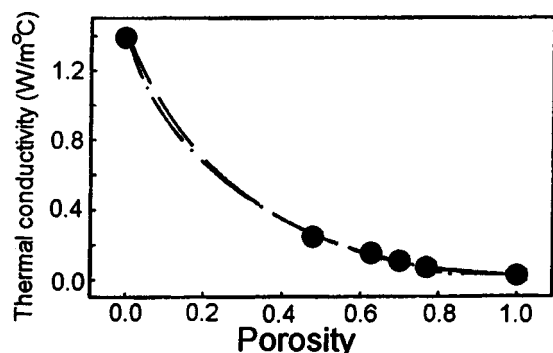


FIG. 43. Effective thermal conductivity of a xerogel film vs porosity. The dots present experimental results by the 3ω technique. For comparison, PWSM (porosity weighted simple medium) and PWDm (porosity weighted dilute medium) models are shown together (reprinted with permission) (see Ref. 155).

technology.¹⁵² Early generations of porous films contained large voids (>100 nm) that hampered integration efforts. New generations of porous organic polymer films have a much smaller subtractive pore size on the order of 5 nm.

It should be mentioned that only the average pore size and pore size distribution have been discussed. They indeed define many of the characteristics of the material and some aspects related to process compatibility. In order for a material to be fully characterized for process compatibility, the pore sizes in the high end of the distribution (i.e., large pores) are of utmost importance. There are no systematic studies of this issue. First attempts to gain insight into the presence and consequences of these outliers will be discussed in Sec. VI.

3. Thermal conductivity

The thermal conductivity of low- k materials is lower than that of SiO_2 . Thermal conductivity is highly dependent on the total porosity of the material, both constitutive and subtractive.

Extensive studies have been conducted on xerogels and HSQ-based films with subtractive porosity.¹⁵³ Costescu *et al.* reported that constitutively porous HSQ films show a thermal conductivity of about $0.4 \text{ W m}^{-1} \text{ K}^{-1}$ (as compared to $1.3\text{--}1.35 \text{ W m}^{-1} \text{ K}^{-1}$ for SiO_2). For an HSQ-based film with 50% subtractive porosity, a value between 0.155 and $0.170 \text{ W m}^{-1} \text{ K}^{-1}$ was reported.¹⁵⁴ Also in this case, it is speculated that the pore structure has a strong influence on the actual value of thermal conductivity.

Thermal conductivity of silica-based low- k films also depends strongly on film porosity. Thermal conductivity values for nonporous films are close to those of SiO_2 [1.2 W/(K m)].¹³⁷ However, with increasing porosity a strong decrease in thermal conductivity (more rapid than the relative dielectric constant decrease) is observed down to 0.3 W/(K m) at 50% porosity (see Fig. 43).¹⁵⁵ One organic polymer was reported to have a thermal conductivity of 0.19 W/m K .¹⁴⁵

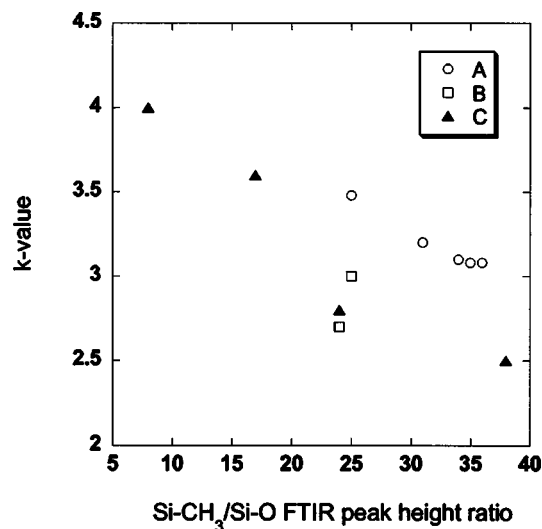


FIG. 44. Dielectric constant of carbon-doped silica as a function of carbon content. Carbon content is supposed to be proportional to the Si-O/Si-CH_3 FTIR peak ratio. (A) data by Han *et al.*, Ref. 134 (B) data by Wu *et al.* (Refs. 135 and 136), and (C) data by Kim *et al.* (Ref. 158).

B. Electrical properties

HSQ-based films are reported to have a dielectric constant in the range of $2.8\text{--}3.0$,¹³⁰ while MSQ films generally show slightly lower values of $k \approx 2.7\text{--}2.9$. No constitutive porosity was detected with EP for HSQ films, whereas, some constitutive porosity has been reported by EFTEM.¹⁵⁶ Most MSQ-based films show a significant percentage of constitutive microporosity by EP, accounting for up to 17%–18% of the film volume.¹⁴⁹

The dielectric constant of silica-based materials can be varied from 4 to around 2 depending on doping and porosity. The basic nonporous silica (conventional silicon dioxide) has a k value of 4. By introduction of fluorine, the k value can be reduced to $3.2\text{--}3.4$ at 10–12 at. % of F due to the lower polarizability of the Si–F bond as compared to Si–O.

Carbon or CH_x doping helps in reducing the k value down to $2.7\text{--}2.8$ (see Fig. 44). Such a decrease has two origins: first, polarizability of Si–C bonds is less than that of Si–O bonds, and second, substitution of oxygen by larger CH_x groups decreases film density, giving rise to constitutive porosity. The ultralow- k values (close to 2.0 or even below) can be achieved using subtractive porosity.

Organic polymers dielectrics have a dielectric constant as low as 2.65.¹⁴⁵ The additional factor of providing minimum frequency dispersion is probably related to the high glass transition temperature (T_g). High T_g and glass–rubber temperatures hinder rotation of the main chain backbone because they are effectively “frozen in” below these temperatures. Relaxation observed in this region can only be attributed to side chain rotation or to “local” movement of small portions of the chain backbone.

Increasing porosity is one way to reduce the k value of an existing material. Low initial dielectric constants, based on low polarizability of the material, make it possible to achieve low- k values for lower total porosity as indicated in Fig. 45.

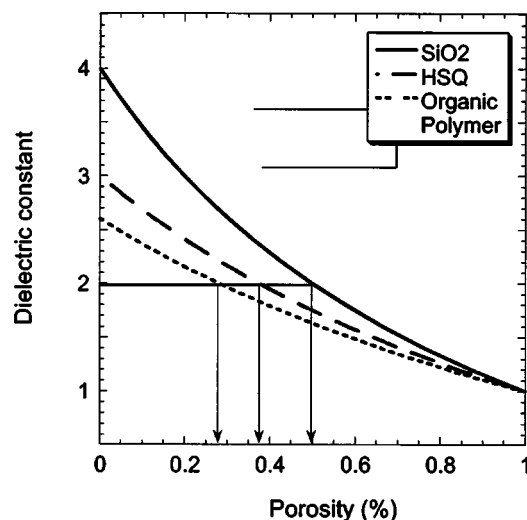


FIG. 45. Dielectric constant vs porosity calculated using the Clausius-Mossotti Eq. (15).

For example a mesoporous HSQ-based material with about 50% total porosity is reported to have a k value of about 1.9,¹⁵⁷ while the k value for an MSQ-based dielectric with about 45% total porosity lies at around 2.0.¹⁴⁹

For interconnect performance, it is very important that the dielectric constant remains stable once integrated into a structure. The contribution from orientation polarization varies significantly with the amount of moisture trapped in the films. The presence of porosity and/or dangling bonds due to plasma damage enhances the possibility of trapping physisorbed and/or chemically bonded moisture in the dielectric layers. To guarantee such a requirement, it is fundamental to minimize degradation of the dielectric during processing steps. Densification of the material and/or loss of hydrophobic behavior, due to for example plasma interactions, should be minimized. It should be noted that the extent of dielectric degradation during processing can be substantial especially in the case of highly porous materials.

In Fig. 46 a comparison between measured and simulated interline capacitance versus line spacing is shown for an HSQ-based dielectric with about 50% porosity. The val-

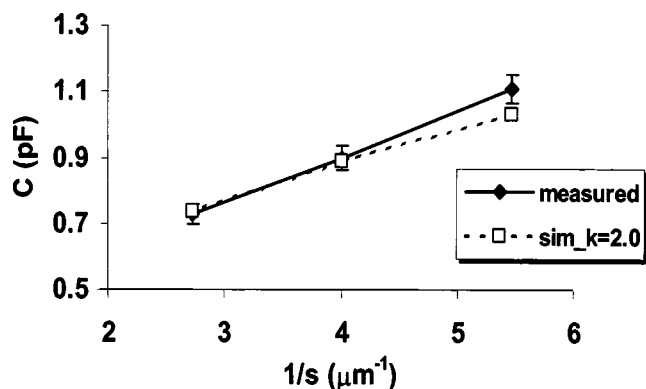


FIG. 46. Comparison of measured and simulated interline capacitance values (100 kHz), assuming a 2.0 dielectric constant for the interlevel dielectric. The dielectric is in this case an HSQ-based material with 50% porosity. S refers to the spacing between the metal lines.

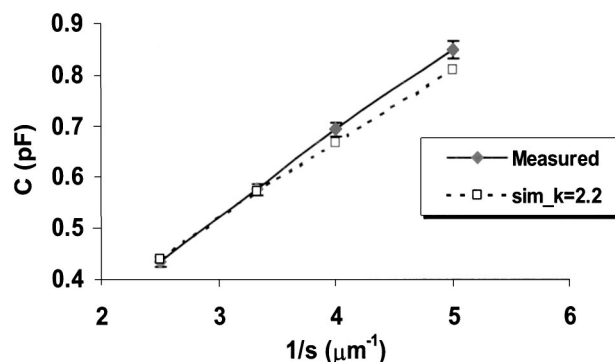


FIG. 47. Comparison of measured and simulated inter-line capacitance values to simulated ones, assuming a 2.2 dielectric constant for the interlevel dielectric. The dielectric is in this case an aromatic polymer with about 20% porosity.

ues are assessed for different line spacings. Clearly the agreement between measured and simulated data degrades for smaller spacings, which is an indication of the fact that the dielectric sidewalls have, to some extent, been degraded by processing. The effect on inter-line capacitance of a degradation of the dielectric is limited to a few nm at its sidewalls and will clearly be more pronounced for the smallest spacings. The same trend is also visible in Fig. 47, where a similar study has been performed using an aromatic polymer with 20% porosity and with an initial dielectric constant of 2.2.¹⁵⁸ Minimization of degradation of dielectric sidewalls is one of the most important compatibility issues in low- k dielectrics processing.

Figures 46 and 47 are shown as examples which confirm that by thorough optimization, good results can be obtained. It remains unclear whether process optimization can suffice as dielectric spacings continue to scale down and porosity continues to increase.

SSQ based, silica-based, and polymer dielectrics have been optimized and processed with acceptable electrical properties. The leakage current density is in the range of 10^{-8} – 10^{-9} A/cm² at an electric field of 1 MV/cm. The breakdown voltage is in the range of 2–5 MV/cm.^{65,137,138,159,160} Even though they are considered acceptable, these values do not compare favorably with a typical leakage current density of 10^{-9} – 10^{-10} A/cm² for lines embedded in SiO₂ and a breakdown voltage higher than 6 MV. The origin of the leakage currents has not been studied in enough detail. More insight needs to be gained into the conduction mechanism and breakdown mechanism in low- k dielectrics.

C. Mechanical properties

The properties of low- k materials are tuned preferentially to obtaining a low dielectric constant, but their structural integrity should also be carefully considered. In particular, the introduction of subtractive porosity compromises both the elastic modulus and the structural integrity of these materials.

TABLE V. Elastic moduli and hardness values for several low- k dielectrics.

Classification	Porosity (%)	E_R (GPa)	H (GPa)	Thickness (nm)
MSQ1	Constitutive	3.65	0.57	400
MSQ2	45	1.2	0.13	400
Organic polymer 1	Constitutive	4.1	0.25	400
Organic polymer 2	20	2.58	0.12	400
Silica-based 1	6–8	6.2	0.9	406
Silica-based 2	Constitutive	8.5	...	400–2000
Silica-based 3	16	3.6	...	600–1000
MSQ 3	40	1.84	0.24	405

1. Modulus and hardness of various low- k films

Table V summarizes the values for the elastic modulus and hardness obtained for a variety of deposition techniques and level of subtractive porosity. For reference the thickness of the layer on which the data are extracted is also indicated.

Clearly, the introduction of subtractive porosity into the films leads to a drastic decrease, which at present, can only be described by empirical models. Some groups reported a linear dependence, which is highly dependent on the porous structure of the dielectric,¹⁶¹ while other groups reported a quadratic dependence.¹⁶²

Typically, MSQ-based materials, engineered with subtractive techniques to achieve around 45%–50% porosity, show an elastic modulus of around 2 GPa or below. Hardness values show a much broader variability, since the determination of this characteristic for thin films is dependent on the method and conditions of the measurement.

Figure 48 shows the variations in E and H as a result of an increasing level of porogen loading for an MSQ based material. An almost linear weakening of the material is observed. A comparative study,^{163,101} using 1 μm MSQ based layers with several levels of subtractive porosity was made in order to evaluate the reliability of the measurement techniques described in Sec. IV. Figure 49 shows that similar values can be obtained with all techniques. Although some disagreement with nanoindentation data was originally reported, in-house measurements showed good correspondence with the other methods. Similar studies on thinner layers are in progress.

No precise (published) data are known about the plasticity of SSQ-based materials. In our experience, they tend to be less brittle than ceramic-based materials (they show some plastic deformation). Fracture toughness for constitutively porous HSQ films is reported as $0.2\text{--}0.3 \text{ MPa m}^{1/2}$.¹⁶⁴

2. Adhesion

Interfacial adhesion in Copper/low- k interconnects is a critical issue. Good correlation between fracture toughness and CMP survival rate was recently shown by Sherban *et al.*¹⁶⁵ who evaluated the adhesion of a range of carbon-doped oxides, spin-on polymers, and spin-on glasses to Ta, Ta(N), and Ti(N) barrier layers. All interfaces having energies below 5 J/m^2 led to either thin film delamination or cracking. The same limit was found for different film stacks during packaging and reliability testing, indicating that this

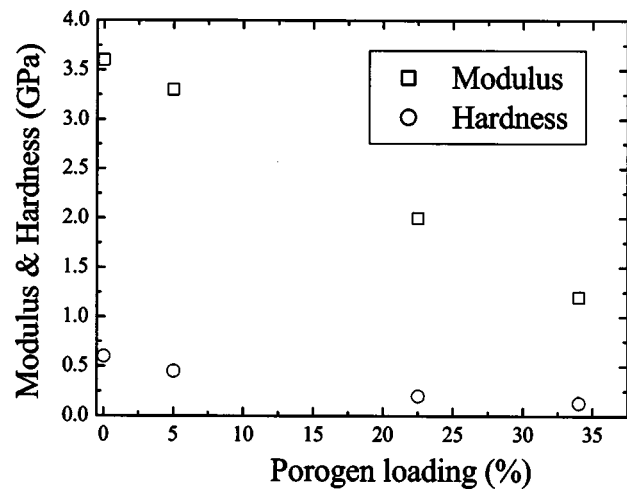


FIG. 48. Modulus and hardness variations for an MSQ-based material with subtractive porosity, introduced by various levels of porogen loading.

number does not depend strongly on the materials used. However, as indicated by Maitrejean *et al.*,¹⁶⁶ the value is obtained for a specific CMP process and in fact they show good CMP performance for an MSQ based material on various liners for values down to $G_c = 2.7 \text{ J/m}^2$.

Surprisingly, interfacial adhesion to “cap” or “liner” layers is relatively insensitive to porosity, even though the elastic modulus changes drastically. Kloster *et al.*¹⁶⁷ show only a minor decrease in adhesion when 45% subtractive porosity is introduced, while Maidenburg *et al.* relate an observed increase for porous MSQ to the higher surface roughness.¹⁶⁸ However, subsequent surface treatments of the porous structure do have a significant effect. An ozone treatment on MSQ, for instance, has a negligible effect on the dense structure but increases the adhesion energy significantly for the porous material,¹⁶⁷ even leading to a change in fracture path. Improvements may be obtained by creating a certain degree of hydrophilicity at the studied interface

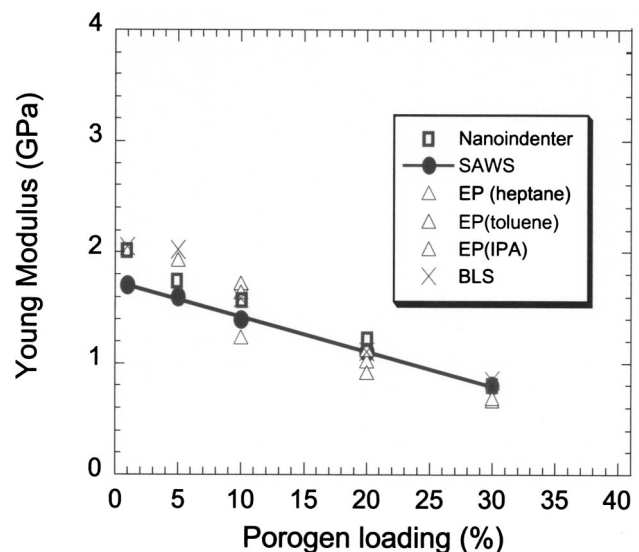


FIG. 49. Comparison of nanoindentation (in house), EP (in house), SAWS and SBS (Ref. 163) for obtaining the elastic modulus of an MSQ based material.

[plasma and/or ultraviolet (UV) ozone], but also by cleaning and increasing the roughness of the underlying layer (especially by plasma treatments).

Typically the adhesion energy of SSQ-based films to various cap layers is in 3.5–5.3 J/m² range, and is systematically lower when compared to the adhesion of organic polymeric films.¹⁶⁷

3. Thermal expansion

SSQ-based films usually show low intrinsic stresses, from 20 to 50 MPa, mainly due to a gradual evaporation of residual solvents. HSQ-based materials have been found to possess a coefficient of thermal expansion (CTE) value of about $20 \times 10^{-6} \text{ }^{\circ}\text{C}^{-1}$ and a Poisson's ratio close to 0.34^{169,142} (by bending beam technique and x-ray reflectivity). There are no data available about the CTE of silica based materials.

The thermomechanical properties of an organic polymer have been reported.¹⁴⁵ The CTE was found to be 66 ppm/°C in a free-standing film during an anneal to 400 °C. It was also proven that the glass transition temperature exceeds 490 °C.¹⁷⁰

The tensile properties of an organic polymer film were determined on free-standing films using a special procedure as described by Im *et al.*¹⁷¹ The modulus for a cured organic-polymer film equals 2.45 ± 0.04 GPa, while the ultimate tensile strength is 90 ± 4.1 MPa. Biaxial stress in a organic polymer film deposited on a silicon substrate is 60 MPa. The stress drops linearly as the sample is heated, reaching a null value at the cure temperature. This linear behavior is reversible during repeated cycling.¹⁷²

A fracture toughness of 0.62 ± 0.04 MPa m^{1/2} was found for an organic polymer film using the m-ELT technique.^{145,173} It is also important to note that the elastic modulus and CTE change abruptly above T_g . The decrease of modulus and increase of CTE due to the increasing viscous flow lead to a concern of the dimensional stability of the polymer.

VI. PROCESS INTERACTIONS

In this section we will discuss the most important process interactions with low-*k* dielectrics, i.e., the ones that will finally determine the “process compatibility” of the material. The main process interactions of interest are the interactions with plasmas, issues related to the deposition of thin films on top of porous dielectrics, and the need for pore sealing.

The discussion is limited to a systematic description of interactions and consequences. Process integration issues are not discussed, as they are not within the scope of this review.

A. Interaction of low-*k* dielectrics with plasmas

Plasma processing plays an important role in advanced interconnect integration. Plasma reactors are mostly used for etching of trenches and vias as well as for resist strip and postetch cleaning. Plasma treatments also become important to change surface properties of low-*k* materials.¹⁷⁴ Of course any treatment should leave the dielectric constant of the film unaltered.

Several types of plasma are used in low-*k* processing. Fluorine- or fluorocarbon-containing gases, oxygen, and hydrogen are mostly utilized to obtain reactive species in the plasma, while inert gases (like helium or argon) dilute reactive gases and provide additional ion bombardment in the case of reactive ion etching (RIE).

The goal of this section is to give an overview of recently obtained results on the interaction between low-*k* materials and different plasmas.

1. SSQ-based materials

Oxygen plasma. An oxygen plasma is known to have a negative effect on SSQ-based low-*k* glasses such as MSQ,¹⁷⁵ HSQ,¹⁷⁶ and their porous versions.^{177,178} Although porous silica films should be formally discussed in the section of silica-based materials, their behavior in plasmas is similar to SSQ-based materials.¹⁷⁹ The reason for this is that they contain a significant amount of hydrophobic organic groups. These include Si-CH₃ and Si-H and are removed by an oxygen plasma, resulting in an increased water absorption as indicated by FTIR. An increased amount of water was also found by means of thermodesorption^{177,179} and results in an increasing dielectric constant,^{177,178} (*k*-value increase with oxygen plasma treatment as illustrated in Fig. 50) which can be as high as 37 after oxygen plasma treatment.

The refractive index of films measured *in situ* during oxygen plasma processing was found to increase.^{201,180} Moreover, SSQ-based low-*k* materials (especially porous) shrink in an oxygen plasma.^{200,201} Structural changes propagate towards the substrate as was found by positron annihilation spectroscopy.¹⁷⁶ In fact, porous SSQ-based materials suffer more severely from an afterglow oxygen plasma than from an RIE oxygen plasma,¹⁷⁸ as can be seen from the stronger OH peak in the FTIR spectrum in Fig. 51. Ion bombardment probably induces the formation of a dense layer on the top surface and thus slows down penetration of the oxygen atoms. Another reason can be the competition between oxidation and sputtering of the oxidized layer, resulting in a lower net amount of oxidation.

Despite the negative effects of an oxygen plasma treatment, an N₂O plasma was reported to have a positive effect on MSQ glass.¹⁸¹ The SOG became more resistant towards oxygen plasma treatment. This resistance was attributed to the creation of a passivation layer induced by the N₂O plasma.

Fluorocarbon containing plasma. A fluorocarbon plasma is commonly used for pattern transfer into SSQ-based glasses. After such plasma exposure, the low-*k* surface is covered with fluorocarbon polymers. The more polymerizing the chemistry (e.g., C₄F₈ versus CF₄) the thicker the formed polymer film and the lower the etch rate.^{182,183} In contrast to organic polymers, fluorine does not seem to diffuse into nonporous films and e.g., RBS reveals no changes in film composition.¹⁸⁴

Hydrogen plasma Liu and Chang, *et al.* published a number of papers on hydrogen plasma treatment of SSQ-based materials.^{185–189} They found that it blocks copper diffusion into SSQ-based low-*k*'s,¹⁸⁵ reduces leakage,^{186,187} and increases material resistance to oxygen plasma treatments.¹⁸⁸

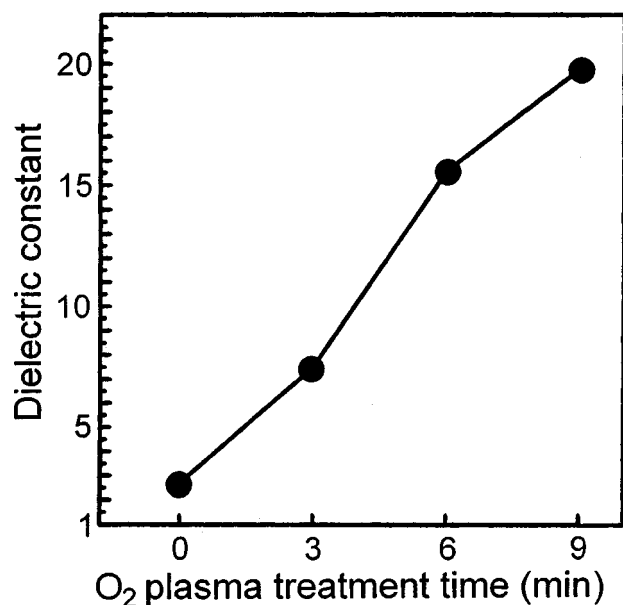


FIG. 50. The dielectric constant of MSQ film with O₂ plasma treatment (300 mTorr, rf power 300 W, 300 °C) as a function of the treatment time.

A positive effect was also found employing a deuterium plasma treatment.¹⁸⁹ The authors attribute the positive effect of hydrogen (deuterium) to passivation of dangling bonds inside the low-*k* material. A hydrogen plasma was also found to be a good candidate for resist stripping.¹⁹⁰ The refractive index, thickness, and *k* value of HSQ remain unchanged during a downstream N₂/H₂ plasma treatment. At the same time photoresist/HSQ etch selectivity was found to be as high as 100 at low pressures.

2. Silica-based materials

There are two main types of silica-based low-*k* materials (except for porous silicas which were discussed in the previous section): fluorinated silicon dioxide (or SiOF) and silicon oxycarbide (or SiOCH). The materials interact with a plasma in different ways. The behavior of SiOF during interaction with plasmas is very similar to that of SiO₂, the only difference is an increased etch rate due to the presence of fluorine in the film.^{201,180}

Oxygen plasma. Generally, SiOCH materials degrade in an oxygen plasma similarly to SSQ-based materials. However, the SiOCH (CVD deposited silica-based) low-*k* dielectrics are more stable in an oxygen plasma than conventional organo-silicate glasses (OSG) (spin-on silica-based materials).¹⁹¹ This is illustrated by Fig. 52, where the dielectric constant and thickness loss of OSG and SiOCH are plotted as a function of oxygen plasma pressure. Nevertheless, an oxygen plasma treatment removes carbon- and hydrogen-containing species from the top layer converting it to a SiO₂-like hydrophilic material,^{191,192} resulting in an increased *k* value. The thickness of the converted layer significantly increases with an increase in film porosity (see Fig. 53).¹⁹²

Fluorine-containing plasma. Exposure of SiOCH films to a fluorocarbon plasma shows the same result as for SSQ-based films. The top surface is covered with fluorocarbon polymers, however, no increase of fluorine was found inside

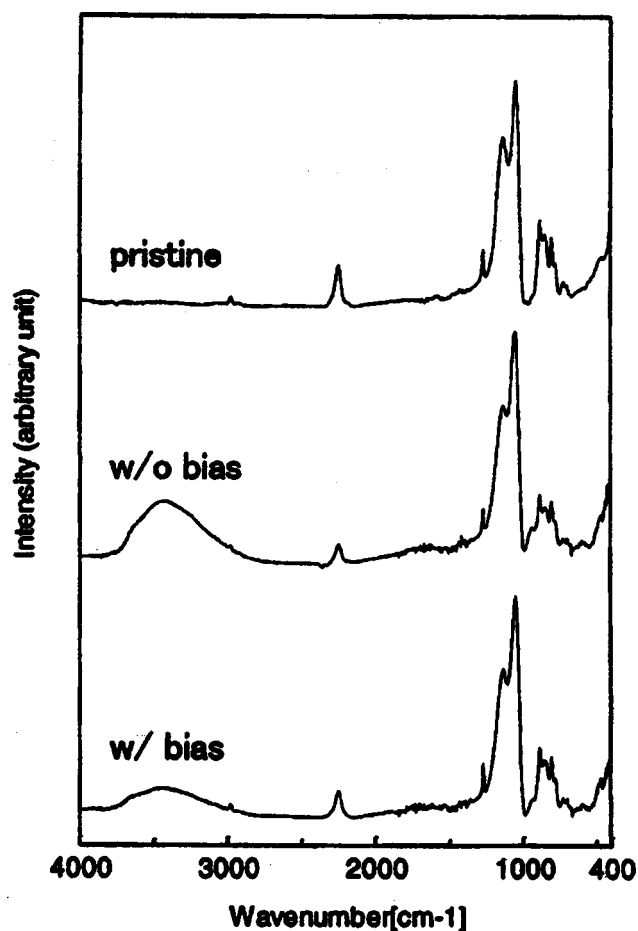


FIG. 51. FTIR spectra of pristine porous HSQ film and the same film after biased and nonbiased oxygen plasma (pressure 5×10^{-6} Pa, volumetric plasma density 0.05 W/cm³, substrate area power density (if any) 0.16 W/cm², substrate holder temperature 30–35 °C) (reprinted with permission) (Ref. 178).

the film.¹⁹² It should be noted that increased porosity does not result in an increased fluorine penetration depth as evidenced by time of flight-secondary ion mass spectrometry (TOF-SIMS) profiling.¹⁹²

Fluorine-oxygen plasma mixture. For SiOCH, a fluorine-oxygen plasma mixture has a maximum in etch rate at a certain oxygen/fluorine ratio (see Fig. 54).¹⁹² As mentioned above, an oxygen plasma creates a SiO₂-like layer on the top surface of the SiOCH film while a fluorocarbon plasma creates a low volatile CF_x polymer. In both cases the etch rate, especially in the absence of ion bombardment, is very low. When both oxygen and fluorine are present in the plasma, the SiO₂-like layer induced by the oxygen plasma can be easily etched by a fluorocarbon plasma. When the fluorine/oxygen ratio is optimal, the oxidation rate is equal to the oxide etch rate and the total etch rate is maximal. A similar effect was found for SiCH films,¹⁹³ but the optimal fluorine/oxygen ratio was shifted towards a higher oxygen concentration because SiCH needs more oxygen than SiOCH to be oxidized to SiO₂.

Hydrogen plasma. No changes in SiOCH films after hydrogen plasma treatment were found by means of FTIR, ellipsometry (refractive index and thickness), and water contact angle measurements.¹⁹²

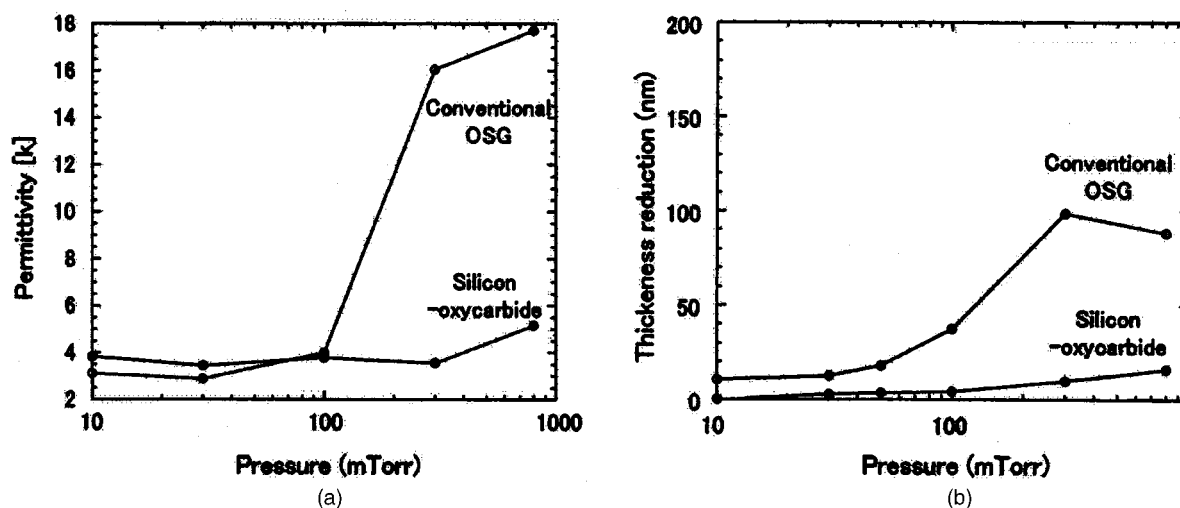


FIG. 52. The dielectric constant (a) and thickness loss (b) of OSG and SiOCH as a function of oxygen plasma pressure (rf plasma power 1.6 W/cm^2 , treatment time 1 min) (reprinted with permission) (see Ref. 191).

3. Organic polymers

Oxygen plasma. An oxygen plasma is widely used for etching of organic polymers due to the high reactivity of oxygen with organic compounds. Highly volatile products of polymer oxidation such as CO_x and H_2O are easily formed and desorbed from the surface. It is known that after interaction with a pure oxygen plasma the surface of polymers is oxygen enriched.^{194,195} XPS analysis of the $\text{O}(1s)$ and $\text{C}(1s)$ spectra¹⁹⁴ shows that in the case of a downstream plasma oxygen primarily forms $\text{C}(\text{OH})_2$ and $\text{C}(\text{OH})_3$ compounds with carbon and hydrogen at the surface. However, in the presence of ion bombardment the total amount of oxygen on the surface decreases and most carbon atoms are bonded to at most one oxygen atom by $\text{C}-\text{OH}$, $\text{C}-\text{O}-\text{C}$, and $\text{C}=\text{O}$ bonds.¹⁹⁴ In the case of ion bombardment in an oxygen deficient plasma (less than 40% of oxygen in O_2/N_2 or O_2/Ar plasma) so called “graphitization” of the polymer surface has been observed.¹⁹⁶ As shown in Fig. 55 the $\text{C}(1s)$ XPS peak shifted towards 283.5 eV (which corresponds to pure graphite) after such a plasma exposure.

The thickness of such a “graphitized” layer increases with increasing surface bias (i.e., ion bombardment) and a decreasing oxygen concentration in the plasma (i.e., when there is not enough oxygen to remove the graphitized layer) as shown in Fig. 56.

During plasma exposure, hydrogen and oxygen are sputtered from the polymer, leaving behind the carbon skeleton of the polymer. The effect is similar to that observed for photoresists when exposed to aggressive plasmas.^{197,198}

It is important to note that only the top surface of organic polymers appears to be modified after oxygen plasma exposure. No changes were revealed either in FTIR spectra or in optical constants (refractive index) for organic polymer films after treatment in a pure oxygen plasma.¹⁹⁹

Fluorine-containing plasma. In contrast to an oxygen plasma, a fluorine-containing plasma etches organic polymers with a low rate,²⁰⁰ especially in the absence of ion bombardment.^{199,201} A fluorine-plasma easily breaks $\text{C}-\text{H}$ and $\text{C}-\text{C}$ bonds, forming nonvolatile CF_x ($x < 4$) polymers.

After fluorine plasma exposure the surface of the dielectric is typically covered with such polymers as was found by XPS analysis. This fluorocarbon polymer film is found to be formed even when the nonpolymerizing fluorine-containing plasmas, such as NF_3 or SF_6 , are used.^{199,202} The fluorinated top surface appears to be hydrophobic according to water contact angle measurements. An increase from 78° to 110° of the water contact angle of an organic polymer film was reported after 120 s exposure to a CF_4 plasma.²⁰⁰

Unlike an oxygen plasma, a fluorine-containing plasma modifies not only the surface of low- k polymers, but also their bulk properties. These changes manifest themselves, for example, in a decrease of the refractive index with exposure to fluorine containing plasmas.^{199,201} The incorporation of fluorine is known to lower the refractive index of polymers.^{203,204} The presence of fluorine in low- k polymer films was confirmed by FTIR spectra where F-related peaks appeared after fluorine plasma exposure^{199,202} (Fig. 57).

It is believed that fluorine from the plasma diffuses into the polymer. Due to a limited diffusion rate, the polymer is partially fluorinated from the top surface down. The fluorinated layer thickness depends on the exposure time and the fluorine concentration in the plasma.¹⁹⁹ The effect is more pronounced when a downstream plasma is used,^{199,201} because the fluorinated layer is being etched in the presence of ion bombardment and the total amount of fluorine in the film after etching is less.^{200,201} The fluorinated polymers show a decrease in water absorption according to thermodesorption measurements.^{200,147} Simultaneously the k value decreases due to the lower polarizability of fluorine-containing bonds.^{199,202}

Fluorine–oxygen plasma mixture. In a fluorine–oxygen plasma mixture the polymer etch rate was found to have a maximum at a specific fluorine concentration (see Fig. 58).^{195,199}

At low oxygen concentration fluorine forms nonvolatile polymers as was described above. If a substantial amount of oxygen is present in the plasma it breaks $\text{C}-\text{F}$ chains, form-

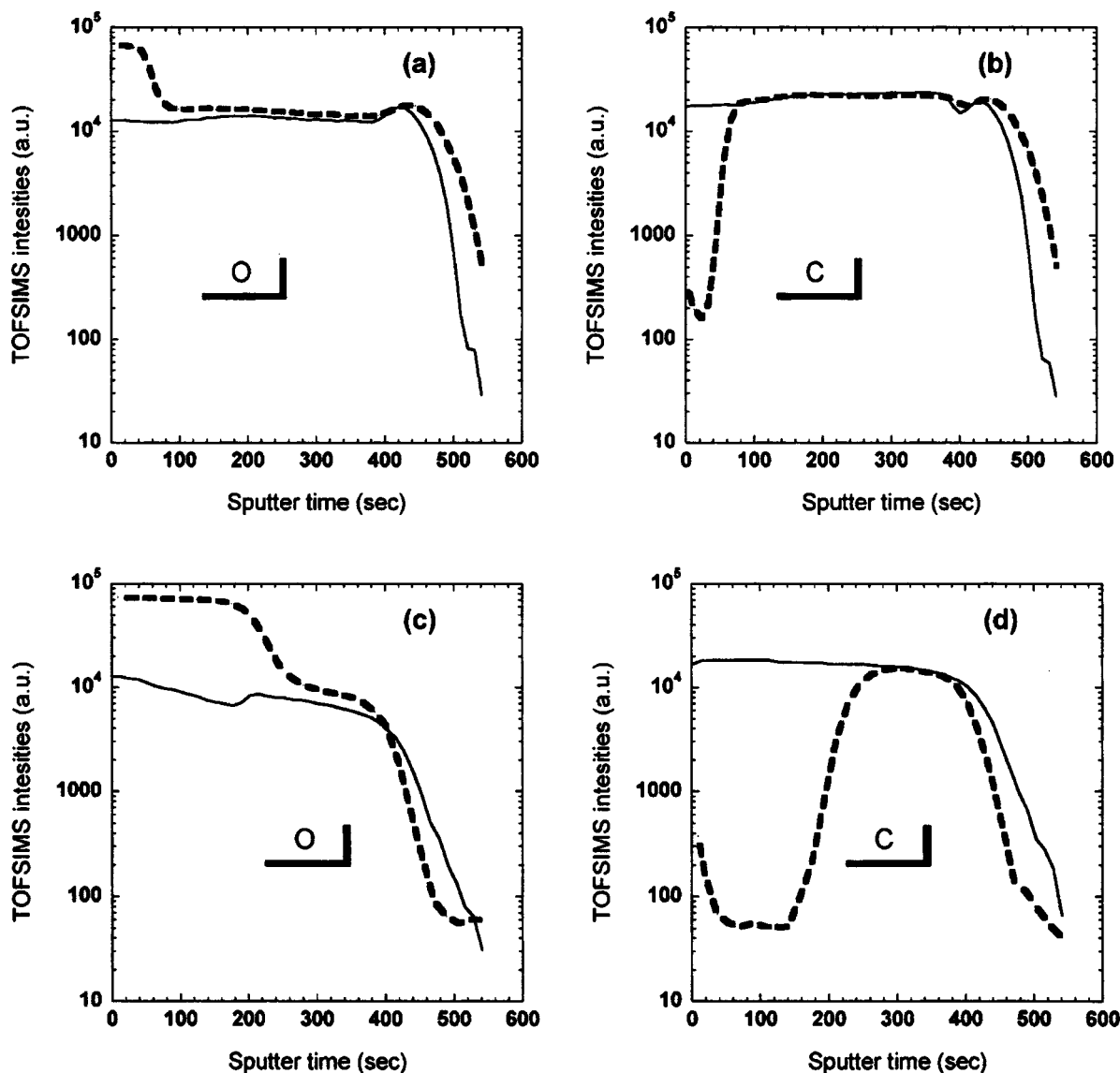


FIG. 53. Concentration profiles of O and C obtained by TOF-SIMS for: (a),(b) low porous (7%) and (c),(d) highly porous (40%) SiOCH films before (thin solid curves) and after (bold dashed curves) oxygen plasma treatment (pressure 40 mTorr, rf power 430 W, grounded substrate, at room temperature) (see Ref. 192).

ing volatile products. However, oxygen-rich plasmas are less effective in producing volatile compounds due to the lower reactivity of oxygen. During RIE fluorine-containing polymer chains can be broken by energetic ions which provides a substantial etch rate even in fluorine-rich plasmas.¹⁹⁵

Hydrogen plasma. A hydrogen plasma can also be used for etching of organic polymers, because the interaction of a hydrogen plasma with polymers produces volatile compounds CH_4 and H_2 . The hydrogen plasma also has a lower etch rate as compared to an oxygen plasma which can be used for improving profile control.²⁰⁵ A mixture of hydrogen and nitrogen plasma has a higher etch rate during RIE as compared to a pure nitrogen or pure hydrogen plasma. Hydrogen ions are too light to provide sufficient ion bombardment, while nitrogen ions hardly form volatile compounds. The combination of nitrogen ion bombardment and hydrogen reactivity results in a maximum etch rate at about 80% of hydrogen (as illustrated by Fig. 59).¹⁹⁶

However, the hydrogen plasma tends to increase mois-

ture absorption. After hydrogen plasma treatment, the water contact angle had decreased slightly (from 78° to 68° after 120 s) and the amount of water, as measured by thermodesorption, increased.²⁰⁰ Nevertheless, the k value seems to be unaffected by the treatment.²⁰⁰

Chlorine-containing plasma. Generally, the etch rate in chlorine-containing plasmas is lower than for fluorine-containing ones due to the lower reactivity of chlorine.¹⁹⁵ Chlorine tends to diffuse into the polymer, as was also observed for fluorine, forming CCl_x compounds within the polymers.²⁰² Incorporation of chlorine into a polymer results in an increase in the k value due to the higher polarizability of chlorine-containing bonds.²⁰²

B. Swelling of low- k dielectric films in liquid media

Interlayer dielectric films can be significantly affected when interacting with liquids during various technological steps. Swelling of low- k dielectric films in liquids causes an

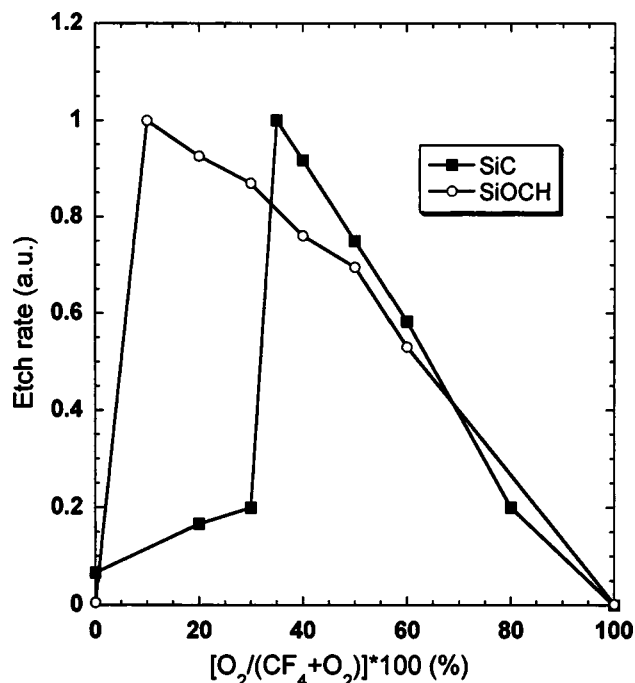


FIG. 54. Etch rate of SiOCH and SiCH as a function of fluorine content (CF_4) in fluorine/oxygen (CF_4/O_2) plasma mixture. Etch rates were normalized to allow direct comparison because experiments were carried out on different tools (see Ref. 192).

uncontrollable change of film volume. The degree of swelling during adsorption depends on the overall rigidity of the film skeleton.

In mesoporous low- k films the degree of swelling is minimal (in agreement with results of NMR analysis). Small

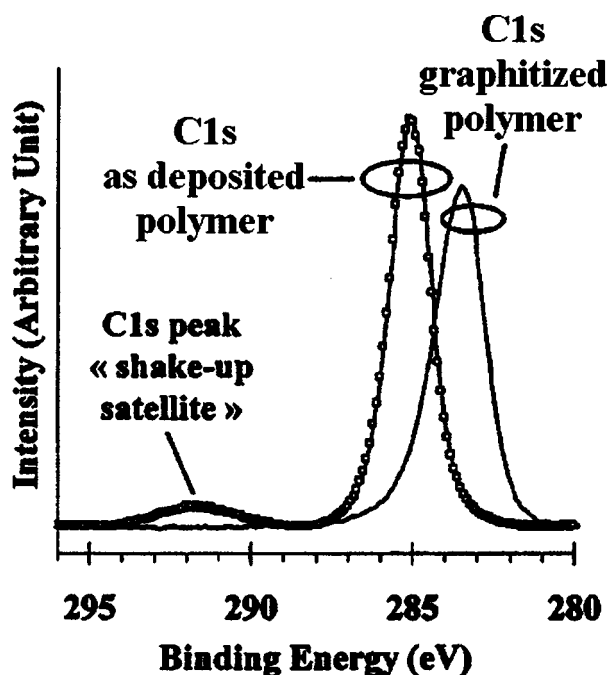


FIG. 55. $\text{C } 1s$ XPS spectra of an organic polymer dielectric as deposited (binding energy: 285 eV) and exposed to an Ar plasma leading to a graphitization of the surface (binding energy: 235 eV). The etching conditions are: 1500 W source power, 1 W/cm^2 bias power, 2 mTorr, 20 °C chuck temperature, and Ar flow rate of 70 sccm. (reprinted with permission) (see Ref. 194).

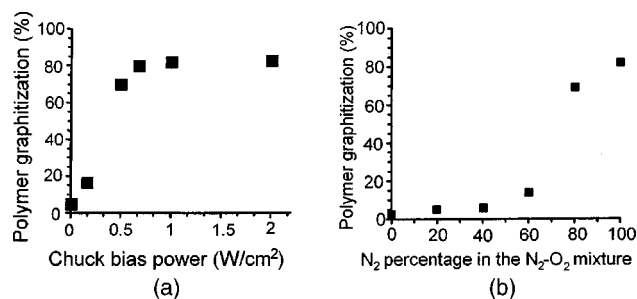


FIG. 56. Graphitization of the polymer surface in a N_2/H_2 (20 sccm/40 sccm) plasma as a function of the rf power applied to the wafer (a) and in a N_2/O_2 plasma as a function of N_2 percentage (b). Graphitization percentage is determined as a ratio between graphitized layer thickness and XPS penetration depth (≈ 10 nm) (reprinted with permission) (see Ref. 194).

reversible shrinkage/swelling is related to capillary forces that appear during solvent condensation in mesopores.¹⁰⁹

The situation is more complicated in the case of microporous films and organic polymers. In fact, polymer free volume and microporosity exhibit similar behavior with respect to swelling. The driving force for adsorption in micropores, with a size of a few molecular diameters, is the overlap of potential fields from neighboring walls. It enables activated diffusion of adsorbate molecules into the film matrix through a channel bounded by polymer segments (model DiBenedetto and Paul).²⁰⁶

According to the theories of adsorption, absorption, and desorption in micropores has to occur without hysteresis.⁹¹ However, in some cases isotherms exhibit a kind of hysteresis which persists to even the lowest pressure; some adsorbate is retained even after prolonged outgassing and can only be removed at an elevated temperature (Fig. 60). An explanation for the low-pressure hysteresis is proposed by Arnell and McDermott²⁰⁷ in terms of swelling of the particles which accompanies adsorption. The swelling distorts the structure and some “closed” pores, which were previously inaccessible to the adsorbate molecules, can be opened. Since the distortion is not perfectly elastic, some molecules become trapped and can escape only very slowly, or possibly not at all, unless the temperature is raised.

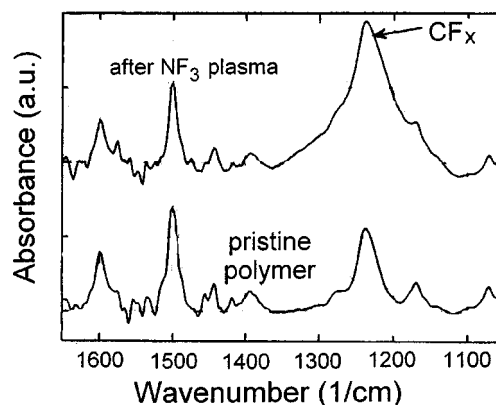


FIG. 57. FTIR spectra of an organic polymer low- k dielectric, as-deposited and after pure NF_3 afterglow plasma treatment (see Ref. 199).

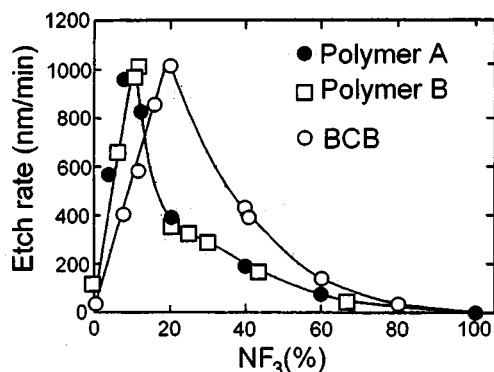


FIG. 58. Etch rate dependencies of various organic polymers on the NF_3 percentage in NF_3/O_2 plasma afterglow (see Ref. 199).

C. Thin film deposition on porous dielectrics

The deposition of a thin film on top of a porous material is nontrivial. Thin film deposition techniques have all been optimized for deposition on nonporous substrates. The porosity of the substrate may translate into a porous thin film, which has a large impact on its functionality as a protective capping layer, a diffusion barrier etc., both for metallic and dielectric thin films.

Thin film deposition is commonly performed by means of vapor deposition techniques, which can be either physical vapor deposition (PVD) or CVD vapor based. To a more limited extent, also spin-on film depositions on top of spin-on low- k dielectrics is of some interest, even though spin-on deposited films are generally low-density films, and will not be treated here.

PVD growth is strongly influenced by the surface morphology of the substrate. For metallic PVD thin films, the sheet resistance of the deposited films is a useful indicator of the quality of homogeneity.

It has been observed that the deposition of thin PVD Ta(N) on blanket dielectric films follows the long range topography of the porous substrates.¹⁴⁸ An analysis of the power spectral densities from AFM scans shows that this is particularly true for spatial wavelengths down to 100 nm,

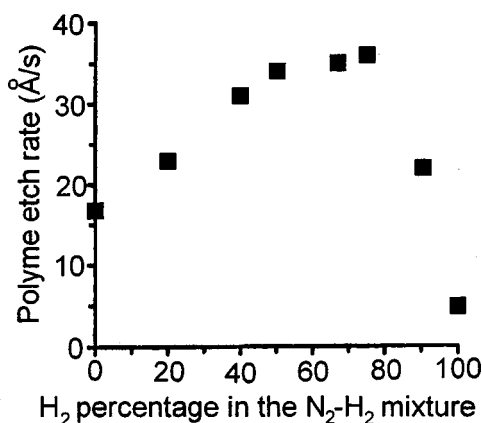


FIG. 59. Etch rate of an organic polymer as a function of the H_2 percentage in the N_2/H_2 gas mixture. The etching conditions are: 1500 W rf power, 1 W/cm² substrate bias power density, 2 mTorr, 20° chuck temperature, and total flow rate of 50 sccm (reprinted with permission) (see Ref. 196).

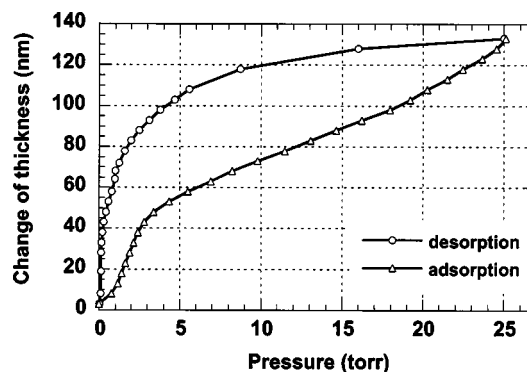


FIG. 60. Change of thickness (swelling) and low-pressure hysteresis in the adsorption of isopropyl alcohol on organic low- k film at room temperature. Initial film thickness is 500 nm.

below which a substantial cutoff occurs. The sheet resistance exhibits an almost linear relationship with roughness rms value on microporous dielectrics (Fig. 61). This confirms that the roughness of the substrate is the dominating parameter in the behavior of sheet resistance of thin PVD-deposited Ta(N) films.²⁰⁸ Indeed, an increase in roughness of the substrate implies an increase in the total surface to be covered by the same amount of species. This leads to a decrease in the effective thickness of a film sputtered on top of a rough substrate.

For mesoporous dielectrics, one has to differentiate between mesoporous with microconnectivity and mesoporous with mesoconnectivity.

For the latter, a significant increase in the sheet resistance of thin conductive films occurs which is related to the substrate porosity. A simple model predicts the increase in sheet resistance for this case since all the pores at the surface will remain open after capping by Ta(N).¹⁴⁸ For a given porous volume fraction P in the dielectric film, the porosity appearing at the surface will be equal to P . We can assume for a very thin cap layer (not yet “bridging” the pores) that this amount of porosity would be transferred to the cap, as shown in Fig. 62.

Under this condition, the lateral area of the current rings generated by a four-point probe measurement corresponds to a reduced effective area A_{eff} approximately $(1 - P)$ times smaller than the area in a continuous film [the current would flow perpendicular to the cross section shown in Fig. 62(a)]. The expressions for sheet resistance measurements by a four-point probe²⁰⁹ with aligned and equally spaced pins, will become

$$R_s = \{ \pi / [(1 - P) \times \ln 2] \} V/I. \quad (40)$$

For mesoporous substrates with a microconnectivity or with a “closed” structure, this effect does not appear since these pores can be covered without introducing porosity in the cap layer [Fig. 62(b)].¹⁴⁹

The increase in sheet resistance is a first indication of the integrity of the deposited thin film in terms of pinholes. It was observed that the presence of a partially porous diffusion barrier leads to the degradation of the porous dielectric, which was attributed to contamination during the subsequent metallization process.²¹³ If no special precautions are taken,

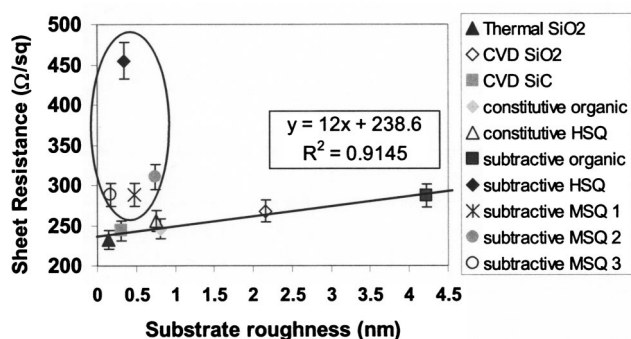


FIG. 61. Sheet resistance vs surface roughness of the substrate (rms from AFM scans). This graph shows that the increase trend of sheet resistance for PVD-deposited Ta(N) films on different constitutive dielectrics is dominated by the dielectric roughness. The behavior on top of most of the mesoporous subtractive dielectric films (highlighted by a circle), except for the subtractive organic material, does not follow the linear trend. This is due to the contribution of porosity and pore structure (see Ref. 148).

PVD thin films will contain pinholes. These are often very difficult to detect, and not visible in cross-sectional TEM.

CVD, onto micro- or mesoporous dielectrics, suffers from severe precursor penetration since they can diffuse through the porous structure of the dielectrics. The parameters by which the precursor diffusion is affected are mostly linked (as in the case of etching and stripping chemistries) to the reactants lifetime, their diffusion coefficient into the specific pore structure, and to the reactivity of precursor with the low- k surface (reaction or mass transfer limited). This holds as well for the recently developed atomic layer deposition (ALD).²¹⁰

A worst case scenario in terms of precursor diffusion is shown in Fig. 63 when an ALD deposition is performed onto a mesoporous dielectric with mesoconnectivity: the precursor can penetrate (and initiate some deposition in the form of islands) through the entire dielectric layer. This is illustrated in Fig. 63. ALD precursors penetration has also been observed in microporous carbon-doped oxides.²¹¹

Also for PECVD depositions onto porous low- k films, precursor penetration was observed on mesoporous dielectrics. It was seen during SiO₂ deposition by SiH₄/N₂O on a porous HSQ-based film, that the bulk of the dielectric can be

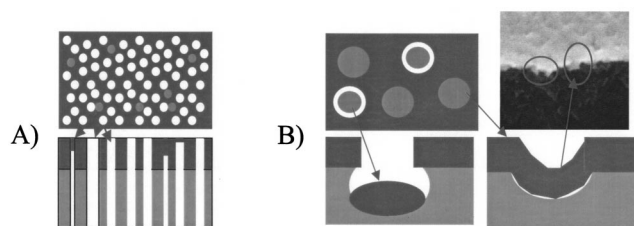


FIG. 62. Coverage behavior of thin PVD-deposited films on top of mesoporous dielectrics with: (A) an "open" pore structure (mesopores connected by mesochannels) and (B) a "closed" pore structure (mesopores connected by microchannels or dielectric free volume). In the first case, the only sealing possibility is by bridging the pores. In the case of "closed" pores, the PVD deposition can follow the pore morphology with no need for bridging. Shadow effects are possible [see scheme (B)], leaving sporadic pinholes in the capping layer (see Ref. 148).

detrimentally affected by the oxidizing species in the chamber, due to their fast diffusion through the mesoporous network.²¹² A degraded performance in terms of capacitance behavior for such films was reported even when the oxidation seemed to affect only the surface of the dielectric. Moreover, it was observed on the same material that there is penetration of organic precursors during PECVD SiC:H deposition (by trimethylsilane and Ar flow) of at least 200 nm of the film (Fig. 64).²¹²

From these data, it can be concluded that both PVD and CVD based thin film deposition suffer from pinhole formation and/or precursor penetration, which leads to functionality degradation of the thin film and possibly to an uncontrolled interaction between the processing ambient and the dielectric. This can be fatal in terms of electrical performance and reliability.²¹³

D. Pore sealing

In order to avoid the problems encountered in the previous section, porous dielectrics need to be sealed before further treatment. This need extends even further than for thin film deposition since any exposure, even to ambient, will lead to contamination of the dielectric, e.g., with moisture. In the first place, an accurate characterization of pinholes and sealing defects has to be established. Subsequently pore sealing procedures can be studied.

1. Characterization of sealing defects

Two techniques have been reported to measure thin film integrity on porous materials: PALS^{89,90} and EP.^{149,214,215} In both cases a barrier prevents a probe (positronium in the case of PALS and solvent vapor in the case of EP) from penetrating into (or escaping from) porous material.

In the case of PALS, a continuous barrier prevents positronium to escape from a porous material to vacuum (see Fig. 23) before significantly decreasing positronium lifetime (see Fig. 24). Using this technique the Ta or Ta(N) barrier deposited on porous silica with 6.9 ± 0.4 nm diam pores was found to be noncontinuous at a thickness of 25 nm. Although 35 and 45 nm thick Ta and Ta(N) layers were equally effective as positronium barriers, only the Ta-capped samples were able to withstand heat treatments of up to 500 °C without breakdown or penetration into the porous film. Ta(N) interdiffusion into the silica pores is indicated by the reduction of the positronium lifetime after high annealing temperatures.

When EP is used as a thin film integrity probe, a continuous barrier prevents solvent vapor (toluene) from penetrating in a porous film. As a result, no change in optical properties of a porous film is registered by ellipsometry when the film is exposed to the vapor. On the other hand, a noncontinuous barrier allows solvent vapor to penetrate into the film and changes its optical properties. An example of the ellipsometric response (Ψ and Δ angles) recorded during exposure of a porous SSQ-based (5 nm pore size, 50% porosity) film with a Ta(N) barrier (PVD deposited) is shown in Fig. 65.

The noncontinuous barrier of 30 nm [Fig. 65(a)] does not stop solvent from penetrating and experimental points

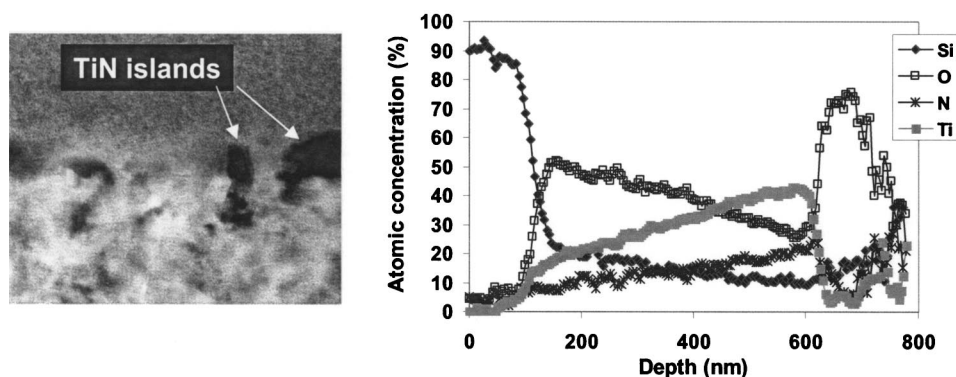


FIG. 63. Depth profiles by EF TEM of a 500 nm thick HSQ film with subtractive porosity after the deposition of 20 nm (nominal thickness) of ALD TiN. Severe precursor penetration is revealed by the presence of significant amounts of Ti and N throughout the porous film. Moreover, the deposited TiN layer is highly discontinuous: the TEM cross section reveals an island-growth regime.

follow the theoretical curve. When the thin film is continuous [Fig. 65(b)] experimental points do not follow the theoretical curve indicating there is no solvent adsorption inside the porous film. The small change in Ψ and Δ is attributed to solvent condensation on top of the Ta(N) barrier. Similar results are obtained for barriers deposited on organic polymers. The EP technique is also able to reveal low-density defects (several defects per square mm). Solvent is trapped beneath such defects making them visible through the optical microscope. Examples of such defects in an ALD WCN barrier deposited on a low- k polymer are shown in Fig. 66.

2. Pore sealing by thin film deposition

The sealing performance of a deposition process is dependent on the nature of the deposition process itself in combination with the morphological and chemical nature of the surface to be sealed. From a sealing point of view, the pore structure of a low- k film can be classified in three main categories: only microporous, mesoporous, with microconnections and mesoporous with mesoconnections. Depending on the porous structure, a CVD or a PVD-based barrier deposition process can show different sealing performances. Pore sealing simulations can be helpful in understanding the processes occurring during thin film deposition on porous substrates.

Systematic studies were reported comparing sealing performance of thin barriers for PVD depositions. It was shown that a 10 nm Ta(N) barrier can easily bridge and seal the microporous volume of a constitutive MSQ-based dielectric.¹⁴⁹ The addition of nanoparticles (porogens) in the silsesquioxane resin precursor leads to mesopores ($\langle d \rangle = 3-4$ nm) interconnected by microchannels given by the original microporosity of the MSQ resin, as also shown by a bimodal pore size distribution.³³ The same PVD Ta(N) thickness on the subtractive mesoporous versions of this dielectric film with only microconnections, still efficiently seals, because pores appearing at the surface can be closed by deposition from the bottom, as shown in Fig. 67. Only when the subtractive porosity of the film is increased above a critical value (22% in the mentioned case), the sealing of such a thin barrier layer is no longer effective because part of the microconnections are converted into mesoconnections.¹⁴⁹ These pores will need to be “bridged” by during PVD deposition, so that a substantially thicker Ta(N) layer is needed to achieve an efficient sealing. Indeed, in order to seal a meso-

porous HSQ-based dielectric with comparable pore size ($\langle d \rangle = 4-5$ nm), but with fully interconnected pores through mesoconnections, a Ta(N) thickness above 30 nm is needed.^{214,216}

A similar behavior for a thin PVD layer is seen on top of an organic porous low- k with only microconnections and average pore size around 15 nm. As can be seen in Fig. 62, PVD Ta(N) film follows the pore features appearing at the surface.¹⁴⁸ However, shadowing effects can hinder PVD coverage due to the relatively large pore size so that a thickness above 30 nm is needed to avoid pinholes.

This particular behavior of a PVD film on a porous dielectric makes it a suitable instrument for the characterization of porous structures. This can be done by a combined analysis of sheet resistance and surface roughness.¹⁴⁸

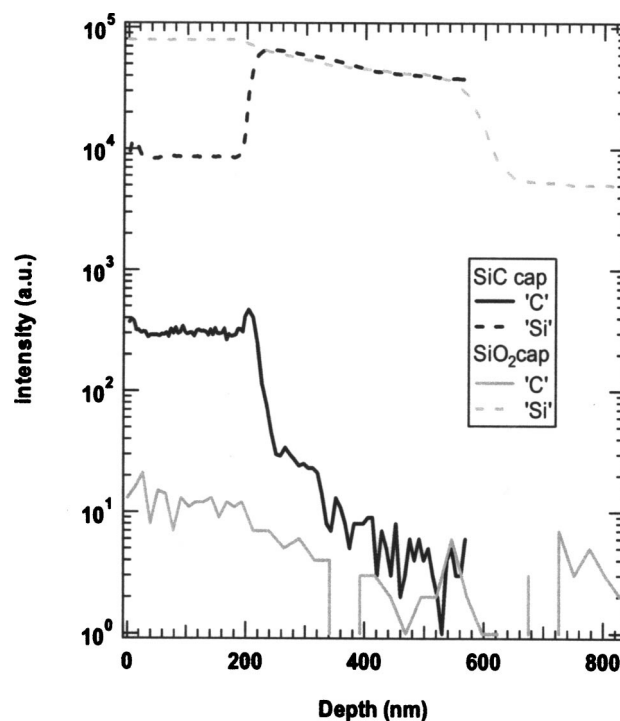


FIG. 64. Comparison of the C and Si concentration profiles by TOF-SIMS analysis in porous HSQ layers capped either by 200 nm SiC:H or SiO₂ CVD depositions. In the case of SiC:H cap, the C profile is still detected with significant intensity down to about 200 nm in the bulk of the porous HSQ film, indicating precursor penetration through the porous network. The low- k dielectric is mesoporous with about 50% porosity (see Ref. 212).

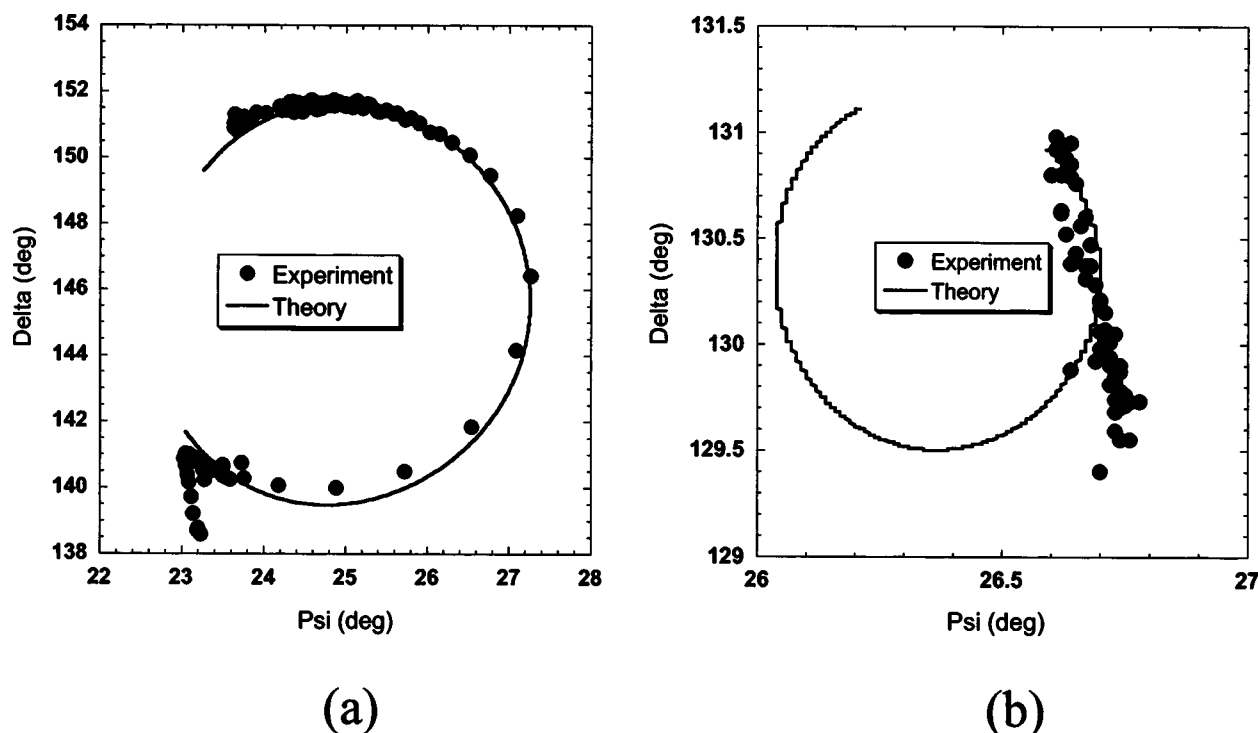


FIG. 65. Ellipsometric angles Ψ and Δ recorded during exposure of a porous HSQ film with 30 nm Ta(N) (a) and 60 nm Ta(N) (b). Continuous curves represent calculated theoretical changes of Ψ and Δ supposing the barrier is porous (see Refs. 214 and 215).

3. Simulation of pore sealing by thin film deposition

To better understand the pore sealing mechanism of porous low- k materials one can use simulations. A Monte Carlo (MC) simulation is used for the investigation of deposition processes and surface relief evolution on an atomic scale.^{217–219} Most simulations employ a two-dimensional (2D) solid-on-solid (SOS) concept, where an atom can only be placed on top of another atom and overhanging configurations above voids are forbidden. There are only a few models that allow a geometrical overhang of thin films over the pore structure. Three-dimensional (3D) models are much less developed and the few studies which do exist are not considered pore sealing.^{220–222} However, pore formation during growth has been investigated.²²³ Some analogy to pore sealing is described by Dew *et al.*,²²⁴ where the authors used a 2D MC model for simulation of aluminum deposition on a surface with initial pits in the micron range. For low- k ma-

terials, or amorphous compounds in general, there are practically no publications concerning MC simulations. In fact, even pore sealing of a Si substrate was described only recently.^{225–227} An investigation of pore sealing as a function of the nature and/or structure of a porous material was carried out for the (111) surface of a diamond-like crystal.^{225–227} Realistic results for the dependence of thickness and shape of the sealing layer on growth conditions were obtained. Also, the (111) surface morphology evolution and critical dose N_c (minimal dose of deposited atoms necessary for pore sealing) dependencies on growth conditions and porous surface morphology were examined. Other reports^{225,226} deal with porous (001) surfaces. The results presented below are obtained using a 3D MC simulation where pore sealing during epitaxial growth on {111} and {001} diamond-like surfaces are investigated.

Ignoring the SOS principle one can simulate a 3D surface layer with deep pores. This surface layer is considered as a perfect 3D crystal that is described by cyclic boundary conditions. The volume of the model surface layer can contain up to 10^7 atomic sites. The algorithm excludes “void events” (when nothing happens) to speed up the simulations.

Surface diffusion is described using diffusion activation energies. The main event in the model is a diffusion hop, where an atom hops to an empty lattice site in any direction in the first, second, or third coordination sphere. For an atom in state p with n first and k second neighbors ($0 < n \leq 4$ and $0 < k \leq 12$) the probability W_{pq} of transition from a state p to a state q is determined by the energy E_{pq}

$$W_{pq} = e^{-(E_{pq}/kT)}, \quad (41)$$

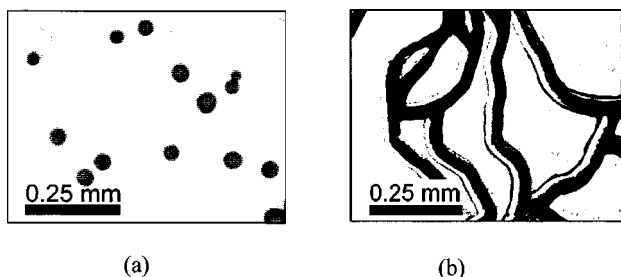


FIG. 66. An organic polymer low- k film capped with barrier after exposure to toluene (optical microscope pictures). Toluene captured beneath the barrier appears in black. Pinholes (a) or cracks (b) in the barrier are made visible (see Ref. 215).

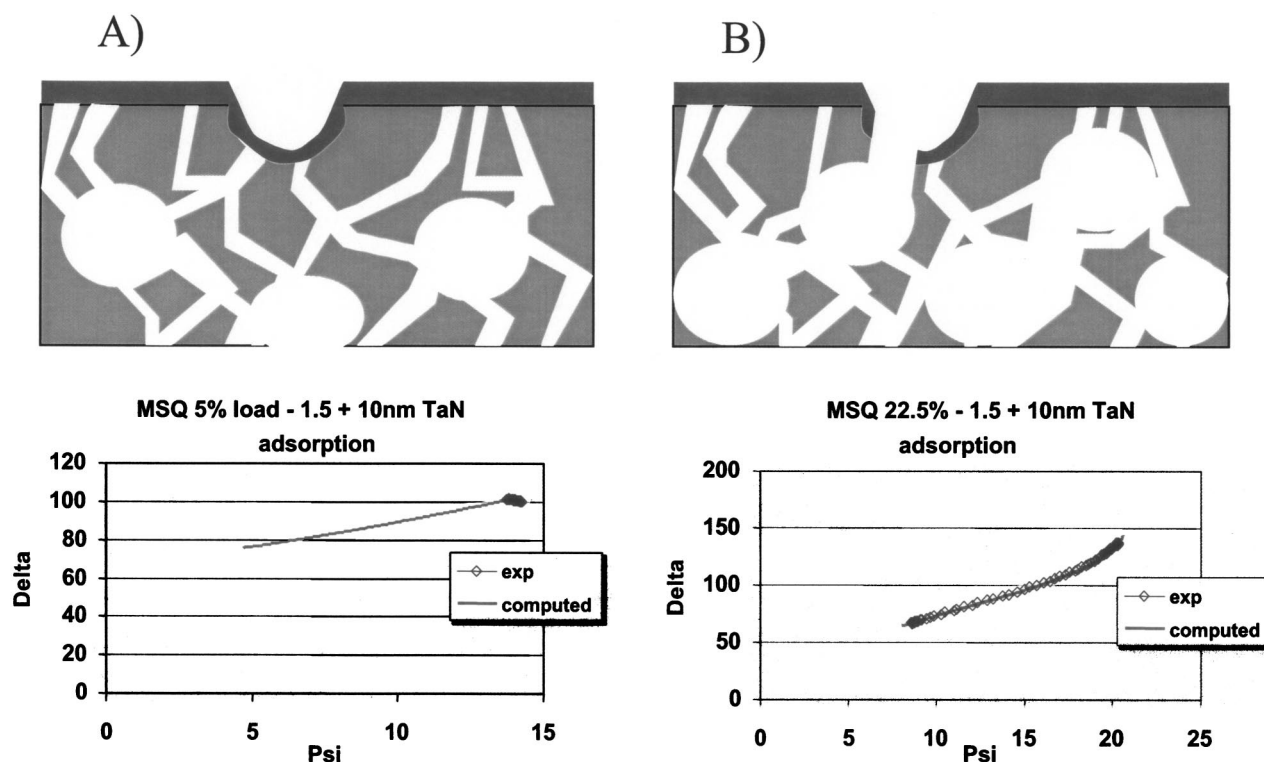


FIG. 67. Scheme of the coverage of a thin PVD cap layer on top of subtractive MSQ-based films with: (A) 5% and (B) 22.5% porogen load. Sacrificial nanoparticles (porogens) generate mesopores connected by the original microporosity of the matrix MSQ material. The mesopores appearing at the surface can be conformally covered by a thin PVD deposition (A). When the porogen load of the films is increased (B), part of this closed pore structure can be converted into an “open” one (with necking comparable to the pore size): these pores can only be sealed by “bridging” them with a thicker cap layer (see Ref. 149).

$$E_{pq} = nE_1 + kE_2 + E_3, \quad (42)$$

where the input parameters of the model E_1 , E_2 are interaction energies of the atom with its first and second neighbors. These two energies determine the detachment energy from the state p . Energy E_3 governs the probability of incorporation into state q .

For the simulation, it is necessary to fix the bonding energy of atoms with the silicon surface, which determines the activation energy of surface diffusion. This value is known only approximately for silicon surfaces and is in the range of 0.75–1.3 eV.^{228–230} The following values were taken for the simulations: $E_1 = 1$ eV, $E_2 = 0.0$ eV, and $E_3 = 0.0$ eV. The simulations were carried out for substrate and growth conditions in accordance with experimental works.^{231,232} Cylindrical pores were taken to be perpendicular to the surface with a density of approximately 10^{11} – 10^{12} cm⁻². The pore diameters were varied from 2.7 to 20 nm (7–50 Si atomic sites), and pore depths were 30 nm with a deposition rate $V = 0$ –10 ML/s. Annealing was simulated by setting the deposition rate equal to zero. The main output of the simulation is the minimal required thickness of the deposited film needed to seal all pores. This minimal thickness can be expressed as a critical dose N_c or in an equivalent number of ML.

Essential differences were found in pore sealing during an epitaxial process on (111) and (001) surfaces. The Si(111) surface remains flat during and after pore sealing as shown in Fig. 68(a). This morphology exists due to the high diffusivity along the (111) surface, as the activation energy of diffusion

hop along this surface of a diamond-like crystal is determined by only one bond, while two bonds are involved on the pore walls. In contrast to the epitaxy on a (111) porous surface, pores on an (001) surface cause surface relief formation during sealing [see Fig. 68(b)]. A pyramidal pit is created above the pore during epitaxy with basis sides parallel to the (011) surface and lateral facets to the (111) surface because diffusivity along the (001) surface (substrate and pore walls) is much lower than along the (111) surface. However, such relief is unique for (001) surfaces and irrelevant for amorphous low- k materials. Pore sealing on the Si(111) surface is more similar to pore sealing on amorphous low- k materials. For such growth on the (111) surface two regimes can be defined:

regime I: islands are formed between pores until a solid layer is created over the pore,

regime II: islands between pores are nucleated simultaneously with pore sealing. The latter regime is illustrated by Fig. 68(a).

It was found that there are optimal deposition conditions at which the sealing thickness (or critical dose N_c) is minimized. A minimum in N_c versus deposition rate for two pore diameters (5 and 10 nm) is seen in Fig. 69(a). At low deposition rates growth regime I (no islands until pores are sealed) takes place and at high ones regime II (islands formed during pore sealing). The slight increase of the critical dose at low deposition rate is due to deeper penetration of the deposited material along the pore walls. Figure 69(b) demonstrates pore cross sections for three deposition rates: to

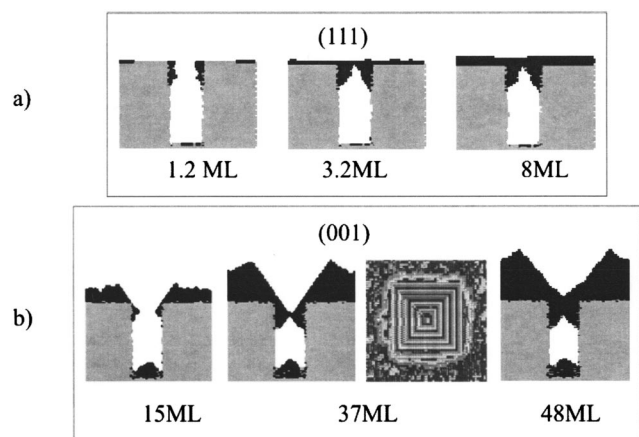


FIG. 68. Simulated pore cross sections after deposition of shown doses on: (a) (111) Si surface and (b) (001) Si surface ($T=800$ K, $V=2$ ML/s, $d=50$ atomic sites).

the left of the minimum in curve 1 of Fig. 69(a), in the minimum, and to the right of it. A clear minimum of the critical dose is also seen in the temperature dependence [see Fig. 69(c)]. The falling portion of the curve at low temperatures corresponds to regime II. A plateau at higher temperatures corresponds to regime I. The minimum corresponds to the situation where diffusion along the substrate surface becomes more substantial than along pore walls. An atom falling into the pore mouth has no time for a diffusion hop because the next one coming from the surface binds with it. At higher temperatures, an increase in the critical dose is associated with active diffusion of substrate atoms deep into the pore. Nucleation processes of islands on the surfaces of substrate and pore walls are determined by the ratio D/V , (where D is diffusion coefficient and V is deposition rate), and not by each of these values separately.²³³ Therefore with increasing deposition rate the entire curve is shifted to higher temperatures. In Fig. 70 one can see a variation of the mouth pore size during pore sealing for two pore diameters at different deposition rates. A lower deposition rate leads to faster pore sealing due to surface diffusion.

It was found that the growth mechanism (regime I or II) determines the critical dose dependence on the substrate's porous structure. In Fig. 71(a) the critical dose dependencies

on porosity have minima when the growth regime is changed. Critical dose N_c versus pore size dependencies are changed from linear to quadratic when the growth mode is changed [Fig. 71(b)].

Although the model is rigorously a lattice model, simulation results could be useful for amorphous porous low- k materials. For materials of different chemical nature this difference can promote or prevent pore sealing. If surface diffusion takes place, adsorbate microcrystallization on an amorphous porous surface might be possible. Using crystal surfaces with two different orientations, one can see how diffusion processes influence pore sealing while simulation results cannot be used for direct comparison with experimental data for amorphous low- k structures. However they illustrate tendencies of surface morphology evolution during deposition processes for different parameters of substrate porosity and growth conditions.

Recent experimental results for pore sealing on low- k dielectrics²³⁴ demonstrate the possibility of thin solid layer formation over pores with low roughness. This highlights the essential role of surface diffusion and indicates higher adatom diffusion between pores, than along pores. Such a picture is similar to the model results obtained on the porous (111) surface. By changing the surface diffusion of different atoms one can simulate the complex chemical nature of low- k materials and sealing films. Such simulations can be useful in the search for conditions for creating a sealing layer as thin and smooth as possible on a porous substrate.

4. Pore sealing by plasma surface interaction

In most cases both chemical and physical action of plasmas lead to a densification of the low- k dielectric. The densification, with appropriate choice of plasma power, can be confined into a few nm of the top layers of constitutive (microporous) dielectric films.²³⁵ This way, the k value of the films is not significantly affected; this newly formed densified "skin" layer can even be beneficial, since it acts as a protection or barrier to further damage in the bulk of the film.^{235,236} This is not true for mesoporous dielectric films, which are extremely sensitive to diffusion of reactive species. In general, effects of plasma treatments can easily attain several hundreds of nm depth in such dielectrics, due to their

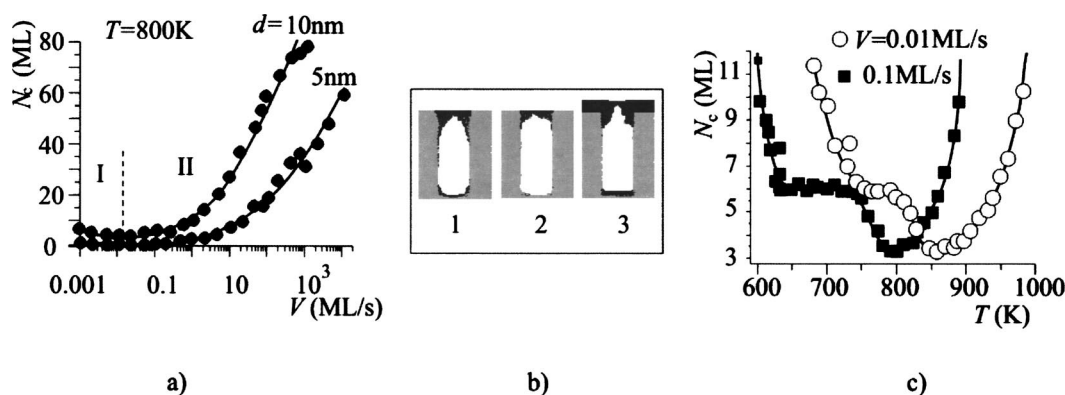


FIG. 69. Critical dose dependencies on growth conditions for the (111) surface: (a) N_c vs deposition rate V ; (b) pore cross-section ($d=10$ nm, $h=25$ nm) at the moment of pore sealing for different V : (1) -0.001 ML/s, (2) -0.1 ML/s, (3) -10 ML/s; (c) N_c vs T , ($d=10$ nm).

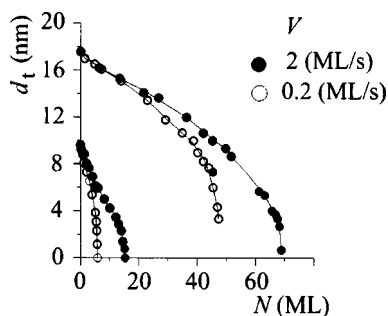


FIG. 70. Dependence of pore mouth diameter d_t on deposited dose N for two values of initial pore diameter [$T=800$ K, (111) surface].

high porosity/low density.²³⁶ It is expected that the extent of this modification would show a difference between mesoporous materials with meso- and microconnections, but so far no data are available showing such a comparison.

In the case of organic polymers, the quality of the WCN barrier obtained by ALD on an organic polymer film is reported to be dependent on surface treatment.

5. Pore sealing by surface cross linking/reconstruction

It is possible to identify a correlation between the carbon content at the dielectric surface on the one hand, and sealing by PVD Ta(N) on the other hand.²³⁴ The deposition of a 10 nm Ta(N) on a mesoporous MSQ-based film with 24% C concentration yields a fully closed cap layer, while an equivalent Ta(N) film on a MSQ dielectric with equivalent pore size and porosity but lower C concentration of about 18% has a higher sheet resistance and remains still porous. Moreover, 10 nm of Ta(N) is efficient in sealing a HSQ-based mesoporous film precapped by 10 nm SiC:H. When depositing either only Ta(N) or only α -SiC:H on such a film, about 30 nm capping thickness is needed to achieve complete sealing.^{212,216} These examples indicate that a higher C concentration in the dielectric composition enhances sealing efficiency.²³⁴

In order to explain the beneficial influence from the presence of surface C on pore sealing, the following mechanism is proposed. The tendency of sputtered Ta atoms to react with C at the surface of the dielectric can lead to the formation of Ta-C.²³⁷ Thus, the wetting capability of Ta(N) on the dielectric surface is enhanced and a structural rearrangement of the

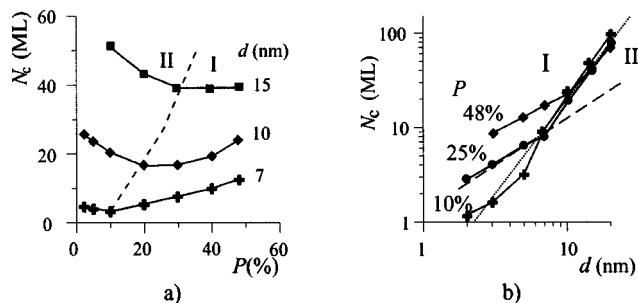


FIG. 71. Critical dose dependencies N_c on parameters of a porous (111) surface: (a) on porosity P and (b) on pore diameter d : (dashed line) $N_c \sim d$, (dotted line) $N_c \sim d^2$.

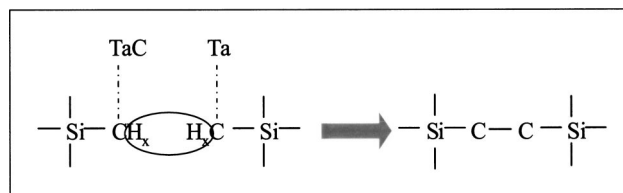


FIG. 72. Mechanism leading to a local reconstruction of dielectric matrices containing CH_x functional groups: the presence of TaC crystallites or unreacted Ta, together with the high temperature and ion bombardment from the PVD deposition lead to the weakening and eventually the break of C-H bonds. Cross-linking between two neighboring polymer chains can take place (Ref. 234).

bonds/charges takes place in the top layers of the dielectric matrix. At the interface between the dielectric and the Ta(N) film, a “transition layer” with high intermixing is formed. A considerable amount of Ta atoms are dispersed in the initial matrix (α -SiC:H or siloxane for the examples mentioned earlier), either unreacted or in the form of Ta-C crystallites. Under these conditions, as already reported by Gerstenberg and Grischke,²³⁸ the pristine carbidic bonds in the dielectric matrices (mainly C- H_x like, since the covalent Si-C bonds are much stronger) are weakened, due to charge delocalization effects induced by the presence of neighboring metal atoms. Moreover, the high deposition temperature and the ion bombardment energy released during PVD deposition further favors the breaking of these bonds. This can lead to a local reconstruction by cross-linking of the top layers of the matrix through the formation of a C-C bond across the polymer chains, as shown schematically in Fig. 72.²³⁴

ACKNOWLEDGMENTS

The authors are very grateful to Dr. M. Van Rossum, Dr. T. Abell (Intel), Dr. C. Whelan, Dr. T. Le Quoc, and Dr. D. Gravesteijn (Philips) for reviewing and correcting the manuscript. The authors would like to thank the many colleagues working in low- k dielectrics from the SPDT division within IMEC.

APPENDIX: GLOSSARY (TERMS AND ABBREVIATIONS)

1MS	monomethylsilane
2MS	di-methylsilane
3MS	three-methylsilane
4MS	tetra-methylsilane
AFM	atomic force microscopy
ALD	atomic layer deposition
APIMS	atmospheric pressure ionization mass spectrometer
BET	Brunauer, Emmet and Teller (authors)
BJH	Barrett, Joyner, and Halenda (authors)
CMP	chemical mechanical polishing
Constitutive porosity	porosity that depends on the original, as-deposited, arrangement of a material structure.
CSM	continuous stiffness measurement

CSN	cross-section nanoindentation
CTE	coefficient of thermal expansion
CVD	chemical vapor deposition
DUV	deep ultraViolet
EELS	electron energy loss spectroscopy
EFTEM	energy filtered transmission electron microscopy
EP	ellipsometric porosimetry
ERD	elastic recoil detection
HRTEM	high resolution transmission electron microscopy
HSQ	hydrogensilsesquioxane
ITRS	International Technology Roadmap for Semiconductors
IUPAC	International Union of Pure and Applied Chemistry
m-ELT	modified edge liftoff test
Mesopores	Pores with diameter between 2 and 50 nm (IUPAC classification)
Micropores	Pores with diameter less than 2 nm (IUPAC classification)
MIM	metal–insulator–metal
MIS	metal–insulator–Semiconductor (Si)
MSQ	methylsilsesquioxane
NMR	nuclear magnetic resonance
PALS	positron annihilation lifetime spectroscopy
PAS	positron annihilation spectroscopy
PECVD	plasma enhanced chemical vapor deposition
Porosity	the fraction p of the total volume of the film which is attributed to the pores: $p = V_p/V$, where V_p is pore volume and V is total volume of the film.
PVD	physical vapor deposition
QCM	quartz crystal microbalance
RBS	Rutherford backscattering
RGA	residual gas analyzer (mass spectrometer)
RIE	reactive ion etching
SANS	small angle neutron scattering
SAW(S)	surface acoustic wave (spectroscopy)
SAXS	small angle x-ray scattering
SBS	surface Brillouin scattering
SE	spectroscopic ellipsometry
SEM	scanning electron microscopy
SS4PB	sandwich structure 4 point bending
SSQ	silsesquioxane
STM	scanning tunneling microscopy
Subtractive porosity	porosity created by selective removal of certain parts of the original material structure
TDS	thermodesorption spectra
TEOS	tetra-ethyl-ortho-silicate
TOF-SIMS	time-of-flight secondary ions mass spectrometry
XPS	x-ray photoemission spectroscopy
XRR	x-ray reflectivity

TABLE VI. Classification of available low- k materials.^a

k value	Organic polymers	SSQ based	Silica based
$k = 4.2$	SiO ₂
$3.0 \leq k \leq 4.0$...	FOX ^{TMb}	Fluorinated silica (SiOF) ^c
$2.4 \leq k < 3.0$	FLARE ^{TMd}	HOSP ^{TMd}	Aurora ^{TMg}
	BCB ^e	...	Coral ^{TMh}
	SiLK ^{TMf}	...	Z3MS ^{TMb}
	Black diamond ^{TMi}
$2.0 \leq k < 2.4$	Porous SiLK ^{TMf}	IPST ^{TMk}	Orion ^{TMn}
	PTFE ^j	LKD ^{TMl}	Nanoglass ^{TMd}
	...	XLK ^{TMb}	...
	...	Zirkon ^{TMm}	...
$k < 2.0$	Aerogel ^o
	Xerogel ^p

^aIf several versions of a material are available then the lowest k -value version is included in the table.

^bSee Ref. 239.

^jSee Ref. 247.

^cSee Ref. 240.

^kSee Ref. 248.

^dSee Ref. 241.

^lSee Ref. 249.

^eSee Ref. 242.

^mSee Ref. 250.

^fSee Ref. 243.

ⁿSee Ref. 251.

^gSee Ref. 244.

^oSee Ref. 252.

^hSee Ref. 245.

^pSee Ref. 253.

ⁱSee Ref. 246.

¹R. H. Havemann and J. A. Hutchby, Proc. IEEE **89**, 586 (2001).

²K. Maex, E. Beyne, F. Catthoor, H. Corporaal, and H. de Man, European Semiconductor, 2002.

³International Technology Roadmap for Semiconductors (2001).

⁴Proceedings of the International Interconnect Technology Conferences (IITC) (IEEE) and of the Advanced Metallization Conference (AMC) (MRS).

⁵J. D. Livingston, *Electronic Properties of Engineering Materials* (Wiley, New York, 1999), Chap. 4.

⁶P. W. Atkins, *Physical Chemistry*, 5th ed. (Oxford University Press, New York, 1994).

⁷R. P. Feynman, R. B. Leighton, and M. Sands, in *The Feynman Lectures on Physics* (Adison Wesley, Reading, PA, 1966), Chap. 11.

⁸P. W. Atkins and R. S. Friedman, *Molecular Quantum Mechanics*, 3rd ed. (Oxford University Press, New York, 1997), Chap. 16.

⁹L. W. Hrubesh, L. E. Keene, and V. R. Latorre, J. Mater. Res. **8**, 1736 (1993).

¹⁰J. Rouquerol, D. Avnir, C. W. Fairbridge, D. H. Everett, J. H. Haynes, N. Pernicone, J. D. F. Ramsay, K. S. W. Sing, and K. K. Unger, Pure Appl. Chem. **66**, 1739 (1994).

¹¹G. L. Link, in *Polymer Science*, edited by A. D. Jenkins (1972), p. 1283.

¹²N. P. Hacker, MRS Bull. **22**, 33 (1997).

¹³R. J. Gutmann, W. N. Gill, T. M. Lu, J. F. McDonald, S. P. Murarka, and E. J. Rymaszewski, *Advanced Metallization Conference in 1996* (Materials Research Society, Pittsburgh, PA, 1997).

¹⁴E. T. Ryan, A. J. McKerrow, J. Leu, and P. S. Ho, MRS Bull. **22**, 49 (1997).

¹⁵A. Grill, Diamond Relat. Mater. **10**, 234 (2001).

¹⁶A. Grill, Thin Solid Films **356**, 189 (1999).

¹⁷H. Yang, D. J. Tweet, Y. Ma, and T. Nguen, Appl. Phys. Lett. **73**, 1514 (1998).

¹⁸J. W. Yi, Y. H. Lee, and B. Farouk, Thin Solid Films **374**, 103 (2000).

¹⁹T. W. Mountsier and J. A. Samuels, Thin Solid Films **332**, 362 (1998).

²⁰C. J. Brinker and G. W. Scherer, *Sol–Gel Science: The Physics and Chemistry of Sol–Gel Processing* (1990).

²¹T. Ramos, K. Roderick, A. Mascara, and D. M. Smith, “Processings of Advanced Metallization Conferences (AMC)” Advanced Metallization and Interconnect Systems for ULSI Applications, 1996, p. 455.

²²C. Jin, J. D. Luttmer, D. M. Smith, and T. A. Ramos, MRS Bull. **22**, 39 (1997).

- ²³ K. Chung, E. S. Moyer, and M. Spaulding, U.S. Patent No. 6,231,989 (2001); E. S. Moyer, K. Chung, M. Spaulding, T. Deis, R. Boisvert, C. Saha, and J. Bremmer, Proceedings of IITC, 1999.
- ²⁴ M. R. Baklanov, E. Kondoh, E. K. Lin, D. W. Gidley, H.-J. Lee, K. P. Mogilnikov, and J. N. Sun, Proceedings of IITC'2001, San Francisco, CA, 2001, pp. 189–191.
- ²⁵ F. Schueth and W. Schmidt, Adv. Mater. **14**, 629 (2002).
- ²⁶ S. Mintova, N. H. Olson, V. Valtchev, and T. Bein, Science **283**, 958 (1999).
- ²⁷ M. E. Davis, Nature (London) **417**, 813 (2002).
- ²⁸ Y. Fan, H. R. Bentley, K. R. Kathan, P. Clem, Y. F. Lu, and C. J. Brinker, J. Non-Cryst. Solids **285**, 79 (2001).
- ²⁹ C. J. Brinker, R. Sehgal, S. L. Hietala, R. Deshpande, D. M. Smith, D. Loy, and C. S. Ashley, J. Membr. Sci. **94**, 85 (1994).
- ³⁰ S. Baskaran, J. Liu, K. Domansky, N. Kohler, X. Li, C. Coyle, G. E. Fryxell, S. Thevuthasan, and R. E. Williford, Adv. Mater. **12**, 291 (2000).
- ³¹ F. K. de Theije, A. Balkenende, K. Kriege, M. Verheijen, and D. Gravest-eijn, presented at the Sematech Workshop, San Francisco, June 2002.
- ³² Y. F. Lu, G. Z. Cao, R. P. Kale, S. Prabakar, G. P. Lopez, and C. J. Brinker, Chem. Mater. **11**, 1223 (1999).
- ³³ M. R. Baklanov et al., Proceedings of the Advanced Metallization Conference (Materials Research Society, Pittsburgh, PA, 2002).
- ³⁴ M. Petkov, M. H. Weber, K. G. Lynn, and K. P. Rodbell, Appl. Phys. Lett. **79**, 3884 (2001).
- ³⁵ J. L. Hendrick, R. D. Miller, C. J. Hawker, K. R. Carter, W. Volksen, D. Y. Yoon, and M. Trollsas, Adv. Mater. **10**, 1049 (1998).
- ³⁶ M. Gallagher, N. Pugliano, J. Calvert, Y. You, R. Gore, N. Annan, M. Talley, S. Ibbitson, and A. Lamola, Presented at the MRS Spring Meeting, 2001.
- ³⁷ K. Chung and S. Zhang, U.S. Patent No. 6,313,045 (2001); B. Zhong et al., Presented at the MRS Spring Meeting, 2002.
- ³⁸ S. Wolf and R. N. Tauber, Silicon Processing for the VLSI Era, Process Technology, Vol. 1, 2nd ed. (Lattice, CA, 2000).
- ³⁹ A. C. Adams, Dielectric and Polysilicon Film Deposition, in VLSI Technology, edited by S. H. Sze (McGraw-Hill, New York, 1983), Chap. 3, p. 93.
- ⁴⁰ S. Sivaram, Chemical Vapor Deposition (McGraw-Hill, New York, 1995).
- ⁴¹ H. J. Emelius and K. Stewart, J. Chem. Soc. 1182 (1935).
- ⁴² P. S. Shantarovitz, Acta Physicochim. **6**, 65 (1937).
- ⁴³ M. R. Baklanov and L. L. Vasilyeva, Mater. Sci. Forum **185–188**, 65 (1995).
- ⁴⁴ M. R. Baklanov, L. L. Vasilyeva, T. A. Gavrilova, F. N. Dultsev, K. P. Mogilnikov, and L. A. Nenasheva, Thin Solid Films **171**, 43 (1989).
- ⁴⁵ F. N. Dultsev, L. A. Nenasheva, and L. L. Vasilyeva, J. Electrochem. Soc. **145**, 2569 (1998).
- ⁴⁶ V. N. Kondratiev, in Comprehensive Chemical Kinetics, The Theory of Kinetics, Vol. 2, edited by C. H. Bamford and C. F. H. Tipper (Elsevier, New York, 1969), pp. 81–188.
- ⁴⁷ H. Yasuda, Plasma Polymerization (Academic, New York, 1985).
- ⁴⁸ T. Homma, Mater. Sci. Eng., R. **23**, 6.243 (1998).
- ⁴⁹ T. Usami, K. Shimokawa, and M. Yoshimura, Jpn. J. Appl. Phys., Part 1 **33**, 408 (1994).
- ⁵⁰ B. K. Hwang, J. H. Choi, S. Lee, K. Fujihara, U. I. Chung, and S. I. Lee, Jpn. J. Appl. Phys., Part 1 **35**, 1588 (1996).
- ⁵¹ W. S. Yoo, R. Swope, and D. Mordo, Jpn. J. Appl. Phys., Part 1 **36**, 267 (1997).
- ⁵² S. M. Lee, M. Park, K. C. Park, J. T. Bark, and J. Jang, Jpn. J. Appl. Phys., Part 1 **35**, 1579 (1996).
- ⁵³ S. W. Lim, Y. Shimogaki, Y. Nakano, K. Tada, and H. Komiyama, Jpn. J. Appl. Phys., Part 1 **35**, 1583 (1996).
- ⁵⁴ T. Homma, R. Yamaguchi, and Y. Murao, J. Electrochem. Soc. **140**, 3599 (1993).
- ⁵⁵ T. Homma, J. Electrochem. Soc. **143**, 1084 (1996).
- ⁵⁶ A. Grill, D. Edelstein, and V. Patel, Advanced Metallization Conference 2001 (Material Research Society, Pittsburgh, PA, 2002).
- ⁵⁷ A. Grill, V. Patel, K. P. Rodbell, E. Huang, S. Christiansen, and M. R. Baklanov, Presented at the Spring Materials Research Society, 2002.
- ⁵⁸ M. Loboda, J. A. Seifferly, C. M. Grove, and R. F. Schneider, Mater. Res. Soc. Symp. Proc. **447**, 145 (1997).
- ⁵⁹ M. J. Loboda, Microelectron. Eng. **50**, 15 (2000).
- ⁶⁰ J. M. Park and S. W. Rhee, J. Electrochem. Soc. **149**, F92 (2002).
- ⁶¹ D. Shamiryan, K. Weidner, W. D. Gray, M. R. Baklanov, S. Vanhaele-meersch, and K. Maex, Presented at European workshop “Material for Advanced Metallization” 2002 Vaals, The Netherlands (to be published in Microelectron. Eng.).
- ⁶² H. G. P. Lewis, D. J. Edell, and K. Gleason, Chem. Mater. **12**, 3488 (2000).
- ⁶³ Q. Wu and K. Gleason, J. Vac. Sci. Technol. A **21**, 388 (2003).
- ⁶⁴ A. Grill, Thin Solid Films **398–399**, 527 (2001).
- ⁶⁵ A. Grill and V. Patel, Appl. Phys. Lett. **79**, 803 (2001).
- ⁶⁶ K. Buchanan, K. Beekmann, K. Giles, J.-C. Yeoh, and H. Donohue, Advanced Metallization Conference, Montreal, Canada, 2001.
- ⁶⁷ D. Shamiryan, M. R. Baklanov, S. Vanhaelemeersch, and K. Maex, Electrochem. Solid-State Lett. **4**, F3 (2001).
- ⁶⁸ D. Shamiryan, M. R. Baklanov, S. Vanhaelemeersch, and K. Maex (unpublished).
- ⁶⁹ M. L. Green, E. P. Gusev, R. Degraeve, and E. L. Garfunkel, J. Appl. Phys. **90**, 2057 (2001).
- ⁷⁰ R. F. Egerton, Electron Energy-Loss Spectroscopy in the Electron Microscope (Plenum, New York, 1996).
- ⁷¹ D. B. Williams and C. B. Carter, Transmission Electron Microscopy: A Text Book of Materials Science (Plenum, New York, 1996), Vols. 1–4.
- ⁷² S. Hens, Ph.D. thesis, University of Antwerp, Belgium, 2002.
- ⁷³ S. Hens, R. A. Donaton, K. Maex, S. Vanhaelemeersch, and J. Van Landuyt, Inst. Phys. Conf. Ser. **169**, 415 (2001).
- ⁷⁴ G. Englehardt and D. Michel, High Resolution Solid State NMR of Silicates and Zeolites (Wiley, New York, 1987).
- ⁷⁵ E. A. Williams, in Annual Reports on NMR Spectroscopy, edited by G. A. Webb (Academic, London, 1983).
- ⁷⁶ M. Stucchi and K. Maex, IEEE Trans. Instrum. Meas. **51**, 537 (2002).
- ⁷⁷ Raphael User's Manual (Technology Modeling Associates, 1995).
- ⁷⁸ A. Julbe and J. D. F. Ramsay, in Fundamentals of Inorganic Membrane Science and Technology, edited by A. J. Burggraaf and L. Cot (Elsevier Science B.V., New York, 1996), Chap. 4, p. 67.
- ⁷⁹ J. D. F. Ramsay, MRS Bull. **24**, 36 (1999).
- ⁸⁰ D. W. Gidley, W. E. Frieze, T. L. Dull, J. N. Sun, A. F. Yee, C. V. Nguyen, and D. Y. Yoon, Appl. Phys. Lett. **76**, 1282 (2000).
- ⁸¹ M. P. Petkov, M. H. Weber, K. G. Lynn, K. P. Rodbell, and S. A. Cohen, Appl. Phys. Lett. **74**, 2546 (1999).
- ⁸² W. Wu, W. E. Wallace, E. Lin, G. W. Lynn, C. J. Glinka, R. T. Ryan, and H. Ho, J. Appl. Phys. **87**, 1193 (2000).
- ⁸³ S. Kawamura, T. Ohta, K. Omote, Y. Ito, R. Suzuki, and T. Ohdara, Proceeding IITC'2001, San Francisco, CA, 2001, pp. 195–197.
- ⁸⁴ F. N. Dultsev and M. R. Baklanov, Electrochem. Solid-State Lett. **2**, 192 (1999).
- ⁸⁵ M. R. Baklanov, K. P. Mogilnikov, V. G. Polovinkin, and F. N. Dultsev, J. Vac. Sci. Technol. B **18**, 1385 (2000).
- ⁸⁶ M. R. Baklanov and K. P. Mogilnikov, Opt. Appl. **30**, 491 (2000).
- ⁸⁷ C. Wongmanerod, S. Zangoie, and H. Arwin, Appl. Surf. Sci. **172**, 117 (2001).
- ⁸⁸ E. Kondoh, M. R. Baklanov, E. Lin, D. Gidley, and A. Nakashima, Jpn. J. Appl. Phys., Part 2 **40**, L323 (2001).
- ⁸⁹ D. W. Gidley, W. E. Frieze, T. L. Dull, J. N. Sun, and A. F. Yee, Mater. Res. Soc. Symp. Proc. **612**, D4.3.1 (2000).
- ⁹⁰ J.-N. Sun, D. W. Gidley, T. L. Dull, W. E. Frieze, A. F. Yee, E. T. Ryan, S. Lin, and J. Wetzel, J. Appl. Phys. **89**, 5138 (2001).
- ⁹¹ S. J. Gregg and S. W. Sing, Adsorption, Surface Area and Porosity, 2nd ed. (Academic, New York, 1982).
- ⁹² M. R. Baklanov and K. P. Mogilnikov, Mater. Res. Soc. Symp. Proc. **612**, D4.2.1 (2000).
- ⁹³ M. R. Baklanov and K. P. Mogilnikov, Microelectron. Eng. **64**, 335 (2002).
- ⁹⁴ M. M. Dubinin and L. V. Radushkevich, Proc. Acad. Sci. **55**, 331 (1947).
- ⁹⁵ G. Horvath and K. Kawazoe, J. Chem. Eng. Jpn. **16**, 470 (1983).
- ⁹⁶ A. Saito and H. C. Foley, AIChE J. **37**, 429 (1991).
- ⁹⁷ A. P. Karnaukhov, Adsorption: Texture of Dispersed and Porous Materials (Nauka, Novosibirsk, 1999).
- ⁹⁸ Y. Spooner, presented at the 1999 Sematech Workshop, Orlando, FL, 1999.
- ⁹⁹ B. J. Bauer, H.-J. Lee, C. Soles, R. C. Hedden, D.-W. Liu, W.-L. Wu, J. A. Lee, and J. Wetzel, presented at the Spring MRS Conference, 2002.
- ¹⁰⁰ The polarizability volume α' (m^3) equals $\alpha/4\pi\epsilon_0$ with α the polarizability ($\text{C}^2\text{J}^{-1}\text{m}^{-1}$).

- ¹⁰¹ C. M. Flannery and M. R. Baklanov, Proceedings of the International Interconnect Technology Conference (IITC 2002), 2002, p. 233.
- ¹⁰² J. Malzbender, J. M. J. den Toonder, A. R. Balkenende, and G. de With, *Mater. Sci. Eng.*, **R. 36**, 47 (2002).
- ¹⁰³ M. R. VanLandingham, J. S. Villarrubia, W. F. Guthrie, and G. F. Meyers, *Macromol. Symp.* **167**, 15 (2001).
- ¹⁰⁴ S. H. Brongersma, 3rd Symposium on Nano-mechanical Testing (submitted).
- ¹⁰⁵ G. W. Farnell and E. L. Adler, *Physical Acoustics*, edited by W. P. Mason and R. N. Thurston (Academic, New York and London, 1972), Vol. IX, p. 35.
- ¹⁰⁶ D. Nelsen, M. Gostein, and A. Maznev, Proceeding of Symposium on Polymers for Microelectronics, Wilmington, DE, 2000.
- ¹⁰⁷ G. Carlotti, L. Doucet, and M. Dupeux, *J. Vac. Sci. Technol. B* **14**, 3460 (1996).
- ¹⁰⁸ B. Hillebrands, *Rev. Sci. Instrum.* **70**, 1589 (1999).
- ¹⁰⁹ K. P. Mogilnikov and M. R. Baklanov, *Electrochem. Solid-State Lett.* **5**, F29 (2002).
- ¹¹⁰ D. S. Campbell, in *Handbook of Thin Film Technology*, edited by L. I. Maissel and R. Glang (McGraw-Hill, New York), p. 6B-1.
- ¹¹¹ R. Jacobsson, *Thin Solid Films* **34**, 191 (1976).
- ¹¹² P. Bodo and J.-E. Sundgren, *J. Appl. Phys.* **60**, 1161 (1986).
- ¹¹³ R. L. Loh, C. Rossington, and A. G. Evans, *J. Am. Ceram. Soc.* **69**, 139 (1989).
- ¹¹⁴ A. J. Perry, *Surf. Eng.* **3**, 183 (1986).
- ¹¹⁵ P. R. Chalker, S. J. Bull, and D. S. Rickerby, *Mater. Sci. Eng.*, **A 140**, 583 (1991).
- ¹¹⁶ Q. Ma, H. Fujimoto, P. Flinn, V. Jain, F. Adibi-Rizi, F. Moghadam, and R. H. Dauskardt, *Mater. Res. Soc. Symp. Proc.* **391**, 91 (1995).
- ¹¹⁷ E. O. Shaffer II, Ph.D. thesis, Massachusetts Institute of Technology, 1995.
- ¹¹⁸ E. O. Shaffer, F. J. McGarry, and L. Hoang, *Polym. Eng. Sci.* **36**, 18 (1996).
- ¹¹⁹ J. M. Sanchez *et al.*, *Acta Mater.* **47**, 4405 (1999).
- ¹²⁰ Z. Suo and J. W. Hutchinson, *Mater. Sci. Eng.*, **A 107**, 135 (1989).
- ¹²¹ P. G. Charalambides, J. Lund, A. G. Evans, and R. M. McMeeking, *J. Appl. Mech.* **111**, 77 (1989).
- ¹²² R. M. Cannon, B. J. Dalgleish, R. H. Dauskardt, R. M. Fisher, T. S. Oh, and R. O. Ritchie, in *Fatigue of Advanced Materials*, edited by R. O. Ritchie, R. H. Dauskardt, and B. N. Cox (MECP Publishing Ltd., Edgbaston, U.K., 1991), pp. 459–482.
- ¹²³ M. Lane and R. H. Dauskardt, *J. Mater. Res.* **15**, 2758 (2000).
- ¹²⁴ S. H. Lau, E. Tolentino, Y. Lim, E. Tolentino, and A. Koo, *J. Electron. Mater.* **30**, 299 (2001).
- ¹²⁵ M. J. Loboda, C. M. Grove, and R. F. Schneider, *J. Electrochem. Soc.* **145**, 2861 (1998).
- ¹²⁶ J. N. Bremmer, Y. Liu, K. G. Gruszynski, and F. C. Dall, *Mater. Res. Soc. Symp. Proc.* **476**, 37 (1997).
- ¹²⁷ M. G. Albrecht and C. Blanchette, *J. Electrochem. Soc.* **145**, 4019 (1998).
- ¹²⁸ V. Belot, R. Corriu, D. Leclercq, P. H. Mutin, and A. Vioux, *Chem. Mater.* **3**, 127 (1991).
- ¹²⁹ U. Kreissig, S. Grigull, K. Lange, P. Nitzsche, and B. Schmidt, *Nucl. Instrum. Methods Phys. Res. B* **138**, 674 (1998).
- ¹³⁰ M. Morgen, E. T. Ryan, J. H. Zhao, C. Hu, T. H. Cho, and P. S. Ho, *Annu. Rev. Mater. Sci.* **30**, 645 (2000).
- ¹³¹ Y. H. Kim, M. S. Hwang, H. J. Kim, J. Y. Kim, and Y. Lee, *J. Appl. Phys.* **90**, 3367 (2001).
- ¹³² F. Iacopi *et al.*, *Proceedings of Advanced Metallization Conference 2000* (Materials Research Society, Pittsburgh, PA, 2001), pp. 287–299.
- ¹³³ T. Furusawa, D. Ryazaki, R. Yoneyama, Y. Homma, and K. Hinode, *J. Electrochem. Soc.* **148**, F175 (2001).
- ¹³⁴ L. M. Han, J.-S. Pan, S.-M. Chen, N. Balasubramanian, J. Shi, L. S. Wong, and P. D. Foo, *J. Electrochem. Soc.* **148**, F148 (2001).
- ¹³⁵ Z.-C. Wu *et al.*, *J. Electrochem. Soc.* **148**, F127 (2001).
- ¹³⁶ Z.-C. Wu *et al.*, *J. Electrochem. Soc.* **148**, F115 (2001).
- ¹³⁷ S. Sugahara, T. Kadoya, K.-i. Usami, T. Hattori, and M. Matsumura, *J. Electrochem. Soc.* **148**, F120 (2001).
- ¹³⁸ S. Sugahara, K.-i. Usami, and M. Matsumura, *Jpn. J. Appl. Phys., Part 1* **38**, 1428 (1999).
- ¹³⁹ M. Loboda and G. Toskey, *Solid State Technol.* **41**, 99 (1998).
- ¹⁴⁰ J. Proost, E. Kondoh, G. Vereecke, M. Heyns, and K. Maex, *J. Vac. Sci. Technol. B* **16**, 2091 (1998).
- ¹⁴¹ J. Proost, M. Baklanov, K. Maex, and L. Delaey, *J. Vac. Sci. Technol. B* **18**, 303 (2000).
- ¹⁴² J. H. Zhao, I. Malik, E. T. Ryan, E. T. Ogawa, P. S. Ho, W. Y. Shih, A. J. McKerrow, and K. J. Taylor, *Appl. Phys. Lett.* **74**, 944 (1999).
- ¹⁴³ H. Miyajima, R. Katsumata, Y. Nakasaki, Y. Nishiyama, and N. Hayasaka, *Jpn. J. Appl. Phys., Part 1* **35**, 6217 (1996).
- ¹⁴⁴ H. Yang and G. Lucovsky, *J. Vac. Sci. Technol. A* **16**, 1525 (1998).
- ¹⁴⁵ S. J. Martin, J. P. Godschalx, M. E. Mills, E. O. Shaffer II, and P. H. Townsend, *Adv. Mater.* **12**, 1769 (2000).
- ¹⁴⁶ M. Fayolle, G. Passemard, M. Assous, D. Louis, A. Beverina, Y. Gobil, J. Cluzel, and L. Arnaud, *Microelectron. Eng.* **60**, 119 (2002).
- ¹⁴⁷ M. R. Baklanov, M. Muroyama, M. Judelewicz, E. Kondoh, H. Li, J. Waterloos, S. Vanhaelemeersch, and K. Maex, *J. Vac. Sci. Technol. B* **17**, 2136 (1999).
- ¹⁴⁸ F. Iacopi, Zs. Tokei, M. Stucchi, S. Brongersma, D. Vanhaeren, and K. Maex, *Microelectron. Eng.* **65**, 123 (2003).
- ¹⁴⁹ F. Iacopi *et al.*, *Microelectron. Eng.* **64**, 351 (2002).
- ¹⁵⁰ B. Zhong *et al.*, Presented at the MRS Spring Meeting, 2002.
- ¹⁵¹ A. Jain *et al.*, *Thin Solid Films* **398–399**, 513 (2001).
- ¹⁵² J. J. Waeterloos, Zs. Tokei, F. Iacopi, R. Caluwaerts, H. Struyf, I. Vos, and K. Maex, SEMATECH Workshop, San Francisco, CA, 2002.
- ¹⁵³ D. G. Cahill, H. E. Fisher, T. Klitsner, E. T. Swartz, and R. O. Pohl, *J. Vac. Sci. Technol. A* **7**, 1259 (1989).
- ¹⁵⁴ R. M. Costescu, A. J. Bullen, G. Matamis, K. E. O'Hara, and D. G. Cahill, *Phys. Rev. B* **65**, 094205 (2002).
- ¹⁵⁵ C. Hu, M. Morgen, P. S. Ho, A. Jain, W. N. Gill, J. L. Plawsky, and P. C. Wayner, Jr., *Appl. Phys. Lett.* **77**, 145 (2000).
- ¹⁵⁶ S. Hens, H. Bender, J. Van Landuyt, F. Iacopi, K. Weidner, and K. Maex, Joint Microscopy Meeting, Lille, France, June 2002, pp. 25–28.
- ¹⁵⁷ R. A. Donaton *et al.*, Proceedings of International Interconnects Technology Conference (IITC), 2000, pp. 93–95.
- ¹⁵⁸ Y. H. Kim, S.-K. Lee, and H. J. Kim, *J. Vac. Sci. Technol. A* **18**, 1216 (2000).
- ¹⁵⁹ Y. Uchida, T. Katoh, S. Sugahara, and M. Matsumura, *Jpn. J. Appl. Phys., Part 1* **39**, L1155 (2000).
- ¹⁶⁰ J. Cluzel, F. Mondon, Y. Loquet, Y. Morand, and G. Reimbold, *Microelectron. Reliab.* **40**, 675 (2000).
- ¹⁶¹ N. Aoi, T. Fukuda, and H. Yanazawa, Proceedings of IITC 2002, pp. 72–74.
- ¹⁶² Z. Hashin and S. Shtrikman, *J. Mech. Phys. Solids* **11**, 127 (1963).
- ¹⁶³ C. M. Flannery, T. Wittkowsky, K. Yung, B. Hillebrands, and M. R. Baklanov, *Appl. Phys. Lett.* **80**, 4594 (2002).
- ¹⁶⁴ J. N. Bremmer, *Solid State Technol. Suppl. S* **44**, S3–S6 (2001).
- ¹⁶⁵ T. Sherban, B. Sun, J. Blaine, C. Block, B. Jin, and E. Andideh, Proceedings of the International Interconnect Technology Conference (IITC 2001), pp. 257.
- ¹⁶⁶ S. Maitrejean, F. Fusalba, M. Patz, V. Jousseau, and T. Mourier, Proceedings of the International Interconnect Technology Conference 2002, p. 206.
- ¹⁶⁷ G. Kloster, T. Sherban, G. Xu, J. Blaine, B. Sun, and Y. Zhou, Proceedings of the International Interconnect Technology Conference, 2002, p. 242.
- ¹⁶⁸ D. A. Maidenberger, W. Volksen, R. D. Miller, and R. H. Dauskardt, Proceedings of the 7th International Conference on Polymers in Electronic Packaging, McAfee, N.J., October 18–20, 2000 (submitted).
- ¹⁶⁹ W. L. Wu and H. C. Liou, *Thin Solid Films* **312**, 73 (1998).
- ¹⁷⁰ P. H. Townsend *et al.*, *Mater. Res. Soc. Symp. Proc.* **476**, 9 (1997).
- ¹⁷¹ J. Im *et al.*, *ASME J. Electron. Packag.* **122**, 28 (2000).
- ¹⁷² J. C. Maisonnoble, G. Passemard, C. Lacour, Lecornec, P. Motte, P. Noel, and J. Torres, *Microelectron. Eng.* **50**, 25 (2000).
- ¹⁷³ E. O. Shaffer II, F. J. McGarry, and L. Hoang, *Polym. Eng. Sci.* **36**, 2381 (1996).
- ¹⁷⁴ A. Satta *et al.*, *Microelectron. Eng.* **60**, 59 (2002).
- ¹⁷⁵ S. Ito, Y. Homma, E. Saski, S. Urichama, and H. Morishima, *J. Electrochem. Soc.* **137**, 1212 (1990).
- ¹⁷⁶ M. P. Petkov, M. H. Weber, and K. G. Lynn, *J. Appl. Phys.* **86**, 3104 (1999).
- ¹⁷⁷ E. Kondoh, T. Asano, H. Arao, A. Nakashima, and M. Komatsu, *Jpn. J. Appl. Phys., Part 1* **39**, 3919 (2000).
- ¹⁷⁸ E. Kondoh, T. Asano, A. Nakashima, and M. Komatsu, *J. Vac. Sci. Technol. B* **18**, 1276 (2000).

- ¹⁷⁹E. Kondoh, M. R. Baklanov, H. Bender, and K. Maex, *Electrochem. Solid-State Lett.* **1**, 224 (1998).
- ¹⁸⁰P. J. Matsuo, T. E. F. M. Standaert, S. D. Allen, G. S. Oehrlein, and T. J. Dalton, *J. Vac. Sci. Technol. B* **17**, 1435 (1999).
- ¹⁸¹T. C. Chang, P. T. Liu, Y. S. Mor, S. M. Sze, Y.-L. Yang, M. S. Feng, F. M. Pan, B. T. Dai, and C. Y. Chang, *J. Electrochem. Soc.* **146**, 3802 (1999).
- ¹⁸²T. E. F. M. Standaert, P. J. Matsuo, S. D. Allen, G. S. Oehrlein, and T. J. Dalton, *J. Vac. Sci. Technol. A* **17**, 741 (1999).
- ¹⁸³T. E. F. M. Standaert, E. A. Joseph, G. S. Oehrlein, A. Jain, W. N. Gill, P. C. Wainer, Jr., and J. L. Plawsky, *J. Vac. Sci. Technol. A* **18**, 2742 (2000).
- ¹⁸⁴S. J. Wang, H. H. Park, and G. Y. Yeom, *Jpn. J. Appl. Phys., Part 1* **39**, 7007 (2000).
- ¹⁸⁵P. T. Liu, T. C. Chang, Y.-L. Yang, Y. F. Cheng, F.-Y. Cheng, F.-Y. Shih, J.-K. Lee, E. Tsai, and S. M. Sze, *Jpn. J. Appl. Phys., Part 1* **38**, 6247 (1999).
- ¹⁸⁶T. C. Chang, P. T. Liu, Y. J. Mei, Y. S. Mor, T. H. Perng, Y.-L. Yang, and S. M. Sze, *J. Vac. Sci. Technol. B* **17**, 2325 (1999).
- ¹⁸⁷T. C. Chang, P. T. Liu, F.-Y. Shih, and S. M. Sze, *Electrochem. Solid-State Lett.* **2**, 390 (1999).
- ¹⁸⁸P. T. Liu, T. C. Chang, Y. S. Mor, and S. M. Sze, *Jpn. J. Appl. Phys., Part 1* **38**, 3482 (1999).
- ¹⁸⁹P. T. Liu, T. C. Chang, Y.-L. Yang, Y. F. Cheng, J.-K. Lee, F.-Y. Shih, E. Tsai, G. Chen, and S. M. Sze, *J. Electrochem. Soc.* **147**, 1186 (2000).
- ¹⁹⁰H.-C. Liou, J. Duell, V. Finch, Q. Han, P. Sakthivel, and R. Ruffin, *Mater. Res. Soc. Symp. Proc.* **612**, D5.11.1 (2000).
- ¹⁹¹T. Furusawa, D. Ryuzaki, R. Yoneyama, Y. Homma, and K. Hinode, *Electrochem. Solid-State Lett.* **4**, G31 (2001).
- ¹⁹²D. Shamiryan, M. R. Baklanov, S. Vanhaelemeersch, and K. Maex, *J. Vac. Sci. Technol. A* **20** (in press).
- ¹⁹³M. R. Baklanov, M. Van Hove, G. Mannaert, S. Vanhaelemeersch, H. Bender, T. Conard, and K. Maex, *J. Vac. Sci. Technol. B* **18**, 1281 (2000).
- ¹⁹⁴T. E. F. M. Standaert et al., *J. Vac. Sci. Technol. A* **19**, 435 (2000).
- ¹⁹⁵S. A. Vitale, H. Chae, and H. H. Sawin, *J. Vac. Sci. Technol. A* **18**, 2770 (2000).
- ¹⁹⁶D. Fuard, O. Joubert, L. Vallier, and M. Bonvalot, *J. Vac. Sci. Technol. B* **19**, 447 (2001).
- ¹⁹⁷O. Joubert, J. Pelletier, C. Friori, and T. A. Nguyen Tan, *J. Appl. Phys.* **67**, 4291 (1990).
- ¹⁹⁸O. Joubert, C. Friori, J. C. Oberlin, P. Paniez, J. Pelletier, M. Pons, T. Vachette, and A. Weill, *J. Appl. Phys.* **69**, 1697 (1991).
- ¹⁹⁹M. R. Baklanov, S. Vanhaelemeersch, H. Bender, and K. Maex, *J. Vac. Sci. Technol. B* **17**, 372 (1999).
- ²⁰⁰T.-C. Wei, C.-H. Liu, J.-M. Shieh, S.-C. Suen, and B.-T. Dai, *Jpn. J. Appl. Phys., Part 1* **39**, 7015 (2000).
- ²⁰¹T. E. F. M. Standaert, P. J. Matsuo, S. D. Allen, G. S. Oehrlein, T. J. Dalton, T.-M. Lu, and R. Gutmann, *Mater. Res. Soc. Symp. Proc.* **511**, 265 (1998).
- ²⁰²S. H. Kim, H. S. Moon, S. G. Woo, and J. Ahn, *Jpn. J. Appl. Phys., Part 1* **38**, 7122 (1999).
- ²⁰³J. M. Cook, O. Turmel, T. Wicker, and J. Winniczek, *Technical Proceedings, SEMICON Japan* (SEMI, Chiba, 1993).
- ²⁰⁴Y. Y. Maruo, S. Sasaki, T. Haga, H. Kinoshita, T. Horiuchi, and T. Tamamura, *J. Vac. Sci. Technol. A* **14**, 2470 (1996).
- ²⁰⁵Y. Morikawa, S. Yasunami, W. Chen, T. Hayahsi, and T. Uchida, *J. Vac. Sci. Technol. A* **19**, 1747 (2001).
- ²⁰⁶C. E. Rogers, in *Polymer Permeability*, edited by J. Comyn (Elsevier, Amsterdam, 1985), Chap. 2, pp. 11–73.
- ²⁰⁷J. C. Arnell and H. L. McDermott, *Proceeding of the Second International Congress on Surface Activity* (Butterworths, London, 1957), p. 113.
- ²⁰⁸For pure Ta deposition also the substrate composition has a significant effect; the same concepts concerning porosity can be though applied also in this case (IMEC unpublished data).
- ²⁰⁹F. M. Smits, *Bell Syst. Tech. J.* **37**, 371 (1958).
- ²¹⁰M. Ritala and M. Leskelä, *Handbook of Thin Film Materials*, edited by H. S. Nalwa (Academic, New York, 2002), Vol. 1, pp. 103–159.
- ²¹¹W. Besling, A. Satta, J. Schuhmacher, T. Abell, V. Sutcliffe, A. M. Hoyas, G. Beyer, D. Gravesteijn, and K. Maex, *Proceedings of IITC*, 2002, pp. 288–291.
- ²¹²F. Iacopi, M. R. Baklanov, E. Sleafckx, T. Conard, H. Bender, H. Meynen, and K. Maex, *J. Vac. Sci. Technol.* **20**, 109 (2002).
- ²¹³F. Iacopi, Zs. Tökei, M. Stucchi, F. Lanckmans, and K. Maex, *IEEE Electron Device Lett.* (March, 2003).
- ²¹⁴D. Shamiryan, M. R. Baklanov, Zs. Tökei, F. Iacopi, and K. Maex, *Proceedings of the Advanced Metallization Conference* (Materials Research Society, Pittsburgh, PA, 2002), pp. 279–285.
- ²¹⁵D. Shamiryan, M. R. Baklanov, and K. Maex, *J. Vac. Sci. Technol. B* **21**, 220 (2003).
- ²¹⁶F. Iacopi, Zs. Tökei, D. Shamiryan, T. Q. Le, S. Malhouitre, M. Van Hove, and K. Maex, *Proceedings of the Advanced Metallization Conference* (Materials Research Society, Pittsburgh, PA, 2002), pp. 61–66.
- ²¹⁷*Monte Carlo Methods in Statistical Physics*, edited by K. Binder (Springer, Berlin, 1979).
- ²¹⁸M. Itoh, *Prog. Surf. Sci.* **66**, 53 (2001).
- ²¹⁹C. Orme and B. G. Orr, *Surf. Rev. Lett.* **4**, 71 (1997).
- ²²⁰S. Kersulis and V. Mitin, *Semicond. Sci. Technol.* **10**, 653 (1995).
- ²²¹I. K. Marmorkos and S. Das Sarma, *Phys. Rev. B* **45**, 11 226 (1992).
- ²²²J. D. Torre, M. D. Rouhani, R. Malek, D. Esteve, and G. Landa, *J. Appl. Phys.* **84**, 5487 (1998).
- ²²³V. M. Burlakov, G. A. D. Briggs, A. P. Sutton, and Y. Tsukahara, *Phys. Rev. Lett.* **86**, 3052 (2001).
- ²²⁴S. K. Dew, T. Smy, and M. J. Brett, *IEEE Trans. Electron Devices* **39**, 1599 (1992).
- ²²⁵A. V. Zverev, I. G. Neizvestny, N. L. Shvarts, and Z. Sh. Yanovitskaya, *Semiconductors* **35**, 1022 (2001); A. V. Zverev, I. G. Neizvestny, N. L. Shvarts, and Z. Sh. Yanovitskaya, *Microelectronics* **28**, 377 (1999).
- ²²⁶A. V. Chemakin, I. G. Neizvestny, N. L. Shvarts, Z. Sh. Yanovitskaya, and A. V. Zverev, *Phys. Low-Dimens. Semicond. Struct.* (to be published).
- ²²⁷I. G. Neizvestny, N. L. Shvarts, Z. Sh. Yanovitskaya, and A. V. Zverev, *Comp. Phys. Commun.* (to be published).
- ²²⁸A. Pimpinelly and I. Villain, *Physica A* **204**, 521 (1994).
- ²²⁹Y. Homma, H. Hibino, and T. Ogino, *Phys. Rev. B* **58**, 13 146 (1998).
- ²³⁰B. Voigtlander, A. Zinner, T. Weber, and H. P. Bonzel, *Phys. Rev. B* **51**, 7583 (1995).
- ²³¹N. Sato, K. Sakaguchi, K. Yamagata, Y. Fujiyama, and T. Yonehara, *J. Electrochem. Soc.* **142**, 3116 (1995).
- ²³²S. I. Romanov, V. I. Mashanov, L. V. Sokolov, A. Gutakovski, and O. P. Pchelyakov, *Appl. Phys. Lett.* **75**, 4118 (1999).
- ²³³C. Heyn, T. Franke, R. Anton, and M. Harsdorff, *Phys. Rev. B* **56**, 13 483 (1997).
- ²³⁴F. Iacopi, Zs. Tökei, Q. T. Le, D. Shamiryan, T. Conard, B. Brijs, U. Kreissig, M. Van Hove, and K. Maex, *J. Appl. Phys.* **92**, 1548 (2002).
- ²³⁵H. J. Lee et al., *J. Electrochem. Soc.* **148**, F195 (2001).
- ²³⁶E. T. Ryan, J. Martin, K. Junker, J. J. Lee, T. Guenther, J. Wetzel, S. Lin, D. W. Gidley, and J. Sun, *Proceeding Of IITC*, 2002, pp. 27–29.
- ²³⁷G. R. Yang, Y. P. Zhao, B. Wang, E. Barnat, J. McDonald, and T. M. Lu, *Appl. Phys. Lett.* **72**, 1846 (1998); J. W. Nah, W. S. Choi, S. K. Hwang, and C. M. Lee, *Surf. Coat. Technol.* **123**, 1 (2000); T. Hara, K. Sakamoto, F. Togoh, Hongning-Yang, and D. R. Evans, *Jpn. J. Appl. Phys., Part 2* **39**, L506 (2000).
- ²³⁸K. W. Gerstenberg and M. Grischke, *J. Appl. Phys.* **69**, 736 (1991).
- ²³⁹A trademark of Dow Corning. For more information about the material see www.dowcorning.com
- ²⁴⁰M. K. Blank, J. Huang, and D. Cheung, *Thin Solid Films* **308**, 507 (1997).
- ²⁴¹A trademark of Honeywell. For more information about the material see www.electronicmaterials.com
- ²⁴²M. E. Mills, P. Townsend, D. Castillo, S. Martin, and A. Achen, *Microelectron. Eng.* **33**, 327 (1997).
- ²⁴³A trademark of Dow Chemical. For more information about the material see www.dow.com
- ²⁴⁴A trademark of ASM. For more information about the material see www.asm.com
- ²⁴⁵A trademark of Novellus Systems. For more information about the material see www.novellus.com
- ²⁴⁶A trademark of Applied Materials. For more information about the material see www.appliedmaterials.com
- ²⁴⁷J. G. Wang, H. K. Kim, F. G. Shi, B. Zhao, and T. G. Nieh, *Thin Solid Films* **377**, 413 (2000).

²⁴⁸ A trademark of CCIC.

²⁴⁹ A trademark of JSR microelectronics. For more information about the material see www.jsrusa.com

²⁵⁰ A trademark of Shipley. For more information about the material see www.shipley.com

²⁵¹ A trademark of Trikon. For more information about the material see www.trikon.com

²⁵² X. Xiao, R. Streiter, H. Wolf, G. Ruan, G. Murray, and T. Gessner, *Microelectron. Eng.* **55**, 53 (2001).

²⁵³ C. Murray *et al.*, *Microelectron. Eng.* **60**, 133 (2002).